

Investigating Triboelectric Discharge at Gale Crater, Mars

Hemani Kalucha

A Thesis Submitted to
The Faculty of Graduate Students
In Partial Fulfilment of The Requirements
For the Degree of
Master of Science

Graduate Program in Earth and Space Science
York University
Toronto, Ontario

June 2020

©Hemani Kalucha, 2020

Abstract

Saltation-induced triboelectric discharge has been theorized to occur on Mars, however, it has never been observed in-situ. It is hypothesized to play a key role in trace gas variation at Gale Crater, specifically as a fast destruction mechanism for methane. To maximize the likelihood of observing the discharge's faint signal, a high-resolution record of saltation activity was produced using MastCam-100. MastCam-L0 and MAHLI were found to be the most suitable cameras with which to observe the discharge. Since the magnitude of discharge is well below the dark noise of these two cameras, it will not be possible to see the glow. However, performing such an observation will enable the definition of an upper limit of the magnitude of discharge, calculated in this work as the radiance limit of the respective cameras. Comparing the annual methane and saltation cycles shows methane levels decreasing in conjunction with increase in saltation activity.

Acknowledgements

First and foremost, the biggest thank you to my advisor, John, for taking a chance on a rookie engineer. All I ever wanted to do was work on a Mars mission and you made it possible at 22. Any footing I have in the world of planetary science is your doing.

Next I'd like to thank Christina, without whom no part of this thesis would be possible. Any email, any question, any coding problem was always met with the most detailed of replies. I was terrified of failing at research and your support gave me the ability to work through every task.

This year would be incomplete without my dear colleagues Alex, Jake, Paul, Charissa, Giang, Solomon, and Noah.

A special shout out to Dr. Mark Lemmon who knows everything about everything and is responsible for key parts of this thesis coming together. And to Dr. Claire Newman, Dr. Tim McConnochie, and Dr. Mariah Baker for generously donating their time to the frustrating difficulties of studying triboelectric discharge on Mars with me.

Thank you, in huge part, to my thesis committee: Prof. Mark Gordon, Prof. Isaac Smith, and Prof. Adam Muzzin for making it through my thesis without falling asleep and providing such valuable feedback!

Last but not least, a big thank you to the MSL team for allowing me to be a part of a real life space mission, I thought I'd have to wait a lot longer for this opportunity.

And, as always, to my parents, for everything else.

Table of Contents

Abstract	ii
Acknowledgements	iii
Table of Contents	iv
List of Tables	vii
List of Figures	viii
1 Introduction	1
1.1 The Physics of saltation-induced Triboelectric Discharge	1
1.2 Laboratory Simulations of Triboelectric Discharge in Martian conditions . .	5
1.3 Observing Triboelectric Discharge on Mars	7
1.3.1 Gale Crater	9
1.4 Environmental Conditions for Triboelectric Discharge	9
1.5 Nighttime Wind Stress at Gale Crater	12
1.6 Lowered saltation threshold on Mars	14
1.7 Effects of Triboelectric Discharge on Trace Gas processes	16
1.8 Methane	19
1.9 Methane Release/Replenishment	20
1.10 Atmospheric Measurements of Methane	20
1.11 Oxygen and Methane Destruction Mechanism	22
1.12 Replenishment of Oxygen	25
1.13 Overview	25
2 Analyzing saltation events with MSL data	26
2.1 LOS Dataset	26
2.2 Processing of MastCam-100 LOS Images	29

2.3	Associated Errors	32
2.4	Analysis of mean extinction variation	32
2.5	Analysis of vertical extinction variation	34
3	Ability of mission cameras to detect Triboelectric Discharge	40
3.1	Predicted Signal Strength of the Discharge Glow	40
3.2	Theoretical Radiance Limits	43
3.2.1	Comparison with Phobos Shine	46
3.3	Archival Datasets	48
3.4	Theoretical detection limits and camera suitability	49
3.4.1	MSL	49
3.4.2	Other Spacecraft	52
3.5	Glow detection limits from archival data	52
3.5.1	MastCam Results	53
3.5.2	MAHLI results	59
3.6	Upper Limit of Glow	61
4	Evaluating trace gas emission cycles at Gale	63
4.1	Periodicity	63
4.2	Statistical Analysis of Annual Methane Variation	65
4.3	Assessment of Periodicity with Lomb-Scargle Periodogram	68
4.4	Atmospheric Cycles	73
4.5	Methane Destruction Rate Calculations	76
5	Conclusion	82
	Bibliography	87
	Appendices	103
A	MAHLI Image Calibration	103

List of Tables

1	Summary of laboratory simulations of triboelectric discharge in martian conditions	6
2	Summary of Camera Parameters for MSL	44
3	Summary of Camera Parameters for InSight and Mars2020	45
4	Summary of Camera signal strength of triboelectric discharge, FOV, and pointing capabilities	49
5	Summary of Radiance Limits of each Camera on MSL	51
6	Comparison of signal strength of triboelectric discharge in MastCam on MSL and MastCam-Z on Mars 2020	52
7	Median Pixel Radiances of MastCam Nighttime Images	54
8	Median radiance value of MAHLI nighttime images.	62
9	Error Margin in Atmospheric Cycles	74
A.1	Ratio of MastCam-34 radiance to MAHLI RAD value ($\text{W}/\text{m}^2/\text{nm}/\text{Sr}$)	105

List of Figures

1	Schematic of Saltation	2
2	Saltation trajectories of charged particles	4
3	Lab simulation of triboelectric discharge in Martian conditions	8
4	Ripple and dune migration at Gale Crater	10
5	Wind stresses in 3 hour intervals as a function of L_s at Gale Crater, Mars.	14
6	Seasonal trends in the instantaneous volume mixing ratios of the three most abundant noncondensable gases in the Mars atmosphere	18
7	Example of LOS observation taken in each camera	28
8	Mean Extinction Data	33
9	Variation in Red Filter Vertical Extinction at Gale	35
10	Variation in Green Filter Vertical Extinction at Gale	36
11	Variation in Blue Filter Vertical Extinction at Gale	37
12	Spectral sensitivities of MSL's cameras overlaid on to Ar spectra	41
13	Colourmap of MastCam image taken on sol 529	58
14	Histogram of pixel values of three MastCam L0 images	58
15	Histogram of pixel radiance values of three MAHLI images	60
16	SAM-TLS measurements at Gale Crater	64
17	Statistical possibilities of Methane variation	66
18	Probability Density Function of Statistical Possibilities	67
19	Comparison of Lomb Scargle to GP Bayesian Model	69
20	Comparison of Lomb Scargle Periodograms of W18 and W20 data	70
21	Identifying False Peaks in Lomb-Scargle Periodogram	72
22	LSP of Atmospheric Argon, Nitrogen, and dust at Gale	73
23	LSP of Atmospheric Oxygen at Gale	75
24	Methane destruction cycle at Gale	75
25	Area covered by simulated methane release	78

A1	Ratio of MastCam-34 radiance to MAHLI RAD for red, green, and blue channels, in time order.	106
B1	Variation in Red Filter Vertical Extinction at Gale with sol and L_s of complete MastCam-100 LOS dataset	107
B2	Variation in Green Filter Vertical Extinction at Gale with sol and L_s of complete MastCam-100 LOS dataset	108
B3	Variation in Blue Filter Vertical Extinction at Gale with sol and L_s of complete MastCam-100 LOS dataset	109

1 Introduction

Triboelectric charging occurs when sand grains rub against each other. The resulting electrostatic attraction is strong enough to propel electrons across the separation between the grains, ionizing gas molecules in their path (Olawale et al., 2016). The gas undergoes excitation and returns to ground state, releasing an emission glow, the spectrum of which is highly dependent on the material composition of the sand grains and the atomic structure of the gas. Laboratory studies have suggested that saltation, the process of wind forcing dust particles to move in jumps, is powerful enough to produce triboelectric discharge in the Martian atmosphere (Krauss et al., 2003, 2006). Mars' low pressure and gravity creates an electric breakdown limit of 20 kV/m as opposed to 3000 kV/m on Earth, aiding triboelectric discharge (Melnik and Parrot, 1998; Zhai et al., 2006).

1.1 The Physics of saltation-induced Triboelectric Discharge

Wind is able to lift sand grains from the surface when it exceeds a frictional velocity (u^*), where $u^* = \sqrt{\tau/\rho_a}$, τ is the wind shear stress, and ρ_a is the air density. Saltation is continued by lifted particles impacting the ground, and ejecting other particles (Kok, 2010). The sand grains have intersecting trajectories; they impact the ground at angles of 5-15° and lift off from the ground at an average of 40° (Rice et al., 1995), and come into contact as a result. The sand grains on Mars are made up of a high percentage of silica (SiO_2), which is a strong insulator (Rieder et al., 1997).

Particles incur charging through contact when there is a difference in contact potential, which doesn't exist between two particles of the same material (like sand/dust on Mars). A contact potential is the difference between work functions of two different materials; a work function is the amount of energy required for a material to give up an electron. There are two alternative theories about how two insulators of the same material get charged. The first theory proposes that particles are charged by the transfer of electrons in high energy states in one particle to the empty spaces in low-energy levels in another particle (Lowell

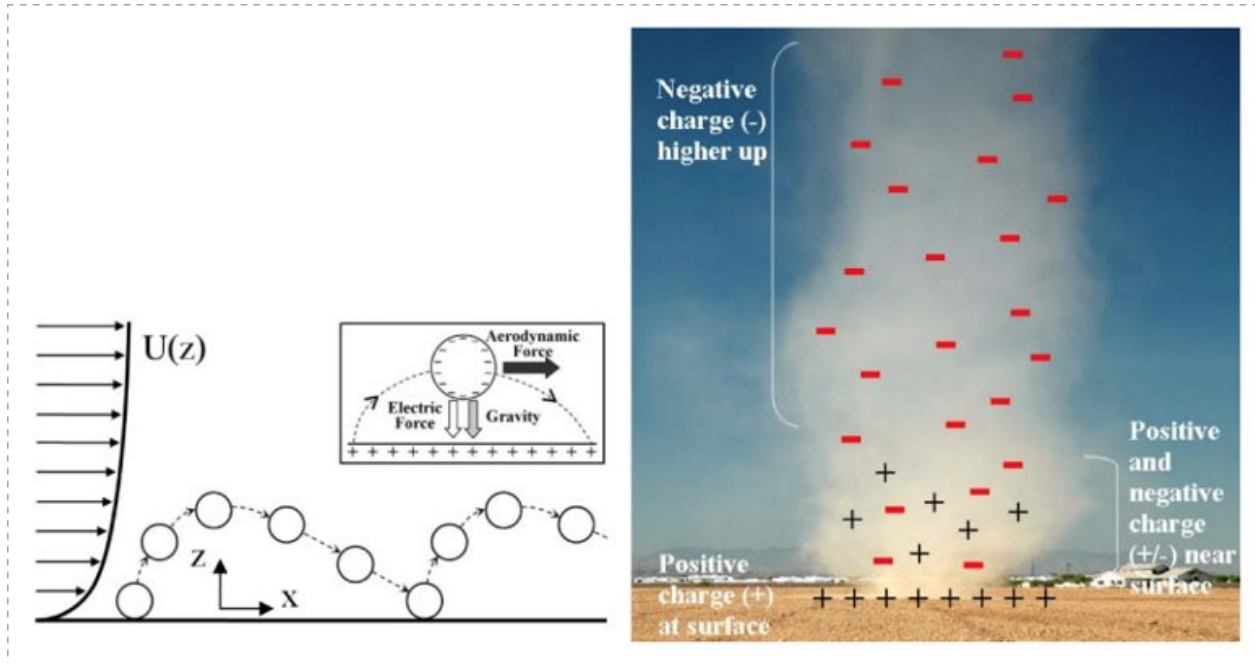


Figure 1: Taken from Figure 1, Kok (2008). (Left) Schematic of saltation, showing the logarithmic wind profile $U(z)$, and sand particles propelled by saltation. The inset shows the force diagram of a negatively charged saltating particle over the positively charged soil surface (Right) Hypothesized charge distribution in dusty phenomena. Larger particles become positively charged and sink to the surface. Smaller particles become negatively charged and stay suspended. The net charge by saltating particles can be either positive or negative. The charge separation can produce large electric fields.

and Truscott, 1986), which is consistent with electron transitions favouring the occupation of lower energy states whenever possible. Larger particles expose more surface area, and therefore lose more electrons in this way, making them positively charged; this process is known as ‘asymmetric rubbing’. The second theory proposes that even if both small and large particles lose equal numbers of electrons, over the course of multiple electron loss interactions, the smaller particles lose the ability to give up any more electrons, and stay negative (Lacks, 2008). In both scenarios, larger sand grains tend to accumulate positive charge and fall to the surface due to gravity while smaller sand grains tend to accumulate negative charge and stay suspended. Contact can occur between saltating particles and the ground and saltating particles and dust, as shown in figure 1. The ground is made up of larger particles and is thus positively charged, while dust is made up of smaller particles and is thus negatively charged (Kok, 2008). The net charge on a saltating particle in between the ground and the dust is decided by its current charge, radius, and contact potential in the collision. However, realistic charging parameters would also include temperature, humidity, particle speed, etc. (Renno and Kok, 2008). This formation creates an upward pointing electric field: this effect has been modelled and proved experimentally (Schmidt et al., 1998; Forward et al., 2009). No electric field measurements have been made on Mars to date.

The electric field set up in the atmosphere produces small discharges, as a few free electrons have the energy to conduct across the electric field (Treumann et al., 2008). When the electric field strength exceeds 20 kV/m from the build up of particle charging and separation, the martian atmosphere is no longer capable of insulating the charges, and undergoes electric breakdown. A large number of electrons gain enough energy to conduct across the electric field and release electrons from other gas molecules in their path, which produces more electrons at an exponential rate (known as avalanching) (Ray, 2013). The rush of current creates a series of discharges. Arc discharges require high density electric fields while Townsend discharges occur in a weak and low-density current flow, the latter of which is likely to occur on Mars due to its low pressure environment. Townsend discharges are known to produce glow in infrared, visible, and ultraviolet ranges as opposed to Arc discharges, where deep

ultraviolet/x-rays are released. Electron avalanches are composed of run-away electrons (the higher energy electrons before breakdown), free electrons that have gained sufficient energy to ionize after breakdown, and secondary electrons, which are freed electrons from gaseous molecules. The avalanche takes the form of a tail, with the electron cloud at the front and the positive ions lagging behind (Treumann et al., 2008).

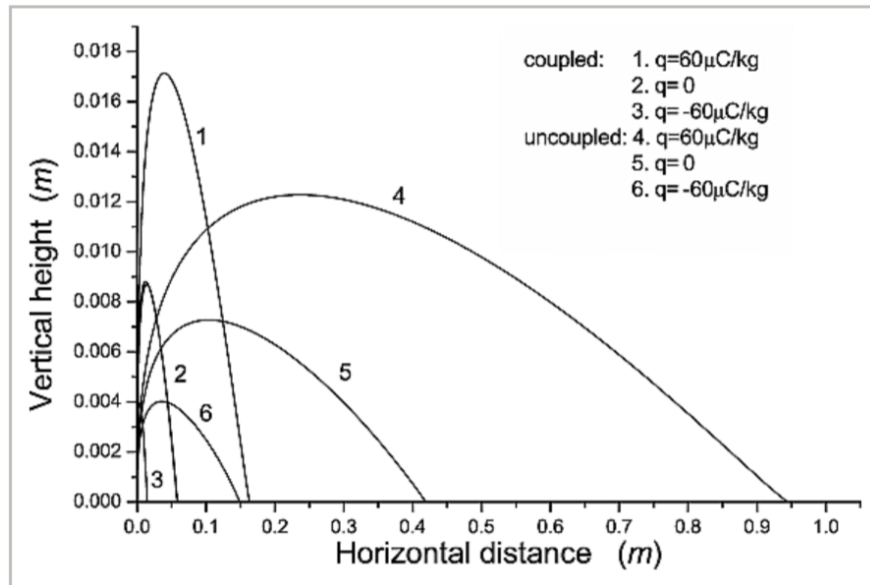


Figure 2: Taken from Figure 4, Zheng et al. (2003). Comparison of trajectories of sand particle motion in saltation cloud when the effect of drag force on wind flow is or is not considered, which are respectively marked by “coupled” and “uncoupled” and when the sand grain possesses different electric charges. (frictional velocity applied is 0.4 m /s)

Uniformly sized sands produce weak electric fields, since the charges are not forced to separate by weight. In mixed particle-size sands (naturally occurring on Mars), the charge to mass ratio increases with height from the sand bed, and decreases with increasing wind speed as a higher number of larger, positively charged sand particles are lifted off the ground. The electric field observed is non-uniform; it increases with increasing height, as suspended particles exert additional electrostatic forces on particles outside of the electric field, and thus expand the electric field (Zheng et al., 2003). The electrostatic attraction between the

sand grains is significant enough to alter the trajectories of the particles (Schmidt et al., 1998); positively charged particles are able to attain higher vertical heights followed by neutrally charged particles and negatively charged particles, as demonstrated in Figure 2, due to the direction of the electric field. The drag force, exerted by the particles opposite to the direction of wind flow, significantly limits the horizontal distance achieved by particles in a single jump, as expected. Electrostatic forces explain why saltating particles do not achieve greater heights with increasing wind speed (Namikas, 2003). For reference, the work function of Mars JSC-1, a martian soil simulant, was found to be 5.6 eV, indicating that it is a stronger insulator compared to stainless steel but weaker than Teflon (Sternovsky et al., 2002; Sharma et al., 2008).

1.2 Laboratory Simulations of Triboelectric Discharge in Martian conditions

Krauss et al. (2003) were one of the first to experimentally investigate whether martian sand-grain interaction could produce charge; they simulated the grains mixing in two ways. Horizontal mixing of JSC-1 Mars regolith simulant was created using a vacuum jar filled with CO_2 gas at 1-8 Torr, and a stirring rod, the speed of which was converted to an equivalent wind speed. The results showed that charges were produced at wind speeds of 2 m/s and higher. The second experiment simulated vertical mixing of a combination of 100 μm JSC-1 simulant and 53 μm glass particles with a rotating glass tube 1.2 m long, similarly filled with CO_2 gas at 1-8 Torr. Krauss et al. (2003) noted that a mixture of different particle sizes produced a bigger discharge than experiments with single-sized particles. The number of charges produced by a vertical drop was highest at 1 Torr and decreased with increasing pressure; however, charges were still produced at 6 Torr, the average pressure at the Martian Surface. The magnitude of the charge differed by as much as 0.1-50 V depending on the pressure used (Krauss et al., 2003). The results of similar laboratory simulations are summarized in Table 1.

The most recent laboratory simulation produced saltation induced triboelectric discharge

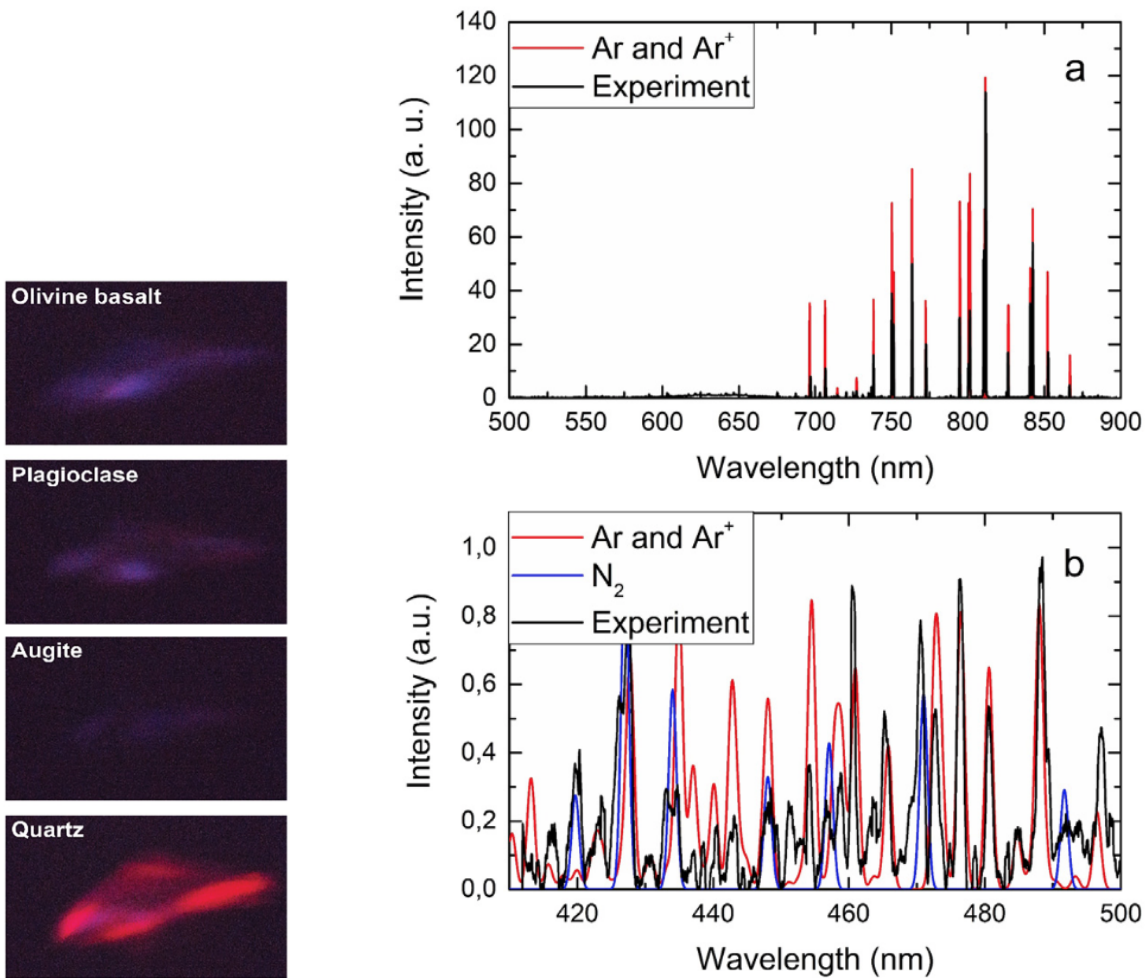
Table 1: Summary of laboratory simulations of triboelectric discharge in martian conditions

Author	Martian Soil Simulant	Particle Size	Atmospheric Conditions	Windspeed	Charging
Eden and Vonnegut (1973)	50 g dry sand	-	CO_2 , 10 mbar	manually agitated	spark like discharges visible
Fabian et al. (2001)	150 ml JSC-1	45-53 μm	CO_2 , 0.1-50 Torr	1.16-2.58 m/s	6 V at 6 Torr
Gross et al. (2001)	1 g JSC-1	as in JSC-1 (up to 1000 μm)	air, 7 Torr , 22 °C	vertical drop apparatus	0.167 nC/g on glass surface
Aplin et al. (2012), reproduction of Krauss et al. (2003) vertical drop experiment	JSC-1 + 53 μm glass particles	as in JSC-1	CO_2 , 7-9 mbar	vertical drop apparatus	500 g JSC-1: -11 V, 400 g dust + 130 g glass: -0.3 V
Bo et al. (2013)	glassy particles	1-10 mm	N_2	0-5.5 m/s	up to -225 $\mu\text{C}/\text{m}^3$
Thøgersen et al. (2019)	olivine basalt, plagioclase, augite, quartz	0.125-1 mm	Martian atmospheric composition, 8 mbar	21.5 m/s	10 $\mu\text{W}/\text{m}^2$

of magnitude $10 \mu\text{W}/\text{m}^2$ (Thøgersen et al., 2019) under Martian conditions. The experiment used 10 g of simulant regolith in a quartz tube, filled with gas of Martian-atmospheric composition at 8 mbar pressure. Saltation was simulated by shaking the quartz tube along its longest axis at a speed of 1 m/s, which corresponds to a windspeed of 21.5 m/s. The glow caused by triboelectric discharge was detected in images obtained of four different materials (Figure 3a). The spectra produced by the discharge of plagioclase, one of the four materials, was prominent in the infrared range (700-870 nm) but also featured in the visible range at a much lower intensity. The relative intensity of the infrared spectrum reached a maximum of 120 a.u. (arbitrary units) whereas the visible spectrum reached a maximum of 1 a.u. (Figure 3b).

1.3 Observing Triboelectric Discharge on Mars

Triboelectric discharge has never been observed on Mars. We can attempt to observe triboelectric discharge with mission cameras. Two landed spacecraft are currently active on Mars: the Mars Science Laboratory rover (Curiosity, MSL) and the InSight (Interior Exploration using Seismic Investigations, Geodesy and Heat Transport) lander. The Mars 2020 (Perseverance) rover, the successor to MSL, is due to land in 2021, providing a potential near-term addition to the active spacecraft complement on the surface of Mars. These spacecraft are, or will be, equipped with a variety of cameras both as part of science payloads and engineering systems, which could be used to place observationally-derived limits on, if not positively detect, the glow discharge from saltation on the surface of Mars for the first time. Since MSL has higher resolution cameras compared to InSight, a requirement for capturing a signal as faint as the glow, and is a currently active mission, this thesis will focus on investigating triboelectric discharge at Gale Crater, the landing site of MSL. Furthermore, Thøgersen et al. (2019) have claimed that the discharge should be detectable using MSL's MastCam.



(a) Images of Triboelectric Glow

(b) Spectra of Triboelectric Glow

Figure 3: Taken from Figure 1c and 2, (Thøgersen et al., 2019). (a) Photos of the saltation-induced glow from four minerals in a Mars-like atmosphere at a pressure of 8 mbar. (b) Selected emission spectra from ampoules containing plagioclase in a Mars-like atmosphere. The spectra are recorded with a spectral resolution of 0.6 nm and 1.2 nm, respectively. The background spectra recorded when the ampoule is at rest have been subtracted from the two emission spectra. The spectra are corrected for the instrument response and shown to scale. The measured spectra are compared to literature values for Ar and Ar^+ (red line) and N_2 (blue line) convoluted with the spectral resolution of the measurements.

1.3.1 Gale Crater

MSL is an active mission situated in the northwest corner of Gale Crater (4.59°S, 137.44°E) (Grotzinger et al., 2012). Gale crater was formed from an impact \sim 3.6 billion years ago and has a diameter of \sim 154 km. It is the site of an ancient lake, giving it great astrobiological potential (Wray, 2012).

1.4 Environmental Conditions for Triboelectric Discharge

Triboelectric discharge is produced when saltation occurs, but it has never been observed in-situ and has a small predicted flux, making it difficult to observe with mission cameras. To understand when triboelectric discharge is most likely to occur and thus easiest to observe, it is necessary to study patterns of saltation. Saltation is a wind-blown sand process and is known to produce aeolian bed forms such as dunes and ripples. Since these features are found ubiquitously on Mars today, saltation must have occurred at some point in the history of Mars. However, the dunes on Mars show relatively little cratering, suggesting they are less than 100,000 years old and a product of recent saltation (Bourke et al., 2008). For triboelectric discharge to occur today, there must be active saltation on present day Mars. The existence of active saltation can be deduced based on dune and ripple migration seen in orbital data. To summarize simplistically, a dune is a large pile of sand that displays directional information about winds. One side of the dune is an evenly inclined surface; wind pushes sand particles up this surface by saltation. The grains collect past the highest point of the dune, which eventually avalanches under its own weight, creating a much steeper decline to reach the ground (Fenton, 2005). This side is known as the slipface. Smaller piles of sand, known as ripples, function in the same way on a smaller scale. As wind continues to blow on the scale of days and years, ripples and dunes migrate in the direction of the wind. Thus, recent orbital and rover data showing dune and ripple migration is proof of active saltation occurring on present day Mars, as in Figure 4 (Ayoub et al., 2014; Baker et al., 2018).

Evidence of saltation on Mars has been detected by several orbital and landed spacecraft.

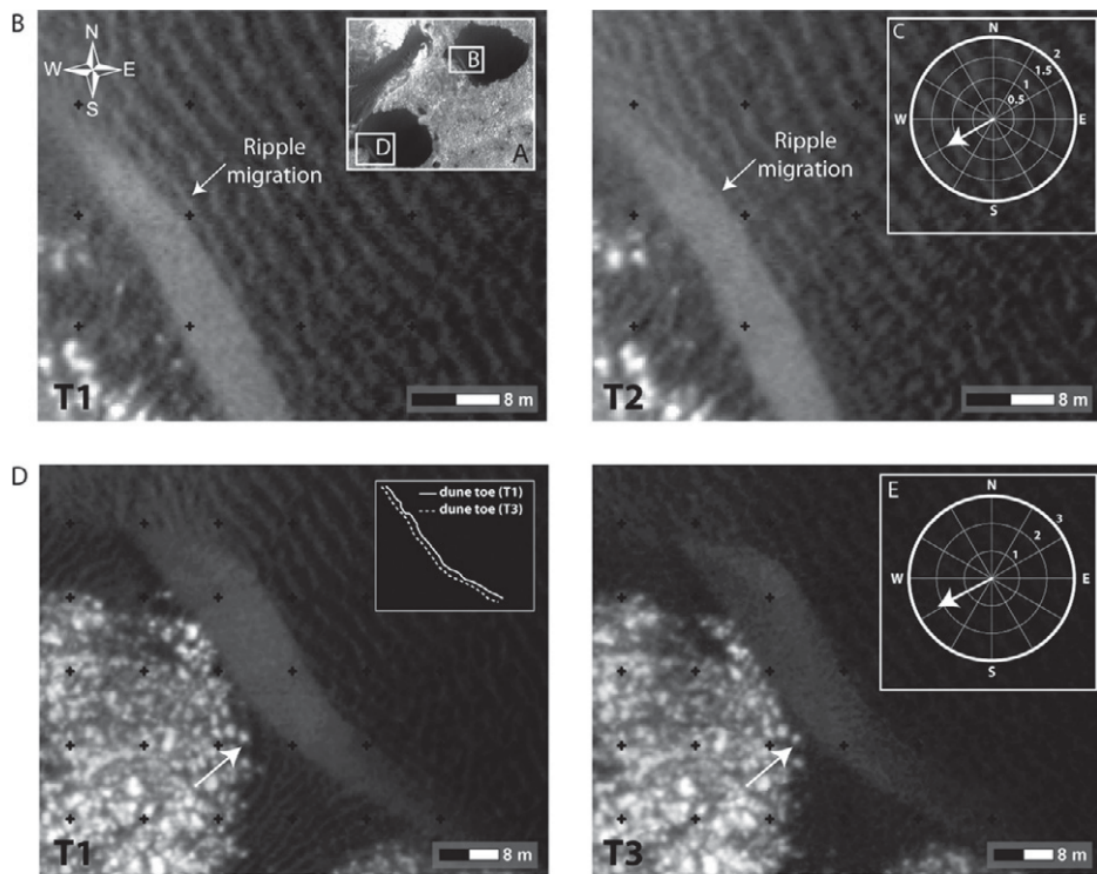


Figure 4: Taken from Figure 3, Silvestro et al. (2013). Ripple and dune migration in the southwest sector of the dune field. A: Locations of the images in B and D. Location of A is shown in Figure 1B. B: Ripple migration over the stoss side of a dune between Mars year (MY) 28 and 29 (A.D. 2006–2008). White arrow indicates the same ripple in the two subimages. Note how the ripple position changes compared to the reference grid. C: Magnitude and direction of the ripple migration (in meters). D: Dune migration between MY 28 and 31 (2006–2011). E: Magnitude and direction of the dune migration (in meters). Note how the dunes advance with respect to the reference grid and to the white arrow that indicates the same feature in the two subimages.

Saltation was observed at Gusev Crater from surface images collected by the Spirit Rover (Greeley et al., 2006). The source of the movement was suggested to be primarily afternoon north-northwest moving winds with a secondary nighttime/early morning wind. Furthermore, the Mars Global Surveyor and the Mars Reconnaissance Orbiter observed erasure of the Spirit rover track from sediment transported by surface winds (Geissler et al., 2010). Though sedimentation is involved in track erasure to some degree, significant changes to the track occurred on the timescale of days, which cannot be accomplished by sedimentation, and is further evidence of saltation. Saltation has also been confirmed at the Bagnold Dune Field in Gale Crater, with migration rates up to 2.8 cm/sol (Baker et al., 2018). On Mars, saltating particles can be lifted to a height of ~ 18 cm according to wind tunnel tests (Bridges et al., 2005). Thus, it should be noted that triboelectric discharge is a strongly near surface process. Given the widespread existence of saltation features seen on Mars, saltation must be possible much more frequently and independently of dust devils.

The Mars General Circulation Model (MGCM) simulates sand transport by predicting wind stresses and wind directions based on the given pressure, density, and gravity conditions on Mars. However, it is unable to reconcile with orbital data in certain ways. Using the MGCM, a wind stress of 0.024 N/m^2 was found to best match the distribution of dune deposits on present day Mars (Anderson et al., 1999). This is $\sim 40\%$ lower than the lowest possible physical saltation threshold on Mars (0.04 N/m^2) (Iversen et al., 1976). Inside Procter Crater, active saltation is noticeable from erased dust devil tracks and multiple dune slipface orientations. However, the Mars-MM5 (Mars Mesoscale Model) circulation model predicts wind stresses inside the crater to be less than half of what is required to reproduce dunes of the size found in Procter Crater (Fenton, 2005). At Gale Crater specifically, the MRAMS (Mars Regional Atmospheric Modelling System) modelled wind stress ratio was found to be 0.57 or approximately half of what is required to initiate saltation (Silvestro et al., 2013).

However, three different dune slipface orientations are observed at Procter Crater whereas the MM5 model can only account for two. The third slipface cannot be explained by a wind

pattern included in MM5. All three wind circulation models acknowledge that the models do not account for short-term, small-scale winds, which may surpass saltation thresholds. A more fine-scale model is needed as these models operate at a resolution 2-5 times the size of the landform (1-100 m) (Jackson et al., 2015). A new microscale model created by Jackson et al. (2015) with a resolution of 5 m revealed two additional factors affecting slipface orientation and ripple migration in Procter Crater. The taller dunes in the crater are able to divert and, in some cases, reverse the wind direction of primary winds to create additional wind flow. Secondly, sharply peaked dunes are able to accelerate wind flow by 150-200%, the same amount by which wind stress predictions are lacking in circulation models. Such a hypothesis is further supported by the the observed volume loss in three polar dunes by the Mars Orbiter Camera (MOC) from 1997-2006. One of the dunes in particular, measuring 19 by 24 m lost 80% of its volume (Bourke et al., 2008). Therefore, active saltation does occur on Mars even if it cannot be predicted by meso-scale circulation models.

Furthermore, saltation activity shows strong seasonal variations, and is most active during the northern winter. Ayoub et al. (2014) measured the ripple migration at Nili Patera dune field in sequential HiRISE images during MY30, and found the migration to be three times higher in northern winter than in northern summer. The sustained flux observed throughout the year, suggests that sand-moving winds occur daily. The effective initiation threshold, simulated in Mars WRF (Weather Research and Forecast System) by adjusting wind stresses such that they match the migration rates above, is estimated to be 0.01 N/m^2 (Ayoub et al., 2014). The Bagnold dune field in Gale Crater is generally inactive from L_s 0-180° as well, suggesting that Gale Crater encounters similar saltation activity to other regions of Mars (Baker et al., 2018).

1.5 Nighttime Wind Stress at Gale Crater

To observe glow discharge, the near surface needs to achieve a threshold wind stress that triggers saltation. In addition, it is only possible to observe glow discharge with a mission camera at night since is too faint to be seen in sunlight (Thøgersen et al., 2019). The aeolian

bedform migration noted above does not reveal the times of day at which saltation occurs. Saltation varies as a function of wind stress, which describes the dust lifting capability of the wind. It is calculated at Gale using meteorological data collected by REMS (Rover Environmental Monitoring Station) on MSL and wind circulation models. It is critical to understand nighttime wind stress variation at Gale to assess whether triboelectric discharge can occur at night. Due to a lack of rover activity past sunset, the variation of wind stress at Gale Crater at night is poorly constrained, relying on sparse late-night REMS data and wind stresses predicted from atmospheric models. The Bagnold Dunes campaign used a particularly dense set of REMS observations over several days to verify the accuracy of Mars WRF in the crater. The Mars WRF model was found to consistently under-predict the windspeed in comparison to daytime REMS observations, each time by a factor of 3 or 4. The highest wind speed values from the model and the in-situ data occur in the afternoon at 13:00 LTST. Both the REMS data and the model show a decrease in windspeed after 15:00 LTST. Though the REMS dataset becomes sparse at 18:00 LTST, the model predicts a resurgence of windspeed at 18:00 LTST to afternoon levels, suggesting that nightly windspeeds are actually as strong as midday values (Newman et al., 2017).

However, a full analysis of the REMS data does not support this result. The average nighttime winds are decidedly lower than the average daytime values in every L_s category (Viúdez-Moreiras et al., 2019a). Nevertheless, amongst the nighttime periods 18:00-21:00, 21:00-24:00, 0:00-3:00 LTST, the strongest winds occur during L_s 240-300°, at 18:00-21:00 LTST or during L_s 180-240°, 21:00-24:00 LTST. The lower averages of nighttime winds do not imply that they can never reach daytime speeds. From the Weibull distributions of these time categories, it is possible to see that daytime and nighttime winds follow similar maximum-minimum limits (0-18 m/s and 0-15 m/s respectively), but with some differences in their probability distribution (Viúdez-Moreiras et al., 2019b). Mainly, the nighttime distributions are more skewed to lower values than the daytime distributions.

Figure 5 shows the wind stress variations in three hour groupings for an entire Mars year. To capture glow discharge at night time, it follows that the best season would be after

L_s 180°, from 18:00-21:00 LTST, when the highest night wind stresses are simulated. This agrees with the windspeed findings.

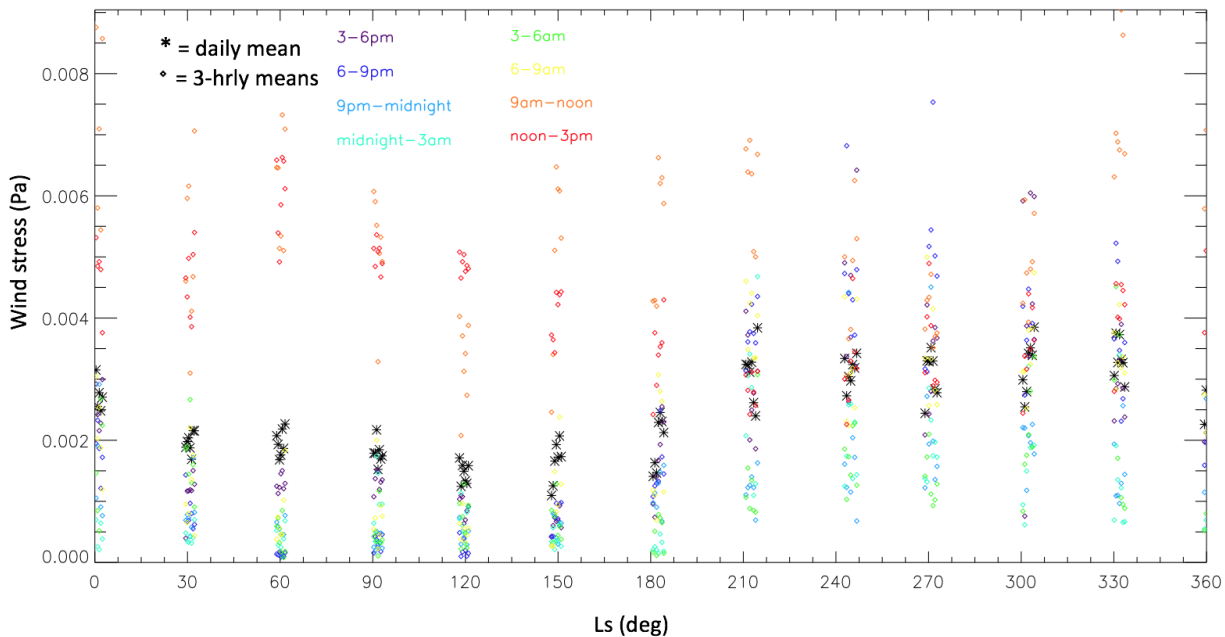


Figure 5: Wind stresses in 3 hour intervals as a function of L_s at Gale Crater, Mars.

1.6 Lowered saltation threshold on Mars

Note that the wind stresses predicted in Figure 5 rarely reach previously suggested threshold of 0.01 Pa by Ayoub et al. (2014) and the windspeeds recorded above are at least 25% lower than the 21.5 m/s employed in the lab (Thøgersen et al., 2019). Even so, saltation is possible due to lower Martian gravity. Once a sand grain is lifted, it is allowed to stay lifted for longer and receive more acceleration from the wind. In turn, it impacts the ground with higher kinetic energy, allowing for sustained jumps of the grain itself, and providing enough energy to other sand grains to be lifted as well (Sullivan and Kok, 2017). Surface overpressure may also be responsible for aiding the lifting of sand particles on Mars. Heat absorbed by gas in the subsurface through pores in the soil incites gas flow to the surface of the soil. The additional pressure caused by the gas flow has been shown to reduce the saltation initiation

threshold by 4-19% using Mojave Mars Simulant at martian pressure (Küpper and Wurm, 2015). Electric fields that exceed a certain threshold (150 kV/m on Earth) can lift sand particles up to 300 μm in size, based on experiments by Kok and Renno (2006). Furthermore, they can reduce the threshold frictional velocity required to initiate saltation by up to 30% (Kok and Renno, 2006). This may contribute to the prevalence of saltation on Mars, however, the effect of martian atmospheric conditions on these effects remains unclear. The impact threshold is known as the wind shear velocity required to maintain saltation and varies with particle size. The average particle size at Gale Crater is 100 μm (Baker et al., 2018). On Earth, the impact threshold is 82% of the saltation initiation threshold, however, on Mars, for 100 μm particles, it is approximately 5% (and goes up to 50% for larger sized particles) Kok (2010). In fact, Zheng et al. (2020) argue that the unevenness of a planetary surface like Mars would generate turbulent flow that allows saltation below the impact threshold. The combination of these mechanisms proposes that a lowered saltation threshold exists on Mars, and that these mechanisms allow widespread saltation on Mars.

The existence of a lowered saltation threshold on Mars was experimentally proven by tests in MARSWIT (Mars Surface Wind Tunnel), a 13 m long low pressure wind tunnel. To account for the reduced gravity on Mars, the tests made use of lower-density sand. The saltation threshold was defined as the point at which grains across the tunnel could sustain saltation. In this study, the closest particle size for comparison to Gale was 200 μm . For 200 μm particles, the windspeed required to pass the saltation threshold was found to be 15.07-19.51 m/s (Swann et al., 2020). The lower end of this windspeed range has been reliably measured by MSL, and smaller particles require even lower thresholds due to the lack of sand cohesion on Mars (Sullivan et al., 2008). As theoretical support, the Jackson et al. (2015) model was able to simulate ripple migration with local windspeeds between 7-12 m/s in Procter Crater, substantially lower than all other results. This highlights the role of localized winds and micro-atmospheric dynamics in saltation processes. The ripple migration calculated by Jackson et al. (2015) is also exponentially proportional to windspeed, supporting the reasoning of Sullivan and Kok (2017).

The magnitude of wind stress at night at Gale Crater is inconclusive, but the crater is a confirmed active saltation environment (Silvestro et al., 2013; Baker et al., 2018). Since the magnitude of glow is small, it is important to identify periods of high saltation throughout the Mars year, to maximize the potential of observing triboelectric discharge. These periods are defined by bigger and more frequent saltation events. In place of wind models and measurements, saltation events can also be detected using an observation already frequently conducted by MSL called the LOS (Line of Sight) observation. This thesis will use LOS data in Section 2 to present the highest resolution analysis of saltation events yet at Gale Crater, and is intended to support any future observation proposals for triboelectric discharge at Gale, by highlighting narrow L_s periods when saltation is highly active in the crater. An observation planned on a night within these periods would have the highest probability of capturing triboelectric discharge.

In section 3, this thesis assesses the detectability of the glow based on current experimental knowledge, and determines the theoretical limits each landed spacecraft’s cameras could place on the radiance of the glow. Additionally, archived nighttime images taken with MSL are analyzed to check if glow radiance has been observed previously on Mars, and future optimized observations are discussed.

1.7 Effects of Triboelectric Discharge on Trace Gas processes

Data from MSL shows evidence of a seemingly unique gas-surface electrochemistry that requires the occurrence of triboelectric discharge (Trainer et al., 2019). The role of triboelectric discharge in the crater can be seen from the oscillating trace gas data collected by the QMS (Quadrupole Mass Spectrometer) of the SAM (Sample Analysis at Mars) suite aboard MSL (Mahaffy et al., 2012).

The martian atmosphere consists mainly of CO_2 (95.3%) with small amounts of N_2 (2.7%) and Ar (1.6%) (Owen and Biemann, 1976). In addition, CO , O_2 , and CH_4 are found in trace amounts. CO_2 has a well-known global variation cycle at the surface as a result of sublimation and condensation of the gas in the polar regions (Tillman et al., 1993). As

CO_2 condenses out of the atmosphere in northern winter, the reduction in pressure pushes atmospheric gases out of the equatorial latitudes of the crater, resulting in a decrease of the volume mixing ratios. The reverse process occurs in the summer due to sublimation of CO_2 back into the atmosphere. However, due to the abundance of CO_2 molecules in the martian atmosphere, the changes in pressure only affect the volume mixing ratio of CO_2 in the crater by 1%; thus, in the context of gas-surface processes at Gale, CO_2 is unvarying (Trainer et al., 2019). N_2 and Ar are weakly cyclical, with mixing ratios varying by 10% over one year. In addition, the interannual measurements of these gases follow the same pattern and magnitude (Figure 6). Since these gases are highly unreactive, the seasonal variation can be attributed to the global transport cycle with which these measurements are well-aligned. CO measurements are unreliable at this time and are therefore not included in the analysis in Section 4 (Trainer et al., 2019).

However, O_2 measurements at Gale show high interannual variability and a pattern of potentially linear increase between L_s 0-150° followed by a drop to a constant lower level for the rest of the year, as shown in Figure 6 (Trainer et al., 2019). The inconsistency between years shows that the mixing ratio of the gas is subject to other phenomena in addition to the global transport cycle. More importantly, the rise of O_2 and instances of sharp decrease in the gas (MY33 L_s 141-161°) cannot be explained by photochemical reactions. Oxygen abundance is decided by a complex series of photochemical reactions involving the recombination and disassociation of CO_2 , H_2O , and OH radicals (Krasnopolsky, 2006). Oxygen creation by UV photolysis is too slow to explain the seasonal rise in levels and oxygen degradation purely from UV photolysis would have a lifetime of 60 years (Krasnopolsky, 2017). Trainer et al. (2019) suggest a local oxygen cycle at Gale where atmospheric oxygen is converted to oxidizing agents in the soil and released again. However, by their calculations, mechanisms such as perchlorate radiolysis and H_2O_2 soil adsorption are too slow to account for the oxygen variation. Furthermore, CH_4 , another trace gas, shows a 36% variation from the mean mixing ratio (Trainer et al., 2019), more than three times higher than the stable gases' variation. The fluctuation in the mixing ratio cannot be accomplished solely by global

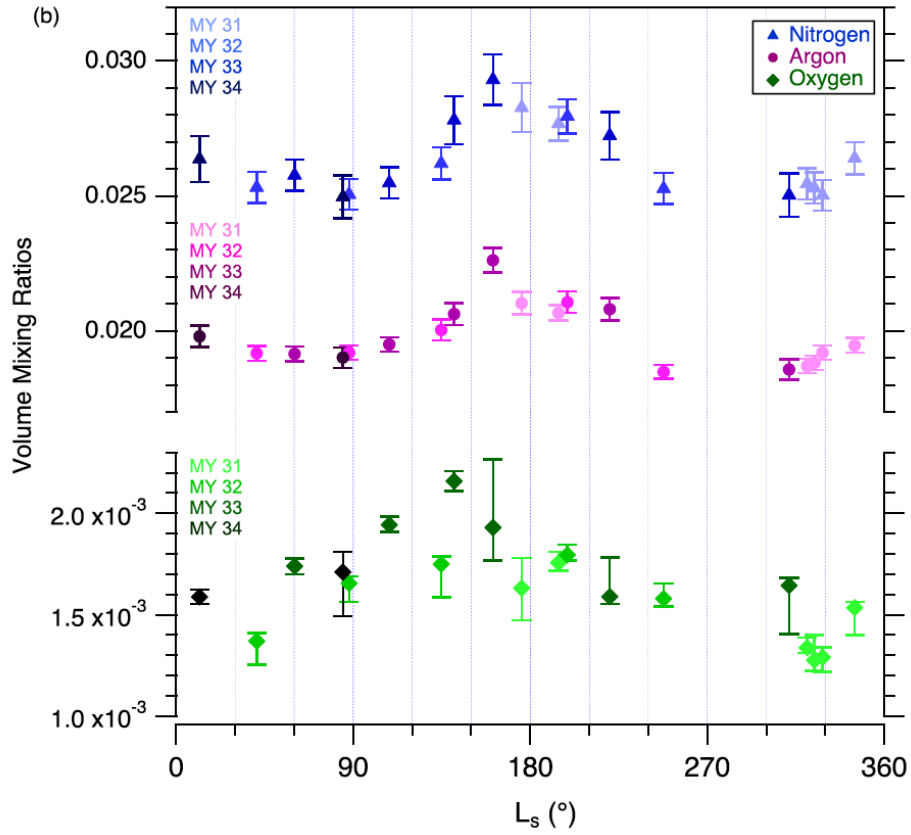


Figure 6: Taken from Figure 7b, Trainer et al. (2019). Seasonal trends in the instantaneous volume mixing ratios of the three most abundant noncondensable gases in the Mars atmosphere. Nitrogen (triangles), argon (circles), and oxygen (diamonds) are plotted versus L_s . Point shading corresponds with Mars year (light to dark) as indicated in the upper left corner of each plot. Error bars shown are 1 standard deviation (σ).

transport. The exaggerated fluctuation points to the existence of a degradation process stronger than UV photolysis, which would otherwise give methane a lifetime of approximately 340 years (Krasnopolsky et al., 2004). Both these gases currently show lifetimes of less than a year.

As such, there is a need for a fast destruction and replenishment mechanism to explain the behaviour of O_2 and CH_4 . Lab simulations show that saltation-induced triboelectric discharge is capable of producing strong oxidants, H_2O_2 and perchlorates, in the soil in the timescales required (Bak et al., 2017; Wu et al., 2018). Both oxidants have been directly detected on Mars (Lasne et al., 2016) and perchlorates specifically at Gale (Sutter et al., 2017). In addition to the atmospheric components, the unusual enhancement of perchlorates in the soil (found by SAM, Farley et al., 2016) demands a faster production mechanism than photochemistry. This thesis hypothesizes that triboelectric discharge is therefore the process responsible for the atmospheric removal of these gases and build up of oxidizing agents in the soil at Gale Crater. It ionizes the near-surface atmosphere, triggering a set of chemical reactions that use up oxygen to form oxidants, which then oxidize or ‘remove’ the methane. The details of the replenishment and destruction mechanisms of oxygen and methane are as follows.

1.8 Methane

Methane can be produced by volcanoes, comets and meteorites, hydrogeochemical serpentinization, and biogenic sources; the possible biotic origins of methane on Mars make it critical to understand the gas’s behaviour (Oze, 2005). Chemolithotrophs are organisms that consume CO and H_2 and produce methane. There is abundant CO and H_2 available in the atmosphere as well as H_2 produced from the hydration of silicates on Mars. These organisms could therefore be producing methane in present time on Mars or may have produced it in the past, with the molecule then being stored in its hydrate permafrost form (Atreya et al., 2007). Methane peaks measured at the northern pole during northern summer suggest that methane reservoirs exist in the permafrost (Fonti and Marzo, 2010; Geminale et al., 2011).

In addition, terrestrial methanotrophs, organisms that consume methane via oxidation, can theoretically survive in present martian conditions (Seto et al., 2019). The existence of a methane-producing, methane-consuming micro-ecosystem (Levin and Straat, 2009) is an exciting alternative explanation for the behaviour of oxygen and methane seen at Gale. Even if some dismiss the existence of methanotrophs, claiming that the bacteria would energetically favour CO reactions instead (Zahnle et al., 2011), methane is still one of the only signs in favour of life on Mars.

1.9 Methane Release/Replenishment

Methane stored under the surface can be released from existing fault lines and fracturing of the surface. The release of methane can be activated by seismic activity, wind storms, gas slugs, and fault burps. The rate of seepage is dependent on permeability of the soil and gas pressure gradients. Mars is thought to be a nearly drained seepage system and thus only experiences episodic seepage (Etiope and Oehler, 2019). Evidence of episodic seepage on Mars has been observed. Over the same region, no methane was detected by Villanueva et al. (2013) in January 2006 but a peak of 25 ppb was detected by Krasnopolsky (2012) in February 2006. Methane seepage resolves the observed ‘fast replenishment’ of methane.

1.10 Atmospheric Measurements of Methane

Orbiter and ground based detections of methane have been varied and sporadic. Methane on Mars was first detected in 1999 by the Canada-France-Hawaii telescope with a magnitude of 10 ppbv (Krasnopolsky et al., 2004). In 2003, a large plume of methane was seen with the equivalent volume of 19000 tons over the sites known as Arabia Terra, Nilli Fossae, and Sirtis Major from ground based telescopes (Mumma et al., 2009). Combining the total detection in the region should have resulted in 6 ppb of methane spread uniformly across the planet; however, in 2006, the mean mixing ratio was only 3 ppb (Mumma et al., 2009). The destruction lifetime was therefore found to be much shorter than 350 years, only about 4 earth years. Using the Mars Express Orbiter (MEx) Planetary Fourier Spectrometer (PFS),

Formisano et al. (2004) noted a spatial variation in methane of 0-30 ppbv from January to May 2004, suggesting that methane is controlled by localized sources/sinks.

MSL-SAM measurements in Gale Crater observe a background level of methane in the range 0.24-0.65 ppbv and occasional spikes as high as 9.34 ppbv (Webster et al., 2018). In comparison, the Trace Gas Orbiter (TGO) has failed to detect anything of the same magnitude, with measurements ranging 0.012-0.15 ppbv. However, it is important to note that MSL and TGO are measuring from two very different vantage points. MSL lies in Gale Crater, 2 km below the surface, very close to the equator and TGO obtained measurements 3-25 km above the surface (Korablev et al., 2019). The discrepancy is still puzzling as trace gases are rapidly mixed in the Martian atmosphere. Any trace gas from the surface is mixed to the top of the 10 km boundary layer in one sol. Progressing from that, global mixing takes place at a rate of 2-3 months (Korablev et al., 2019). However, in June 2013, only one of the two methane spikes detected by SAM-TLS was also detected by PFS. A 5.78 ppbv peak was detected by SAM on Curiosity mission sol 305 and immediately followed by a PFS detection of 15.5 ppbv on mission sol 306. However, the peak of 2.13 ppbv detected by SAM on sol 313 went undetected by PFS (Giuranna et al., 2019). The methane detected at Gale Crater is sometimes prevented from reaching the atmosphere, which suggests that Gale is a localized sink of methane.

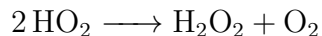
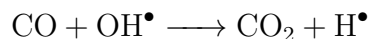
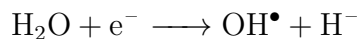
Viscardy et al. (2016) mapped the movement of methane based on a global circulation model that simulated Mars from the surface to a height of 150 km in 102 vertical levels. It took into account CO_2 ice mass, dust particle distribution, surface pressure cycles, and thermal emission. The model tested the outcome from an instantaneous (30 Mars minutes) emission of 5×10^6 kg at Nili Fossae at local noon, 10% of the quantity of the Mumma et al. (2009) plume. It assumed no previous methane was present in the atmosphere at the time. The plume was simulated to be released in the lowest vertical level, 38.9 m above the surface, at the same temperature and pressure as martian air at that altitude for simplicity. The methane dispersed horizontally at first, but in 5 sols, the methane had escaped the Planetary Boundary Layer (PBL). In just 20 sols, the methane had circled the planet. It is

then impossible to justify a plume detected by SAM to be undetectable by orbiters such as PFS or TGO in the days following its release.

The discrepancies call for a fast destruction mechanism that eliminates methane before it mixes in with the global atmosphere.

1.11 Oxygen and Methane Destruction Mechanism

The destruction mechanism of methane is triggered by triboelectric discharge; the charge build up in the dust contact ionizes surrounding gas molecules. Atreya et al. (2006) defines the process as this series of reactions:



Most notably, these set of reactions highly favour the disassociation of water vapour, which leads to the atmospheric enrichment of H_2O_2 , a highly oxidating agent of methane. In electric fields exceeding 20 kV/m, there is an H_2O_2 enrichment of $220\times$. H_2O_2 is also produced by the reaction of abraded silicates with atmospheric oxygen and the reaction of abraded silicates active sites with H_2O (Bak et al., 2017). Oxygen is thus used up by these reactions, representing an active sink for oxygen inside the crater. Although the density of CO_2 molecules eventually stabilizes because of the reattachment of CO and O^- ions, the density of H_2O molecules only decreases and the density of H_2O_2 ions only increases (Atreya et al., 2006).

As the density of H_2O_2 particles produced exceeds saturation, it condenses out of the atmosphere, reaching the surface, and “scavenging” the underground sourced methane seeps that pour out of surface cracks. When H_2O_2 diffuses into the soil, it can survive considerably longer than its atmospheric lifetime of two days. There has been no direct measurement of

the depth to which H_2O_2 can reach before extinction, but it would have a lifetime of 105 years if found at 2.3 m below the surface and have a surface concentration $10\times$ its atmospheric concentration, for example (Atreya et al., 2006). Since H_2O_2 is soluble in water, it can also be transported along the surface. Thus, H_2O_2 in the soil is not limited to the site of production and can form even more effective superoxides in the soil (Atreya et al., 2006). Methane is then scavenged by the combination of triboelectric discharge events across the surface and movement of oxidants in the soil.

Bak et al. (2017) confirmed the formation of H_2O_2 by saltation in a lab study. The samples used were each 10 g, a mix of quartz and basalt, and tumbled in a Mars-like atmosphere at a windspeed of 2 m/s and 8 mbar pressure. After 63 days in a 20 cm long ampoule, the H_2O_2 concentration was found to be 44.9 nmol/g. The significance of this quantity will be analyzed in Section 4.10. A second study simulated triboelectric discharge by applying voltage to two parallel copper electrodes inside a Mars chamber. For the first part of the experiment, the Mars chamber was fed Martian Simulate Gas and observed at 3-9 mbar pressure. As an independent confirmation to Thøgersen et al. (2019), emission spectra from a variety of ionic species were collected: CO_2^+ , CO^+ , O_I , H_{III} , H_{II} , OH , Ar_I , N_2 , and N_2^+ (where O_I is the first excited state of an oxygen atom). In the second part of the experiment, a pure CO_2 atmosphere at 3 mbar was used in the Mars chamber on an $NaCl$ sample to test the formation of perchlorates. Raman spectroscopy confirmed that $NaClO_3$ appeared as early as 15 minutes into the experiment. Further products such as Na_2CO_3 and $NaClO_4$ were produced at hour 3 and 4 respectively. After 10 hours, perchlorates were detected at all layers of the 3mm deep soil and 1/6 of the amount at the surface was detected in the bottom most layer. When the experiment was repeated using an $NaCl$ fused silica cell (representing salts in martian soil) as one of the electrodes, the yield was cut in half. Thus, other components of martian soil may diminish the conversion to perchlorates. The oxidation power of triboelectric discharge on Mars was determined to be up to $10^7\times$ the oxidation power of UV photolysis on Mars (Wu et al., 2018), fitting the description of a fast destruction mechanism well.

Encrenaz et al. (2019) noted a large decrease in H_2O_2 quantities using the IRTF telescope from May 2016 to July 2018. The 2018 measurement was in the middle of the MY 34 dust storm. In 2016, they observed 45 ± 10 ppbv of H_2O_2 in the northern hemisphere and no H_2O_2 in the southern hemisphere, with an upper limit of 10 ppbv. In 2018, an upper limit of 15 ppbv of H_2O_2 was observed across the martian disk, but it was mainly undetected. The depletion could very much be explained by large dust events during the global dust storm, depositing H_2O_2 on to the soil.

Thus, triboelectric discharge is suggested to be responsible for triggering a series of chemical reactions that cause the accumulation of strong oxidizing agents in the soil and ‘destroy’ methane. In addition, Thøgersen et al. (2019) determined that saltation was able to ionize Argon (15.76 eV), which has a higher ionization energy than all other gases noted here: H_2O (12.65 eV), CO_2 (13.78 eV), O_2 (12.07 eV), CH_4 (12.61 eV), CO (14.01 eV), and N_2 (15.58 eV) (Erman et al., 1993; Trickl et al., 1989; Berkowitz et al., 1987; Tonkyn et al., 1989; Wang et al., 1988; Snow and Thomas, 1990). The electrochemistry is therefore in favour of the chemical reactions listed above, and triboelectric discharge is able to ‘destroy’ methane but changing it directly into other ionic products such as CH_4^+ , CH_3 , CH_2 , and CH . Even though saltation is limited to a small height above the surface, the effects of triboelectric discharge reach beyond this restriction.

Gale Crater was found to have a much larger normalized pressure surface cycle, and a much shallower convective boundary layer than expected. It is an asymmetric crater placed at the edge of the hemispheric dichotomy, which leads to large pressure variations inside it. In turn, this results in much larger temperature extremes inside the crater (Tyler and Barnes, 2015). The lower temperature in the crater at nighttime due to radiative cooling reduces turbulent mixing and promotes molecular diffusion. The rate of this diffusion was calculated to be $9.4 \times 10^{-4} \text{m}^2/\text{s}$, which limits all atmospheric mixing to 16 m, creating a compressed nighttime planetary boundary layer at Gale (Moores et al., 2019). The reduction in volume undoubtedly forces a significantly higher number of gas particles into the saltation workspace at night, increasing the potential impact of triboelectric discharge.

1.12 Replenishment of Oxygen

At this time, there is no definite proposal of a 'fast replenishment' mechanism for oxygen, an issue that has been raised before (Zahnle et al., 2011). Trainer et al. (2019) calculated that 10^{20} oxygen molecules would need to be released back to the atmosphere seasonally to explain the increase in oxygen and cited three possible replenishment mechanisms. By their estimates, H_2O_2 soil desorption can provide 10^{19} oxygen molecules, a magnitude smaller than needed, but this number may be further reduced depending on the depth at which H_2O_2 exists in the soil. Perchlorate radiolysis can provide the needed magnitude of molecules but its reaction rate is too slow to recover the oxygen levels seasonally. Lastly, H_2O_2 is proposed to release oxygen rapidly upon humidification at temperatures of 10°C , but a lack of experimental data prevents numerical estimates of this mechanism. This author suggests that a combination of all three mechanisms may be occurring and could be sufficient to explain the increase in oxygen observed after depletion.

1.13 Overview

Oxygen and methane are fundamental to the existence of life on Earth; even though triboelectric discharge is an abiotic process, the activity of trace gases must be thoroughly explored as there may be biotic factors yet to be uncovered. In order to further our comprehension of near surface electrochemistry on Mars, this thesis provides an in-depth perspective of triboelectric discharge at Gale Crater. Section 2 analyzes the optimum environmental conditions when triboelectric charge is most likely to occur at Gale Crater. Section 3 describes the methods employed to ascertain the ability of present and future mission cameras to detect the glow. It also presents the radiance limits of each camera and analyzes past nighttime images from MSL to explore if observational conditions have been met in the past. In addition, it discusses the implications of this analysis on future measurements that can be conducted to capture triboelectric discharge. Section 4 assesses the possible effects of triboelectric discharge on trace gas processes inside the crater.

2 Analyzing saltation events with MSL data

2.1 LOS Dataset

The concentration of dust in the crater can be measured by the line of sight (LOS) extinction method. It is documented by the mission on a regular cadence with MSL’s NavCam and MastCam. Since saltation only occurs very close to the surface, its variation cannot be assessed directly. When saltation events take place, the sand grains also activate the dust in the crater. This is because smaller particles sit buried within the laminar sublayer and are difficult to pick up. Dust is released much more easily when it is released by impacts from saltating particles. This dust rises up to a greater height than the sand, and increases the concentration of dust up to the 2 km crater rim. The increased concentration of dust is reflected in the LOS observation, and suggests that saltation has taken place. Dust lifting can occur without saltation, but dust in the crater is certainly enhanced by saltation. Thus, by extracting a high resolution dust record and identifying periods of dust enhancement in the crater, we can extract periods of high saltation as well.

Over the course of the mission, the observation has been modified and expanded. From mission sol 100 to 1187, the observation was taken with only one camera, NavCam on MSL, and consisted of four images taken at the same pointing: the north rim of the crater (Moores et al., 2015). NavCam is a monochrome camera that operates in the near-infrared spectrum (600-800 nm) and has a wide $45 \times 45^\circ$ field of view. The two identical NavCams are situated on the mast of the rover, with a CCD of 1024 pixels \times 1024 pixels (Maki et al., 2012). The LOS images taken with NavCam are 512 pixels vertically and 1024 pixels horizontally. To calculate Line of Sight, the mean radiance of a patch in the sky, the mountains, and the ground was first separately extracted from 5 different points in the image, each 8 pixels wide (Moores et al., 2015). The optical depth was then derived using:

$$\tau = -\ln \frac{1 - I_s/I_m}{I_g/I_m - I_s/I_m} \quad (1)$$

where I_s is the radiance of the sky, I_m is the radiance of the mountains and I_g is the radiance

of the ground. Extinction directly follows as:

$$E = \tau/d \tag{2}$$

where d is the distance to the mountains and extinction, E , is measured in km^{-1} . The distance to the mountains was measured by a digital terrain model.

Equation 1 was developed with the following framework. The ground is on the order of 10s of metres away from the camera, and it is assumed to be made of the same material as the mountains. Thus, the ground is taken to be the radiance of the mountains if the optical depth were 0. The optical depth equations are simplified by comparing the sky brightness to the mountain brightness, where the sky is assumed to have infinite optical depth. They are comparable because both the path from the sky and the mountains to the camera is nearly horizontal, the Sun is shining from above, and the path length through the atmosphere to the mountains is one order of magnitude smaller than the path length from the mountains to the camera. The complete derivation is described in (Moores et al., 2015).

From the analysis of the first set of NavCam images, mission sol 100 to 1701, the crater was found to be horizontally homogeneous. In terms of vertical stratification, dust loading increased in concentration with decreasing altitude (Moore et al., 2019), an important result as it showed that resolvable dust lifting occurs in the crater, an effect that marks the occurrence of saltation. LOS extinction as a function of solar longitude over three Mars years shows a clear repeated seasonality; the dust loading is minimal at L_s 90° , maximum between L_s 310° and 315° , and ranges from 0.02 to 0.1 km^{-1} (Moore et al., 2019).

By mission sol 1187, LOS observations were expanded to include a MastCam-34 and MastCam-100 image, always taken in conjunction, and also pointed to the north of the crater. MastCam, also positioned on the mast of the rover, is equipped with R,G,B CCDs, operates in the visible to infrared spectrum, and is made up of two cameras: the left eye a 34 mm lens and the right eye a 100 mm lens. Both cameras contain several narrow-band filters and one broadband filter, the latter of which is used by LOS (Bell III et al., 2017). The MastCam CCD is 1648 by 1200 pixels, but the LOS images use a 1184×1184 pixel

subframe, which gives MastCam-34 a $15 \times 15^\circ$ field of view and MastCam-100 a $5.1 \times 5.1^\circ$ field of view. The most recent dust cycle record extends to sol 2556 in NavCam and 2662 in MastCam. The optical depth in these images is calculated by extracting all pixels with an elevation of $0\text{-}2^\circ$ as crater rim/mountain pixels, -3.5 to -10° as ground pixels, and 3.5 to 5.5° as sky pixels, thus producing a continuous extinction record (Smith, 2020). Figure 7 shows an example LOS observation image taken in each camera: NavCam, MastCam-34, and MastCam-100.



Figure 7: Example of LOS observation taken in each camera. (a) NavCam image taken on sol 2031 (b) MastCam-34 image taken on sol 2037 (c) MastCam-100 image taken on sol 2037. Images are not processed. Image Credit: NASA/JPL-Caltech/MSSS.

From Smith (2020)’s detailed comparison of the NavCam and MastCam-34 record from mission sol 100 onwards, several other variations in the dust concentration were revealed. When differentiating the observations by morning and afternoon, afternoon extinctions were found to be consistently higher, suggesting a potential diurnal variation in dust particle density at Gale. There is a noticeable depreciation in average extinction values from MY32 to 33 to 34. As found previously, the extinction values in NavCam stay between 0.08 and 0.1 km^{-1} in the extended analysis period, excluding the global dust storm. The MastCam-34 images detect a minimum slightly later in the year (L_s 100°) and a maximum slightly earlier in the year (L_s 240°), compressing the dust cycle. The amplitude of the cycle in the green

and blue filter is also compressed to 0.07 km^{-1} , which may be due to differences in dust particle sizes, but is not yet certain. In addition, the green and blue filters detect a small dip in values after the maxima at $L_s 240^\circ$, the reasons for which are still unclear (Smith, 2020). LOS images taken between 10:00-14:00 LTST were found to be more reliable, as images taken outside this window were more distorted by shadowing and lighting effects (Smith, 2020). During MY34, the year of the global dust storm, extinctions jumped to a peak of 1.07 km^{-1} in NavCam and 1.0 km^{-1} in MastCam on sol 2088 in the course of a few sols. The values then observed a slow decay lasting till approximately sol 2160 (Smith et al., 2019).

The images taken with MastCam-34 include the sky, crater rim, and ground. They provide good comparison to the NavCam images as shown in Figure 7. The two cameras have enabled us to understand the variation of dust in the crater with solar longitude, time of day, and azimuth well. However, as stated before, saltation is connected to dust lifting in the crater. For a greater understanding of the peak dust lifting in the crater, it is necessary to analyze a higher resolution image of vertical stratification of dust within the crater and its seasonal variation. MastCam-100 LOS images can be used for this purpose and have been thus analyzed for the first time in the next section.

2.2 Processing of MastCam-100 LOS Images

MastCam-100 images only include a view of the crater rim and a small portion of the sky (Figure 7c). These images enable the highest vertical resolution observation of dust lifting in the crater yet as many more pixels are dedicated to values in the crater rim. The three CCDs in the camera image the crater at different wavelengths: 638 nm (Red), 551 nm (Green), and 493 nm (Blue) (Bell III et al., 2017). These wavelengths are a few nanometers apart from the MastCam-34 filter wavelengths: 640 nm (Red), 554 nm (Green), and 495 nm (Blue), and therefore allow data from MastCam-34 to be used in the calculations of MastCam-100 as needed and explained below. As per the data availability on each mission sol, observations were taken in low-volume and high-volume formats. As a result, low-volume images were available from mission sol 1187 to 2310, and high-volume images were available from mission

sol 2013 to 2554. The images are combined into a single dataset, since Smith (2020) showed that the extinction results from both types of images are identical. Images between sols 2066 and 2175, the year of the global dust storm, have been excluded for this analysis, since equation (1) breaks down in extreme dust loading. A total of 460 images were analyzed in the MastCam-100 LOS dataset; 236 of these images fall between 10:00-14:00 LTST.

MastCam-100 images were downloaded from the Experiment Data Records (EDRs), and processed in the same way as MastCam-34 images in Smith (2020), but using right-camera specific parameters. Low-volume and high-volume data is processed differently because low-volume data is already de-bayered. The differences are highlighted in the steps below:

1. Low-volume images are downloaded as R, G, B frames. High-volume images are downloaded as one frame.
2. The frame(s) is decomanded from 8 bit to 11 bits, using the decomanding table provided in Bell III et al. (2017).
3. Dark current, equivalent to 3 DN (Digital Numbers), is subtracted.
4. Right camera flat field is subtracted for high-volume images. Individual R, G, B right camera flat fields are subtracted from each low-volume frame.
5. Cropped to 1184×1184 pixel subframe.
6. High-volume image is de-bayered using the Malvar et al. (2004) algorithm. High-volume image is split into R, G, B frames. Both types of images are now handled identically.
7. Hot and grey pixels listed in Table 6, Bell III et al. (2017) removed and replaced with mean of surrounding pixels.
8. Pixel value in DN converted to radiance (R) using coefficients (C_v) in Table 4, Bell III et al. (2017), by $R = \frac{P}{t} \times C_v$, where P is the pixel value, and t is the exposure time of the image in seconds.

For the tau calculation (equation 1), the pixel radiances of the crater rim were taken from the MastCam-100 image and correspond to pixels in the elevation range $0-2^\circ$. Compared to MastCam-34, on average, pixel radiances of the crater rim in the same region were $1.12\times$ higher in the red filter, $1.075\times$ higher in the green filter, and $1.045\times$ higher in the blue Filter. The MastCam-100 radiances were reduced accordingly. The mean sky radiance and ground radiance of the respective MastCam-34 regions of the corresponding MastCam-34 image was calculated. Equation (1) was then applied to each pixel in the MastCam-100 crater rim, thus computing a 2D subframe of taus equivalent to the size of the crater rim area. The distance to the crater rim for each pixel in this subframe was generated by a digital terrain model (DTM) (Gwinner et al., 2010), which was also used by Smith (2020). The DTM had a resolution of 50 m between two lateral pixels, which was much larger than the lateral distance between two lateral MastCam-34 pixels; to compensate, the DTM frame was then interpolated to match the resolution of the MastCam-100 image grid. Equation (2) then resulted in an equal sized 2D subframe of extinction values as a function of azimuth and elevation.

To understand the vertical variation of extinction, the subframe of extinction values was regridded and interpolated once more to numerical heights in metres instead of elevation angles. This was done to account for the movement of the rover. As MSL has traversed away from the crater rim, the $0-2^\circ$ elevation cutoff has encompassed a larger visible height of the crater rim within it. This is noticeable in Figure 9a, as the extinction bars' maximum rises from 1279 to 1404 m. The average height range encompassed by the pixels (and therefore dust in the crater) is 120 m to 1350 m above the surface of the crater whereas the DTM distances ranged from 20-32 km. 464 MastCam-100 pixels are dedicated to this height range, creating a resolution of 2.65 m/pixel, which is still insufficient to see saltation, but $\sim 3\times$ better than the MastCam-34 resolution of 7.64 m/pixel.

2.3 Associated Errors

The uncertainty of the 2D subframe of extinction values within one image was calculated using the rms method,

$$E_{rms} = \sqrt{\frac{1}{n} \times \sum_{i=1}^n (E - E_i)^2} \quad (3)$$

where n is the number of pixels, E is one of the extinctions in the subframe, E_i is the mean extinction of the subframe, and E_{rms} is the resulting root mean square.

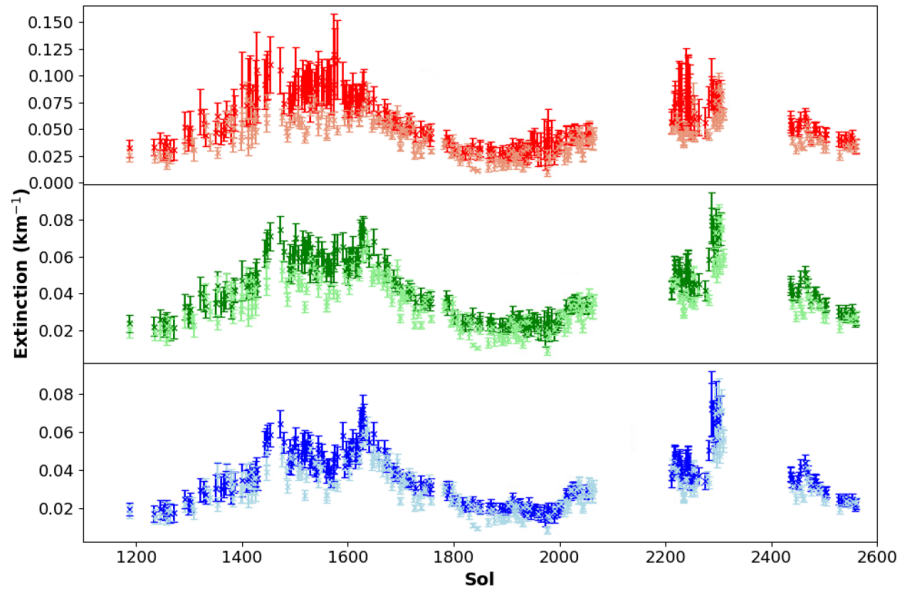
In addition, the tau calculation from equation (1) has an error of 4% compared to radiometric models (Moores et al., 2015) and the DTM has an accuracy of 50 m, both of which were added in quadrature,

$$E_{err} = \sqrt{\left(\frac{\tau \times 0.04}{\tau}\right)^2 + E_{rms}^2 + \frac{50.0^2}{d_{av}}} \quad (4)$$

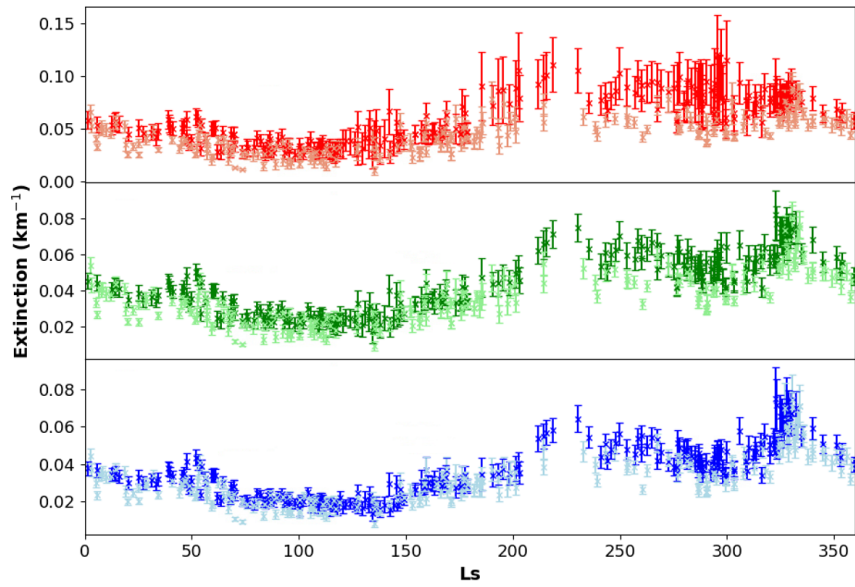
where E_{err} is the total percentage error associated with the extinction, τ is the mean tau of the image, and d_{av} is the average distance to the crater rim in the subframe. For extinctions between 10:00-14:00 LTST, the average extinction error was found to be 21.0% and ranged from 11.5 to 52.2 %. For the entire dataset, the average error was found to be 17.6%, and ranged from 6.1 to 52.2%.

2.4 Analysis of mean extinction variation

Figure 8 shows the variation of mean extinction (averaged along azimuth and elevation) with sol and L_s in each R, G, B filter, and represents a high resolution dust lifting variation map. The MastCam-100 LOS record spans 1400 sols, or just over two Mars years. Compared to the MastCam-34 analysis by Smith (2020), the maximum extinction values are slightly enhanced in each filter, and most prominent in the red filter, which has a maximum extinction of 0.14 km^{-1} in MastCam-100 as opposed to 0.1 km^{-1} in MastCam-34. These differences arise as a result of the radiation enhancement in MastCam-100 noted earlier and are exaggerated by the log factor in the tau calculations, but do not suggest an absolute difference in dust concentration measured by the camera. From sol 1200 to sol 1650, the extinction values



(a)



(b)

Figure 8: Mean extinction in R,G,B filter (from top to bottom) and as a function of (a) sol and (b) L_s plotted with error bars. Darker coloured points are data observed between 10:00-14:00 LTST. Lighter coloured points are data observed outside of this window.

steadily increase, except for the small dip in the green and blue filters. The extinction values then steadily decrease with much less variation amongst data points till sol 1900. From sol 1900 to sol 2600, the data also undergoes this rise and decline, but has two large gaps: one for the global dust storm and another due to lack of available observations. However, the repeatability of the data is confirmed by the L_s plot, as the data points of the two years cluster tightly over each other. The extinctions between 10:00-14:00 LTST are consistently higher than those outside of that window in each filter. This analysis is in complete agreement with the results of Smith (2020). It is harder to accurately place the maximums and minimums of these plots compared to the MastCam-34 plots. All three filters undergo a period of near-minimum extinction values from L_s 75 - 130°, and a period of high extinction values from L_s 210 - 325°. The same dips that appear from sol 1400-1650 appear in the L_s 275 - 325° range in the green and blue filters. Smith (2020) has suggested that these dips could represent different filter wavelengths being sensitive to different dust particle sizes, systematic underestimation by the green and blue filter, or the the result of MSL’s increase in elevation along its traverse. The sudden peak at L_s 325° may be caused by imperfections in the DTM, as the terrain changes vertically and horizontally with each sol. However, if this data result is not erroneous, this peak could be the result of a temporary high stress regional wind that the meso-scale circulation models are unable to simulate due to their low resolution as discussed in Section 2.1.

2.5 Analysis of vertical extinction variation

Figures 9, 10, and 11, are made up of extinction values from observations between 10:00-14:00 LTST, to ensure the reliability of the analysis. The entire extinction dataset is presented in Appendix B. Figures 9a, 10a, 11a plot the vertical extinction values averaged across azimuth but correlated to height in R,G,B filters respectively. Figures 9b, 10b, 11b use a linear interpolator to show a continuous variation of vertical extinction with sol and L_s .

When the data is averaged across one axis, azimuth, the maximum red filter extinction values increase to 0.16, while the other two filters do not show any change. MY 34 is, on

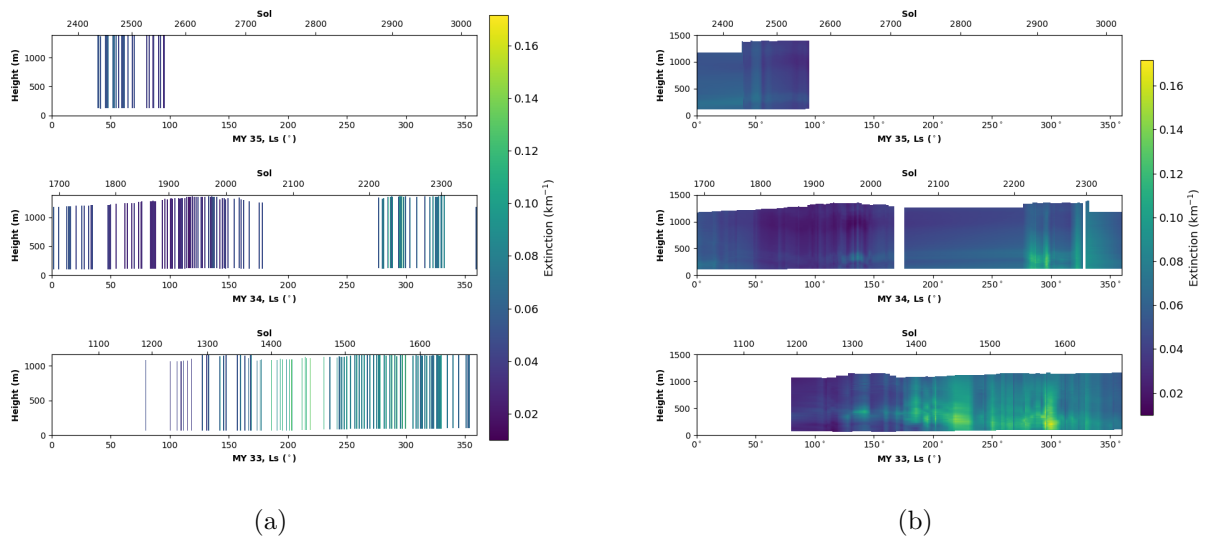


Figure 9: Variation in Red Filter Vertical Extinction at Gale with sol and L_s . X-axis represents height above the surface of the crater. (a) Each vertical line is the extinction calculated from one LOS image, averaged across azimuth. (b) Linear interpolation on individual extinction bars across the entire sol span of the data. Pixel radiance is represented by colour bar intensity.

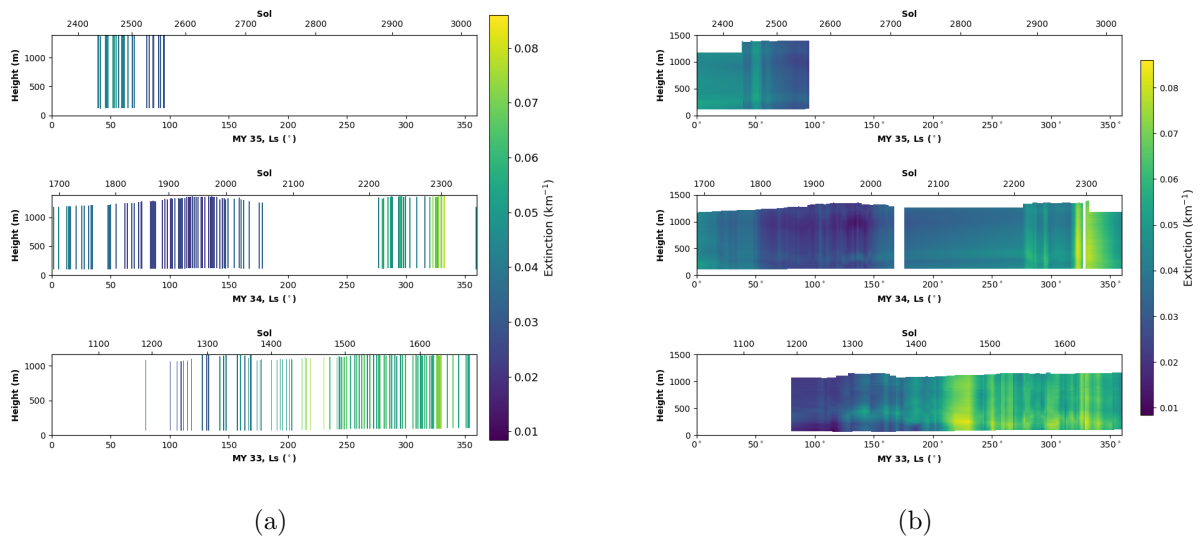


Figure 10: Variation in Green Filter Vertical Extinction at Gale with sol and L_s . X-axis represents height above the surface of the crater. (a) Each vertical line is the extinction calculated from one LOS image, averaged across azimuth. (b) Linear interpolation on individual extinction bars across the entire sol span of the data. Pixel radiance is represented by colour bar intensity.

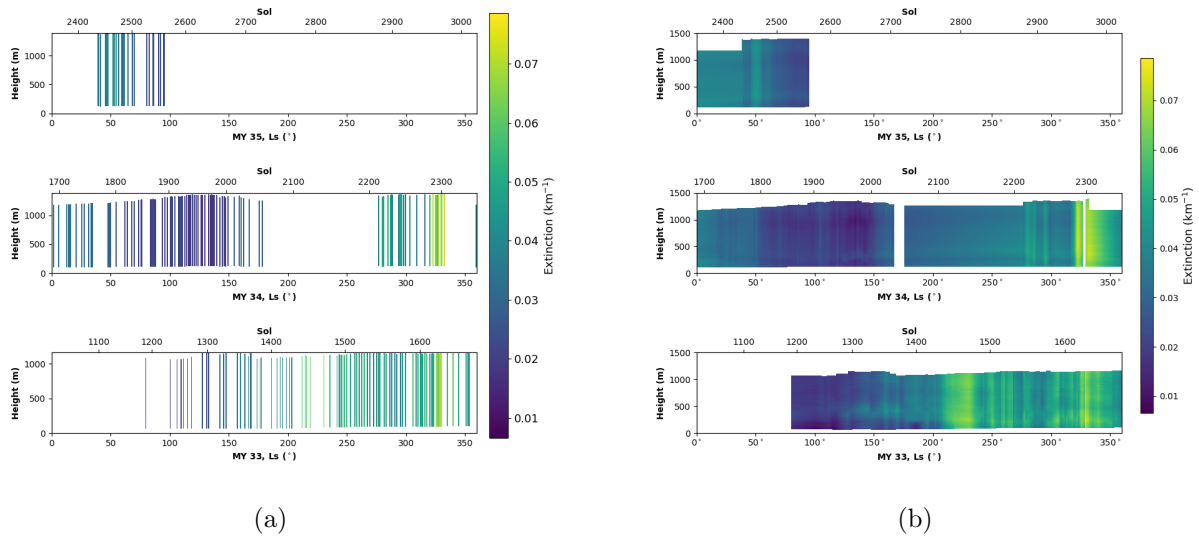


Figure 11: Variation in Blue Filter Vertical Extinction at Gale with sol and L_S . X-axis represents height above the surface of the crater. (a) Each vertical line is the extinction calculated from one LOS image, averaged across azimuth. (b) Linear interpolation on individual extinction bars across the entire sol span of the data. Pixel radiance is represented by colour bar intensity.

average, darker across the whole year, showing a lower overall dust concentration than MY 33, a diminution that has also been confirmed before. This may be explained by the onset of the global dust storm, which removed dust from inside the crater. The annual dust cycle minimums and maximums do not change position in the MastCam-100 vertical extinction plots. MY35 and MY34 reaffirm that the first half of the year has minimal dust lifting. MY 33 depicts an increase in dust lifting past L_s 150° and consistently high values past L_s 200°, both of which are expected from previous analysis. The multi-year observation has built up considerable data and is now able to show dust lifting repeatability in the crater; for example, the same dust lifting peak at L_s 325° is observed in MY34 and 33. The high intensity line visible at 250 m in MY33 and throughout MY 34 is likely a feature on the crater wall, as proposed by Smith (2020). The vertical extinction plots of the entire dataset in Appendix A do not show any discernible differences from Figures 9, 10, and 11: the linear interpolation in the smaller, afternoon dataset follows the same pattern as the non-interpolated extinction bars in the appendix plots.

In terms of identifying periods of potentially highly active saltation, MY33 shows consistently high extinction values below 500 m, or sustained dust lifting, after L_s 200°, which is the windy season. The concentration of high extinction values below 500 m carry upward in several sections of the second half of MY 33 and a few sections in MY34, suggesting large saltation events that are able to lift dust to the top of the crater. Particularly big dust lifting events are noted at L_s 225° and 300°. The blue filter shows an additional peak at L_s 325°, and the green an additional peak at L_s 250°. The green filter has the largest area of high extinction values, followed by blue, and then red. The red filter, as a result of the bigger range in scale, may be the most helpful in pointing out the most active saltation periods. An observation should attempt to fall in specific periods of high extinction values found in the red filter: L_s 181-189°, 191-197°, 201-203°, 216-221°, 249-252°, 257-268°, 276-282°, 286-291°, 295-303°, 315-321°, and 328-332°. Unfortunately, these L_s periods are based on the data of only MY33; as more data is available for the second half of MY35, it can add validity to these patterns. Compared to MastCam-34 images, which show high extinction values vertically

and horizontally across the second half of the year, the red filter of MastCam-100 images is able to highlight much more narrow periods of dust lifting.

The process of this work discloses the difficulties involved in confirming that saltation has taken place in the crater at a specific time and day. A rover camera cannot be dedicated to observing sand particles in motion near the surface of the crater due to limited resources. The vertical extinctions presented here are an attempt to continuously record dust lifting activity, and by extension saltation activity, to the resolution of one sol. However, this data still does not differentiate between night and day or hourly variations, both of which would significantly aid the planning of a real observation. Furthermore, this data only tackles temporal variations, and there is no existing data that can help us understand the spatial variations in saltation activity. Saltation should be ubiquitous on Mars because of the topography discussed earlier, however, the average area covered by saltation events in the crater and the number of simultaneous locations that events frequently occur at is unknown. Without this information, the observation cannot be planned with precision. And due to the limited resources on MSL, any attempt to increase the spatiotemporal coverage of the observation comes at a high cost. This is the first of many hurdles involved in directly observing triboelectric discharge.

3 Ability of mission cameras to detect Triboelectric Discharge

Cameras from three spacecraft are considered in this section: the MSL rover, the Mars 2020 rover, and the InSight lander. MSL is equipped with six engineering cameras: front and back HazCams and front Navcams. The HazCams and NavCams are monochrome cameras that operate in the visible spectrum and have a wide field of view. The NavCams are situated on the mast whereas the HazCams are positioned between the wheels of the rover (Maki et al., 2012). In addition, four other cameras on the rover are considered for the observation: MAHLI (Mars Hand Lens Imager), MARDI (Mars Descent Imager), MastCam and ChemCam RMI (Remote Micro-Imager). These cameras are equipped with R,G,B CCDs, operate in the visible to infrared spectrum, and have a range of fields of view. Mars 2020 is set to land at Jezero Crater in February 2021 (Nelessen et al., 2019). MastCam-Z on Mars 2020, an updated version of MSL’s MastCam, will also be assessed (Bell et al., 2020). InSight, which landed at Elysium Planitia in November 2018 (Golombek et al., 2016), has a total of two cameras, both of which will be evaluated: the Instrument Deployment Camera (IDC) on the arm is similar to NavCam on MSL and the Instrument Context Camera (ICC) is similar to HazCam on MSL (Maki et al., 2018a). Only those camera-filter combinations that had spectral widths covering a significant portion of the Ar laboratory spectra were included (Fig. 12).

3.1 Predicted Signal Strength of the Discharge Glow

The signal strength measured by a camera-filter combination is indicative of how effectively it can capture triboelectric discharge. The measured flux of glow discharge from lab simulations is converted into the number of electron/s produced by the detector, given the individual optical parameters of the camera and filter. The ‘signal’ or number of counts recorded by the detector is directly proportional to the number of electrons produced by the detector; counts are measured in Digital Numbers per second (DN/s). This method enables a direct

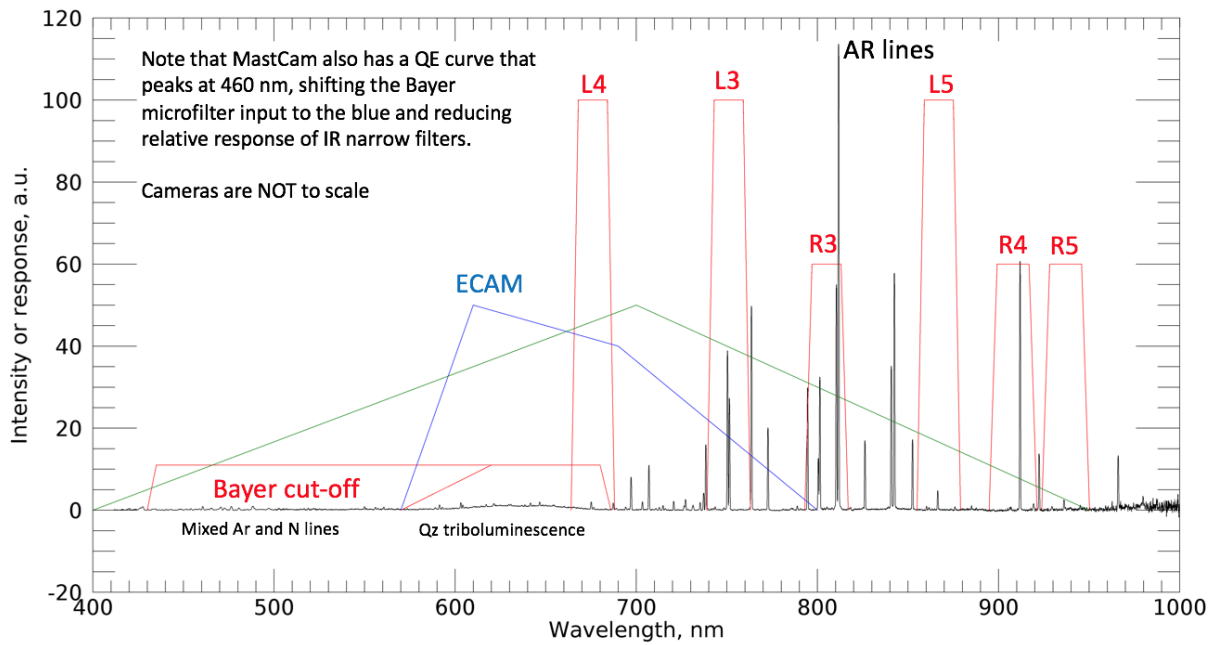


Figure 12: Spectral sensitivities of MSL’s cameras overlaid on to Ar spectra (Ar spectra taken from Thøgersen et al. 2019). Intensity response is in arbitrary units. ECAM represent the engineering cameras. Bayer-Cutoff represents MastCam-L0 filter. The red columns are respective MastCam filters.

comparison between cameras with very different optical characteristics. The signal strength was determined by the following set of equations, beginning with the known flux of an object such as the glow, which is $10 \mu\text{W}/\text{m}^2$. Since it is radiating in all directions, the radiance (I) is:

$$I = \frac{F}{4\pi} \quad (5)$$

where F is the glow flux. Given this radiance, the flux per pixel (F_{pp}) reaching the camera is:

$$\Omega = \frac{\theta^2}{a} \quad (6)$$

$$F_{pp} = I\Omega \quad (7)$$

where Ω is the solid angle per pixel in Sr of the camera, θ is angular size of the field of view of the camera in radians, and a is the area of the detector in pixels. The energy reaching the detector is:

$$A = \pi\left(\frac{d}{2}\right)^2 \quad (8)$$

$$E = F_{pp}A \quad (9)$$

where d is the diameter of the camera aperture. The photon energy stored in the central wavelength of the camera is:

$$E_\lambda = \frac{hc}{\lambda} \quad (10)$$

where h is Planck's constant, c is the speed of light, and λ is the central wavelength of the camera. Dividing the total energy by the energy of a photon at the effective wavelength of the camera-filter combination as per the Planck-Einstein relation, gives the number of photons per second reaching the detector.

The number of electrons/s released is the product of the number of photons and the quantum efficiency (QE) of the detector. The signal strength of the glow in a given camera filter is the number of electron/s produced by the detector divided by the gain (g). For

example, Mastcam-34 with the L3 filter has a field of view of 0.262×0.262 radians, a CCD consisting of 1200×1200 pixels, an effective wavelength of 751 nm, and a gain of 16e-/DN (Digital Number). Using equations 5-10, this corresponds to a glow signal strength of 0.0189 DN/s.

The final equation becomes

$$E = \frac{F\theta^2}{4\pi a} \times \pi\left(\frac{d}{2}\right)^2 \times \frac{\lambda}{hc} \times \frac{QE}{g} \quad (11)$$

A summary of camera specifications for MSL is displayed in Table 2. The reflectance refers to the fraction of light reflected by the martian surface for the central wavelength of the camera. For ChemCam, the QE and transmission factors are given separately, and so must be multiplied together to get the final QE. For cameras/filters with a flat spectral sensitivity across a large range of wavelengths, the central wavelength was taken to be the numerical average of the minimum and maximum of the range, specifically applied to ChemCam, MAHLI, MARDI. In some cases, the aperture diameter is provided. In other cases, the focal length is divided by the f number to get the aperture value. For ChemCam RMI, the FOV is an area bigger than 20 cm at 10 m (Maurice, 2012, p. 13), which gives a minimum FOV of $1.146 \times 1.146^\circ$. For cameras with an additional Neutral Density (ND) filter,

$$N_{Psf} = \frac{N_{Psi}}{10^{NDv}} \quad (12)$$

where N_{Psf} is the number of photon/s after the ND filter, N_{Psi} is the number of initial photons/s, and NDv is the value of the ND filter.

The summary of camera parameters for relevant Mars 2020 cameras and InSight can be found in Table 3.

3.2 Theoretical Radiance Limits

The radiance limit is the minimum radiance an object is required to have to be at the noise level of the camera. To derive the limits, the calculations described above must be applied in reverse, taking the dark noise of the camera for a specific temperature and exposure time in DN/s as the signal.

Table 2: Summary of Camera Parameters for MSL

	Haz Cam	Nav Cam	MARDI	Mast Cam 34 L0	Mast Cam 34 L3	Mast Cam 100 R3	MAHLI	Chem Cam RMI
FOV (de- grees)	124 × 124	45 × 45	70 × 52	15 × 15	15 × 15	5.1 × 5.1	31.1 × 23.3	1.146 × 1.146
CCD pix- els	1024 × 1024	1024 × 1024	1600 × 1200	1200 × 1200	1200 × 1200	1200 × 1200	1600 × 1200	1024 × 1024
Gain (e-)	50	50	15.8	16	16	15.8	16.19	13
Read Noise (e-)	25	25	17.5	18	18	15.8	17.89	40
Preferred Exposure (s)	180	180	180	180	180	180	180	40
QE (%)	43	43	40	45	15	10	38	1.44
Aperture (mm)	0.37	1.25	3.23	4.25	4.25	10	2.15	110
Central Wave- length (nm)	650	650	537	590	751	805	532.5	700
Spectral Bandpass (nm)	600 - 800	600 - 800	399 - 675	420 - 680	733.5 - 768.5*	790 - 825*	395 - 670	450 - 950
Reflectance (%)	26.11	26.11	14.97	21.21	28.98	29.60	14.28	27.83
ND filter	1.1	1.3	-	-	-	-	-	-
Ref.	1	1	2	3	3	3	4	5

1: Maki et al. (2003, p. 3,4,5,7), Maki et al. (2012, p. 4), Bell et al. (2003, p. 17); 2: Malin et al. (2017, p. 514,532, 534); 3: Bell III et al. (2017, p. 397,398,399,403,409), Malin et al. (2017, p. 514), Malin et al. (2005); 4: Edgett et al. (2012, p. 262), Edgett et al. (2015, p. 59,64); 5: Maurice et al. (2012, p. 13,25,26,27,33,35), Langevin et al. (2013)

* estimated from Malin et al. (2017, p. 516)

Table 3: Summary of Camera Parameters for InSight and Mars2020

	InSight IDC	InSight ICC	Mast Cam-Z L0-B	Mast Cam-Z L3	Mast Cam-Z L2	Mast Cam-Z L1	Mast Cam-Z R2
FOV	45×45	124×124	23×18	23×18	23×18	23×18	23×18
CCD pixels	1024×1024	1024×1024	1600×1200	1600×1200	1600×1200	1600×1200	1600×1200
Gain (e-)	50	50	16	16	16	16	16
Read Noise (e-)	25	25	21	21	21	21	21
Preferred Exposure (s)	180	180	180	180	180	180	180
QE (%)	8.0	8.0	32.5	20.0	12.0	8.0	5.0
Aperture (mm)	1.25	0.37	3.5	3.5	3.5	3.5	3.5
Central Wavelength (nm)	500	500	476	677	754	801	866
Spectral Bandpass (nm)	400 - 700	400 - 700	430 - 522	666 - 688	744 - 764	792 - 810	856 - 876
Reflectance (%)	22.15	22.15	8.70	27.23	29.00	29.58	29.64
ND Filter	-	-	-	-	-	-	-
Ref.	1	1	2	2	2	2	2

1: Maki et al. (2018a, p. 3,8,9), Maki et al. (2018b); 2: Hayes et al. (2020), Bell et al. (2020);

*central wavelength of blue filter selected for InSight Cameras, as lab spectra is shown in visible range, 420-500 nm, corresponding to the blue filter coverage

*MastCam-Z wide view parameters have been chosen as that is most suitable for the observation

The total noise for a given camera is the sum of read noise and thermal noise. Thermal noise in electrons is estimated by multiplying the dark current of each camera for a given temperature and exposure by the gain. Each camera has a dark current relation that can be used to find the total dark noise of the camera in DN. This value should be divided by the correct exposure time so that it is in units independent of time (DN/s). For ChemCam RMI, no dark current formula is provided but the dark current as a function of temperature is presented for 10 s and 1 s exposures in Maurice et al. (2012, p. 26). The ratio ($10 \times$) of the dark current values of these two functions at a specific temperature is taken as the ratio by which the exposure affects the dark current value. This is then extrapolated to the necessary exposure time, in this case 40 s, or $4 \times$. Even though the triboelectric observation would benefit from the collection of as many photons as possible or the longest possible exposure time, the camera would be saturated by photons much before this, which must be taken into account. For all cameras aside from ChemCam RMI, a balanced exposure time is 180 seconds. For RMI, based on the saturation chart, a good exposure time is 40 seconds (Maurice et al., 2012, p. 27). These exposure times are for an observation designed specifically to look for glow as they maximize the number of photons that can be collected by the detector before saturation occurs. Radiance values are calculated for -10, -20, and -30°C. The uncertainty of MastCam dark noise is ± 5 DN (Bell III et al., 2017, p. 404). If propagated through the dark noise calculations, the uncertainty of the MastCam radiance limits is $\pm 0.55 \mu\text{W}/\text{m}^2/\text{Sr}$. No other dark noise uncertainties are available. Given the MastCam uncertainty, all radiance limit values will be rounded to the nearest integer.

3.2.1 Comparison with Phobos Shine

For comparison, the radiance of Phobos reflected off the ground at the central wavelength of each camera was calculated as Phobos is the next brightest object after triboelectric discharge at night. These calculations are intended to derive the maximum radiance of Phobos for simplicity. For each camera, the ASTM G173 solar spectrum (ASTM, 2012) at zero airmass was integrated over the respective spectral bandpass (found in Table 2) of the

camera, and were adjusted to the distance of Mars at perhelion (1.377 au):

$$F_{MP} = F_E \left(\frac{1 \text{ AU}}{1.377 \text{ AU}} \right)^2 \quad (13)$$

where F_{MP} is the solar spectrum flux at Mars perhelion, F_E is the solar spectrum flux at Earth, and 1.377 AU is the known distance of Mars perhelion from the Sun (NASA, 2020a). The resulting flux is then reduced by the albedo of Phobos's surface, the value of which is 0.07 (Simonelli et al., 1998), and the amount of light reaching the top of the martian atmosphere.

$$F_{MT} = F_{MP} A \left(\frac{11.267 \text{ km}}{5844.5 \text{ km}} \right)^2 \quad (14)$$

where F_{MT} is the flux at the top of the martian atmosphere, A is the albedo, 11.276 km is the radius of Phobos, and 5844.5 km is the closest approach of Phobos to Mars, calculated by subtracting the radius of Mars (3389.4 km) from Phobos periapsis distance (9234 km, NASA, 2020b). The flux reaching the martian surface is attenuated by the atmospheric optical depth, which in these calculations was taken to be 0.5 (Smith and Lemmon, 1999), and Phobos' apparent zenith angle from the observer's perspective. Phobos has an equatorial orbit, which simplifies this geometry. For an observer at the latitude of MSL, 4.44° South (Grotzinger et al., 2012), Phobos will rise to 85.56° in the sky. The zenith angle in this case is the angle between south pole and Phobos, which is again 4.44°. Taking into account the additional airmass and projection of light at this zenith angle, the flux reaching the martian surface can be found by:

$$F_{MS} = F_{MT} e^{-0.5/\cos(4.44)} \cos(4.44) \quad (15)$$

where F_{MS} is the flux reaching the martian surface. The radiance of Phobos reflected off the ground, with respect to each camera, is found by:

$$I_{phobos} = F_{MS} R_\lambda \quad (16)$$

Where I is the radiance and R_λ is the reflectivity of the martian surface (McCord and Adams, 1969) corresponding to the central wavelength of the respective camera. The radiance is also

affected by the incidence angle of Phobos’s light on the surface. However, as that changes over the course of each sol, it was not included in this calculation; the magnitude of radiance here refers to when Phobos is directly overhead and is thus a maximum value.

3.3 Archival Datasets

Since MAHLI and MastCam showed the best sensitivities to glow discharge (see Section 3.4), nighttime images taken with MAHLI and MastCam over the course of MSL’s mission were analyzed. Night was defined as any image taken after sunset on that sol. MAHLI nighttime images were characterized by all 3 LEDs being in the off state. Nighttime images of MastCam were available on Sols 529, 783, and 2561. A total of 570 images were found on these sols and 52 night images were carried forward for the analysis. Nighttime images of MAHLI were available on sols 165, 910, 935, 1337, 2018. A total of 1447 images were found on these sols and 23 night images were carried forward for the analysis.

MastCam images used were EDR products with no modifications. Only Type C (lossless) or Type E (JPEG 422) images were used, as these are full size images. A series of steps were applied to remove hot pixels, remove flatfield background, rotate the image, etc. as in (Smith et al., 2019). Each pixel value was converted to a radiance value by the factors listed in Bell III et al. (2017), which have an error of approximately 10%. Only images in the L0 filter were analyzed as no images could be found in the L3 or R3 relevant filters.

MAHLI images used were RDR (Reduced Data Record) products, or 16-bit depth (per band) relative radiometric calibrated color images (Edgett et al. 2015). Only Type C (lossless) or Type E (JPEG 422) images were used, as these are full size images. A series of steps were applied to convert each pixel value to a radiance value that is comparable to MastCam (described in Appendix A). The root-mean-square of these radiance factor conversions is 1-2%.

Flatfielding and dark current estimations of both these cameras are handled by the respective instrument teams. They conduct these tests using replicas of the flight instruments in lab. Flatfield files, provided by the instrument teams, are uniformly used on all images.

3.4 Theoretical detection limits and camera suitability

3.4.1 MSL

Table 4: Summary of Camera signal strength of triboelectric discharge, FOV, and pointing capabilities

Camera	Signal Strength DN/s	FOV (degrees)	Ability to point?
MastCam L0	0.0445	15 × 15	Yes
MAHLI	0.0254	31.1 × 23.3	Yes
MastCam L3	0.0189	15 × 15	Yes
MARDI	0.2557	70 × 52	No
MastCam R3	0.0088	5.1 × 5.1	Yes
ChemCam RMI	0.0112	1.146 × 1.146	Yes
HazCam	0.0008	124 × 124	No
NavCam	0.0008	45 × 45	Yes

Table 4 presents the estimated signal strength (in DN/s) of the glow for each of the cameras on-board MSL that could be used to observe triboelectric discharge. The table is arranged in descending order of suitability for observing the glow, with the most suitable at the top and least suitable at the bottom. The suitability takes into account signal strength in DN/s, field of view, and the ability to point. A wide field of view and large range in possible pointing directions provides flexibility when taking the observation. A high DN/s increases the likelihood of detecting the glow’s faint signal. While the signal strength is critical to maximize, it cannot be considered independently of the field of view of the camera, since the precise location of saltation events cannot be known in advance. The MastCam L0 filter records the highest signal strength, has a sizable field of view, and has the ability to point in any direction, making it the most suitable of MSL’s available cameras to place observationally-derived limits on the glow radiance. MAHLI is listed second in suitability as

it has the second highest signal strength and an even wider field of view. The disadvantage of MAHLI is that it requires significant power usage of the robotic arm to point it. However, in its stowed state, it points at the horizon and includes significant foreground of the surface, which would be sufficient to observe triboelectric discharge. MastCam L3 is placed next in order of signal strength, while still retaining the ability to point and wide field of view. MARDI, despite having a signal strength one order of magnitude higher than any other camera, is not suitable as it points strictly downward and cannot be adjusted. It is unlikely that the rover will capture saltating particles directly beneath itself. MastCam R3 is more suitable than ChemCam RMI despite the superior signal strength of the latter, because it offers a wider field of view, which increases likelihood of observing triboelectric discharge. HazCam and NavCam prove to have too poor a signal to noise ratio to be considered suitable to observe or place meaningful limits on the magnitude of the triboelectric discharge, in spite of their large FOVs, and so are placed last.

Though the numbers in Table 4 predict that the magnitude of glow is two orders of magnitude below the detection limit of the cameras, and therefore the detection of glow will not be possible, an observationally derived upper limit for the glow can be obtained. Table 5 shows the theoretical radiance limits of MSL cameras at different temperatures for the exposure times recommended in Section 2. If a mission camera were employed to observe triboelectric discharge and glow could not be captured by the camera, the upper limit of the glow would be defined as the radiance limit of that camera at the corresponding temperature. The radiance of Phobos at the effective wavelength of the camera is added here for comparison. The lowest radiance limits in the table are one order of magnitude above Phobos's radiance reflected off the ground. MARDI is calculated to achieve the lowest radiance limit, but its downward pointing prohibits it from consideration as a candidate for this observation. The next two lowest radiance limits are MastCam L0 and MAHLI, which correspond to the two highest ranked cameras in Table 4.

Table 5: Summary of Radiance Limits of each Camera on MSL

Camera	Radiance ($\mu\text{W}/\text{m}^2/\text{Sr}$) at -10°C	Radiance ($\mu\text{W}/\text{m}^2/\text{Sr}$) at -20°C	Radiance ($\mu\text{W}/\text{m}^2/\text{Sr}$) at -30°C	Phobos Radiance ($\mu\text{W}/\text{m}^2/\text{Sr}$)	Glow Radiance ($\mu\text{W}/\text{m}^2/\text{Sr}$)
MastCam L0	52.0	42.0	36.0	8.23	0.8
MAHLI	50.0	50.0	50.0	5.91	0.8
MastCam L3	122.0	96.0	85.0	1.07	0.8
MARDI	6.0	6.0	6.0	6.19	0.8
MastCam R3	269.0	204.0	175.0	0.97	0.8
ChemCam RMI	316.0	261.0	N/A	16.53	0.8
HazCam	28956.0	11333.0	4450.0	6.22	0.8
NavCam	19263.0	7540.0	2960.0	6.22	0.8

*ChemCam RMI dark current data is not available for temperatures below -20°

3.4.2 Other Spacecraft

The Insight IDC and ICC cameras have a radiance limit of 3104.0 $\mu\text{W}/\text{m}^2/\text{Sr}$ and 4666.0 $\mu\text{W}/\text{m}^2/\text{Sr}$ respectively at -10°C , and thus would not be able to impose meaningful limits on the glow radiance. Since the Mars 2020 dark noise formulas are not available yet for MastCam-Z, an analysis of signal strength as in Table 4 was done instead. For reference, the signal strength of the MastCam filters on MSL have also been listed in Table 6. The MastCam-Z filters do not show an improvement in signal strength compared to the MSL MastCam filters; their radiance limits will be on the same order of magnitude to that of MastCam.

Table 6: Comparison of signal strength of triboelectric discharge in MastCam on MSL and MastCam-Z on Mars 2020

MastCam Filter on MSL	Signal Strength (DN/s)	MastCam-Z Filter on Mars2020	Signal Strength (DN/s)
L0	0.0445	L0-B	0.0243
L3	0.0189	L3	0.0213
R3	0.0088	L2	0.0142
		L1	0.0101
		R2	0.0068

3.5 Glow detection limits from archival data

MAHLI and MastCam showed the best sensitivities to observe triboelectric discharge. This result prompted further investigation of previous nighttime images with these two cameras to see if triboelectric glow or Phobos radiance had been captured by chance. The constraints with which the images were selected for analysis have been noted in Section 2.4. Tables 7

and 8 present the results from the analyzed images as well as image data such as LTST, L_s , exposure, and pointing to give context for these images. Images taken in the windy season are starred; saltation is a wind-blown process and saltation-induced triboelectric discharge is more likely to be observed in windy seasons. Based on the image's pointing, the associated region in view is listed. Based on the image's timestamp, the elevation of Phobos, if visible in the sky, is listed. Phobos is deemed visible if it has an elevation greater than 10° above the horizon (to account for the crater rim). To process this large dataset, the median pixel radiance value in each of the R,G,B filters is calculated. Since the dark noise of the cameras has already been subtracted in preprocessing, the pixel radiances signify extra radiance above the noise level of the cameras. Unusually high pixel radiances were then flagged for further investigation by producing colour maps and histograms of the image in question, which clarified whether the source of radiance was triboelectric discharge. The colour map showed the positions of the pixels on the x and y axes in terms of pixel number and the intensity of pixels by colour. The histogram displayed the radiance values of the pixels on the x axis and the number of pixels with each radiance value on the y-axis.

3.5.1 MastCam Results

For each MastCam image in Table 7, a mean pixel radiance in any filter under $1.0 \mu\text{W}/\text{m}^2/\text{Sr}$ was found to be negligible from an analysis of the colormap. The colormap of the image was filled with pixels of 0 radiance and dotted by a few higher radiance pixels in random positions. Since the higher radiance pixels did not have any pattern, were not limited to any region (sky/crater/ground) of the image, and were negligible in number, they were discounted as valid pixels. Images where the median pixel radiance exceeded this value have been highlighted in red.

The main sources of excess radiance are found in two series of images on sol 529 and sol 783. For the sequence on sol 529, the increase in radiance is attributed to light from behind the horizon, as shown in the colormap in Figure 13. The crater and foreground surface remains dark, suggesting that no saltation or glow is occurring. Phobos is not visible in

Table 7: Median Pixel Radiances of MastCam Nighttime Images

LTST	Exp. (s)	Temp. (°C)	[Az El]	LS	Median R	Median G	Median B	View	Phobos El.
sol-00529M 19:11:26	2	-20.97	[-71.7 17.9]	83.747	1.731	1.902	2.117	AS	NV
sol-00529M 19:11:45	2	-20.65	[-59.9 17.9]	83.747	1.998	2.365	2.325	AS	NV
sol-00529M 19:12:04	2	-20.65	[-47.9 17.9]	83.747	1.789	2.018	2.053	AS	NV
sol-00529M 19:12:22	2	-20.33	[-47.9 6.4]	83.747	2.568	3.072	2.987	H	NV
sol-00529M 19:12:41	2	-20.01	[-59.7 6.4]	83.747	2.764	3.334	3.342	H	NV
sol-00529M 19:12:59	2	-19.7	[-71.7 6.4]	83.748	2.649	3.210	3.204	H	NV
sol-00529M 19:13:39	2	-19.38	[-36.6 75.7]	83.748	0.725	0.829	0.827	AS	NV
sol-00529M 19:15:02	2	-19.06	[120.4 37.3]	83.748	0.693	0.798	0.791	AS	NV
sol-00783M 18:58:53	5	-20.01	[-54.6 5.9]	217.424*	17.459	17.522	17.082	H	43.7
sol-00783M 18:59:12	5	-19.7	[-54.9 18.9]	217.424*	24.676	26.414	27.613	AS	43.7
sol-00783M 18:59:30	5	-19.38	[-54.9 31.9]	217.424*	19.814	21.208	21.825	AS	43.7
sol-00783M 18:59:49	5	-19.06	[-54.8 44.9]	217.424*	14.386	15.244	15.552	AS	43.7

sol- 00783M 19:00:07	5	-18.74	[-54.9 57.9]	217.424*	10.774	11.309	11.327	AS	43.7
sol- 00783M 19:08:41	7.5	-19.06	[-45.9 54.1]	217.428*	4.503	4.745	4.771	AS	40.46
sol- 00783M 19:08:54	30	-19.06	[-45.9 54.1]	217.428*	4.23	4.396	4.487	AS	40.46
sol- 00783M 19:21:58	7.5	-18.74	[-50.2 51.8]	217.434*	1.359	1.465	1.398	AS	37.17
sol- 00783M 19:22:12	30	-18.74	[-50.2 51.8]	217.434*	1.232	1.257	1.292	AS	37.17
sol- 00783M 19:29:14	7.5	-17.15	[-52.0 50.8]	217.437*	0.815	0.865	0.849	AS	37.17
sol- 00783M 19:29:27	30	-17.47	[-52.0 50.8]	217.437*	0.696	0.698	0.720	AS	37.17
sol- 00783M 19:36:19	7.5	-17.47	[-53.6 49.7]	217.44*	0.531	0.567	0.569	AS	33.85
sol- 00783M 19:36:33	30	-17.78	[-53.6 49.7]	217.44*	0.414	0.406	0.433	AS	33.85
sol- 00783M 19:44:32	7.5	-17.47	[-55.7 48.2]	217.444*	0.381	0.407	0.419	AS	33.85
sol- 00783M 19:44:46	30	-17.78	[-55.7 48.2]	217.444*	0.264	0.247	0.285	AS	33.85
sol- 00783M 19:52:32	7.5	-17.78	[-57.2 47.1]	217.448*	0.318	0.341	0.361	AS	30.51
sol- 00783M 19:52:46	30	-17.78	[-57.2 47.1]	217.448*	0.188	0.169	0.212	AS	30.51

sol-00783M 19:59:21	7.5	-16.83	[-58.5 45.9]	217.451*	0.283	0.306	0.333	AS	30.51
sol-00783M 19:59:34	30	-17.15	[-58.5 45.9]	217.451*	0.165	0.142	0.194	AS	30.51
sol-00783M 20:07:17	7.5	-17.15	[-60.0 44.4]	217.454*	0.254	0.275	0.308	AS	27.14
sol-00783M 20:07:31	30	-17.15	[-60.0 44.4]	217.454*	0.145	0.121	0.176	AS	27.14
sol-00783M 20:15:07	7.5	-17.47	[-61.2 43.0]	217.457*	0.256	0.276	0.310	AS	27.14
sol-00783M 20:15:21	30	-17.78	[-61.2 43.0]	217.458*	0.130	0.108	0.160	AS	27.14
sol-00783M 20:26:15	7.5	-19.06	[-60.2 41.0]	217.462*	0.259	0.282	0.314	AS	23.77
sol-00783M 20:26:33	30	-18.74	[-60.2 41.0]	217.462*	0.141	0.116	0.176	AS	23.77
sol-00783M 20:29:24	0.5	-17.78	[-82.4 47.6]	217.464*	2.272	2.606	2.781	AS	23.77
sol-00783M 20:29:34	7.5	-17.78	[-82.4 47.6]	217.464*	0.146	0.124	0.182	AS	23.77
sol-00783M 20:29:48	30	-17.78	[-82.4 47.6]	217.464*	0.134	0.109	0.166	AS	23.77
sol-00783M 20:30:27	7.5	-17.15	[-75.2 40.4]	217.464*	0.161	0.135	0.203	AS	23.77
sol-02561M 02:19:59	10	-25.1	[166.6 -35.8]	95.329	0.212	0.181	0.266	AG	NV
sol-02561M 02:20:14	10	-24.78	[166.6 -35.8]	95.329	0.214	0.181	0.269	AG	NV

sol- 02561M 02:20:29	10	-24.47	[166.6 -35.8]	95.329	0.215	0.181	0.270	AG	NV
sol- 02561M 02:20:43	30	-24.47	[166.6 -35.8]	95.329	0.193	0.143	0.242	AG	NV
sol- 02561M 02:21:18	30	-24.15	[166.6 -35.8]	95.329	0.188	0.139	0.236	AG	NV
sol- 02561M 02:21:55	30	-23.83	[5.7 - 59.7]	95.329	0.192	0.142	0.242	AG	NV
sol- 02561M 02:22:31	60	-23.51	[5.7 - 59.7]	95.33	0.205	0.148	0.258	AG	NV
sol- 02561M 02:23:36	60	-22.56	[5.7 - 59.7]	95.33	0.223	0.161	0.280	AG	NV
sol- 02561M 02:24:45	60	-21.92	[5.7 - 59.7]	95.33	0.216	0.155	0.271	AG	NV
sol- 02561M 02:25:50	120	-21.92	[5.7 - 59.7]	95.331	0.229	0.165	0.288	AG	NV
sol- 02561M 02:27:56	120	-21.29	[166.6 -35.8]	95.331	0.233	0.168	0.293	AG	NV
sol- 02561M 02:30:03	120	-20.65	[166.6 -35.8]	95.332	0.239	0.172	0.300	AG	NV
sol- 02561M 02:33:22	0.5	-20.01	[166.6 -35.8]	95.333	1.309	1.186	1.616	AG	NV
sol- 02561M 02:33:40	10	-20.33	[166.6 -35.8]	95.333	0.251	0.192	0.314	AG	NV

bold: unusually high values

*denotes windy season

AS: Image view is All Sky

AG: Image view is All Ground

NV: Not Visible

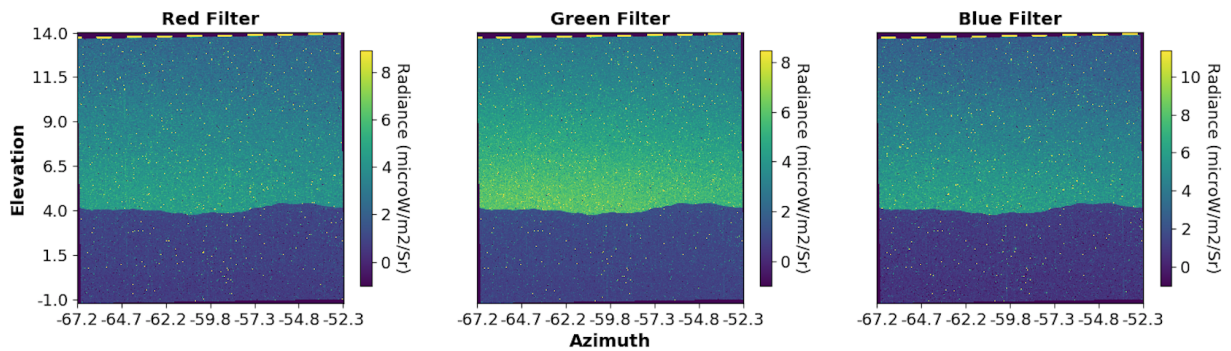


Figure 13: Colourmap of MastCam image taken on sol 529 showing the variation of individual pixel radiance in the image. R,G,B filters shown separately. Axes show azimuth and elevation of image.

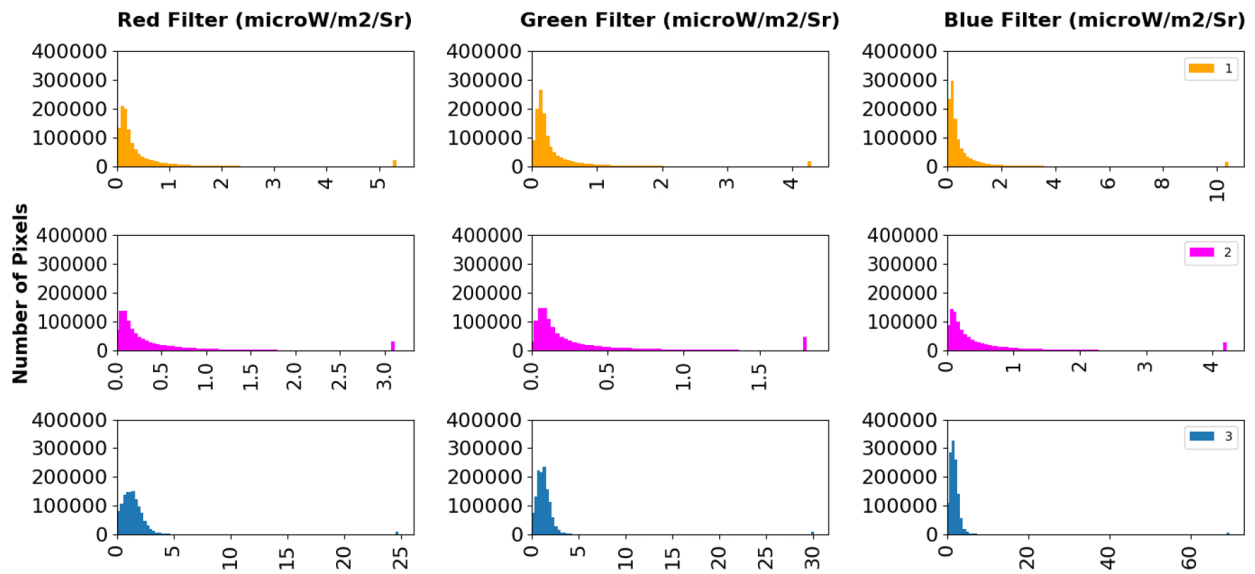


Figure 14: Histogram of pixel values of three MastCam L0 images 1: 2561ML0121520010805736C00_DXXX.IMG, 2: 2561ML0121520020805737C00_DXXX.IMG, 3: 2561ML0121520030805738C00_DXXX.IMG. X-axis shows the radiance value of the pixel and y-axis shows the number of pixels with this radiance value.

the sky and sunset in LTST on sol 529 occurred at 17:51. This image was taken at 19:12 LTST, which is 80 minutes past sunset, making twilight glow an unlikely possibility. The source of radiance is likely due to diffuse illumination of the night sky that has produced an isotropic scattering effect, which increases with airmass. The light is most concentrated behind the crater rim, supporting this idea, and all three horizon images show this same pattern of illumination. The sequence on sol 783 is not pointed to the ground and is therefore irrelevant to both triboelectric discharge and Phobos shine. Other than these images on sol 783, despite Phobos being visible in the sky, no extra radiance is noted by MastCam L0 on this sol. However, the camera is pointed at 40-48°, intended to capture the Siding Spring Comet and Phobos lowers to 23° of elevation, or below the camera, as time goes on. On sol 2561, there is no extra radiance to be noted. Even though the camera is pointed almost directly to the ground, this data was not taken during the windy season and Phobos is not visible in the sky. As such, there are no light sources expected to be captured by the camera. The three histograms shown in Figure 14 sample images on sol 2561: the histogram peaks near zero radiance and depreciates too quickly to be of note.

3.5.2 MAHLI results

Table 8 summarizes the data found in MAHLI nighttime images. The median radiance values of all images were zero, so the maximum radiances have been listed instead, as a limiting case. The median values suggest that no extra radiance was captured by the detector. However, the camera is pointed very closely at a surface target in almost all cases, due to the nature of how MAHLI is used in the mission. The first four images taken on sol 165, are pointed at Mount Sharp during the night and are taken in the windy season between 18:00-21:00 LTST, fulfilling two of the criteria for the observation. This is rare since MAHLI has not targeted Mount Sharp or any other non-surface target at night to date. Unfortunately, no extra radiance is observed, even if these images are stacked together. Phobos is not visible in the sky to be captured by the detector. Thus, it is not possible to confirm whether Phobos radiance could have been captured by the camera. In another instance, on sol 1337, Phobos

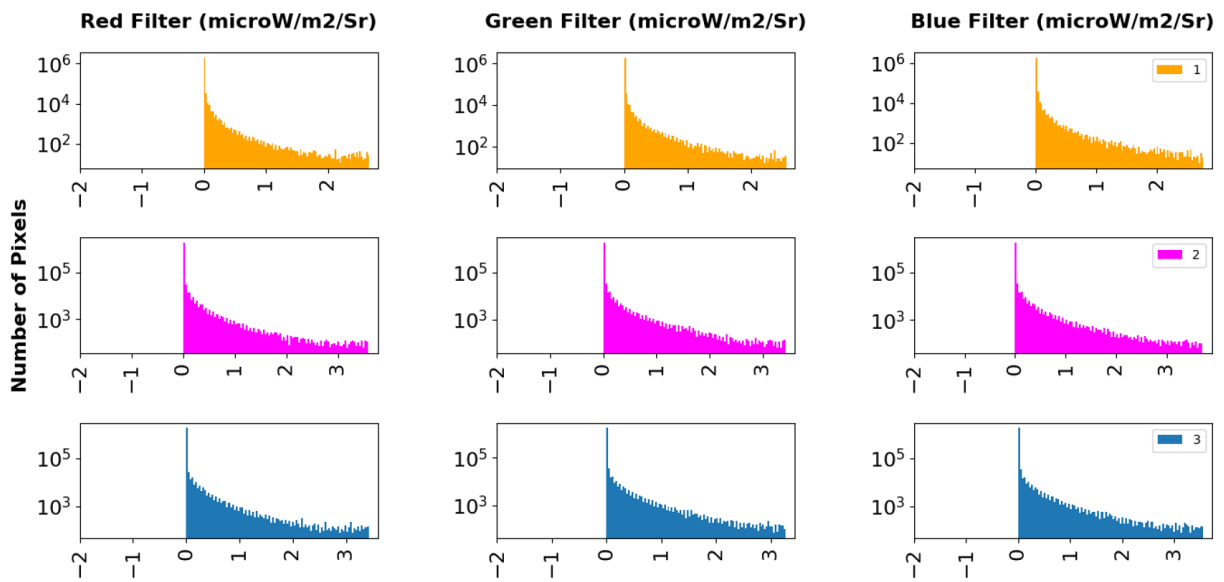


Figure 15: Histogram of pixel radiance values of three MAHLI images in Red, Green, and Blue filters 1: 0165MH0001990000101970C00_DRXX.IMG, 2: 1337MH0006090060601419C00_DRXX.IMG, 3: 2018MH0007390070800977C00_DRXX.IMG. X-axis shows the radiance value of the pixel and y-axis shows the number of pixels with this radiance value.

is visible in the sky at an elevation of 35-38°. The light from Phobos could have possibly reflected off the surface features that MAHLI is pointed at. However, again with a zero RGB median, this possibility is nullified. It is also possible that the specific rock being targeted was simply not subject to the reach of Phobos shine.

The colour maps and histograms of the images in Table 8 were analyzed to confirm that there were no patterns of radiance that could be attributed to triboelectric discharge. The histograms of the images with the three highest maximum radiances are illustrated in Figure 15 as an example of this. From this figure, it is clear that the only pixel value of significance is zero.

3.6 Upper Limit of Glow

The analysis of past nighttime images taken by MastCam and MAHLI are unable to define upper limits to the magnitude of glow discharge. None of the images fulfil both criteria needed to define upper limits of the glow: imaged during the windy season and image pointed at horizon with substantive foreground. The four images taken by MAHLI of Mt. Sharp do fulfil both criteria, however, the total duration of this sequence is less than 5 minutes, which is not enough time to ensure saltation activity definitively occurred. To define upper limits for glow discharge, a specific observation must be designed. The observation parameters themselves are easy to execute for the rover and have been used several times before. It would require the rover/lander to take a nighttime long-exposure image prepointed during the day to face the possible saltation activity from winds moving down dunes or tall features. The optimal time of year and day to conduct the observation has been discussed in Section 2. Image maps (like Figure 13 produced from the data will make it easier to discern triboelectric discharge from other sources of light, as the discharge should only occur below the horizon, where the sand particles lie. Previous nighttime image analysis shows that the ground is not lit up by remnant sunlight and is not sensitive enough to be lit up by starlight or other optical effects, thus the contrast of the dark ground allows for identification of the discharge.

Table 8: Median radiance value of MAHLI nighttime images.

sol	Exp. (s)	Temp. (°C)	Az., El.	LTST	LS	Max R	Max G	Max B	View	Phobos El.
165	30	-22.88	130.33, 14.56	20:39:34	250.16*	2.67	2.552	2.76	MS	NV
165	60	-22.88	130.33, 14.56	20:40:11	250.16*	1.335	1.276	1.38	MS	NV
165	120	-22.88	130.33, 14.56	20:41:17	250.16*	0.667	0.638	0.69	MS	NV
165	270	-21.92	130.33, 14.56	20:43:20	250.16*	0.297	0.284	0.307	MS	NV
165	15	-21.6	254.5, -73.94	20:58:28	250.17*	5.724	5.471	5.915	Rock	NV
165	30	-21.6	254.5, -73.94	20:59:25	250.17*	2.862	2.735	2.958	Rock	NV
165	60	-22.24	254.5, -73.94	21:01:06	250.17*	1.431	1.368	1.478	Rock	NV
165	120	-22.88	254.5, -73.94	21:04:15	250.17*	0.715	0.684	0.739	Rock	NV
165	270	-22.56	254.5, -73.94	21:10:48	250.17*	0.318	0.304	0.329	Rock	NV
165	15	-21.6	254.51, -73.95	21:24:17	250.18*	6.186	5.912	6.393	Rock	NV
165	30	-22.24	254.51, -73.95	21:25:15	250.18*	3.093	2.956	3.197	Rock	NV
165	60	-22.56	254.51, -73.95	21:26:56	250.18*	1.546	1.478	1.598	Rock	NV
165	120	-21.6	254.51, -73.95	21:30:05	250.18*	0.773	0.739	0.799	Rock	NV
165	270	-21.92	254.51, -73.95	21:36:38	250.19*	0.344	0.328	0.355	Rock	NV
1337	30	-21.29	31.38, -86.39	21:22:44	150.72	3.537	3.381	3.656	Rock	35.26
1337	60	-22.24	31.38, -86.39	21:24:25	150.72	1.768	1.69	1.828	Rock	35.26
1337	30	-21.29	31.71, -86.37	21:32:40	150.73	3.797	3.63	3.925	Rock	35.26
1337	60	-21.6	31.71, -86.37	21:34:21	150.73	1.898	1.814	1.962	Rock	35.26

1337	30	-21.6	49.98, -87.75	21:43:44	150.73	3.591	3.433	3.712	Rock	38.69
1337	60	-21.92	49.98, -87.75	21:45:25	150.73	1.795	1.716	1.856	Rock	38.69
1337	120	-21.92	49.98, -87.75	21:48:34	150.73	0.898	0.858	0.928	Rock	38.69
2018	30	-21.92	207.86, -78.27	20:02:14	157.32	3.425	3.274	3.54	Rock	NV
2018	60	-22.56	207.86, -78.27	20:03:55	157.32	1.713	1.637	1.77	Rock	NV

Note: All MAHLI median RGB values were 0

*denotes windy season

MS: Mount Sharp

NV: Not Visible

Max R, G, B values are in $\mu\text{W}/\text{m}^2/\text{Sr}$

4 Evaluating trace gas emission cycles at Gale

Ultimately, this thesis aims to understand if there is evidence of triboelectric discharge altering gas-surface chemistry at Gale and if so, how prominent its effects are. Since it seems unlikely that Curiosity’s cameras will successfully detect triboelectric discharge directly, it is necessary to extract the presence of triboelectric discharge on gas-surface chemistry indirectly.

4.1 Periodicity

The variation of saltation at Gale Crater has been discussed in depth in Section 2. SAM-TLS (Tunable Laser Spectrometer) detects a background level of methane in the crater, which appears to vary seasonally as well (Webster et al., 2018). TLS has a wavelength of 2.78 μm , which is already highly sensitive to methane when the gas is directly ingested into the chamber; in the case of background measurements, the gas is ingested and passed over a CO_2 scrubber to achieve an enrichment factor of 25 and reduce uncertainty (Webster et al., 2018). Measurements are started around midnight LTST; direct ingests take 7 minutes whereas enrichment measurements ingest gas over a two hour period. Enrichment measurements

were first initiated due to the debate surrounding the magnitude of methane found on Mars as a way to gain high precision measurements. However, the results found methane in two different orders of magnitude: > 1 ppbv and < 1 ppbv, the latter of which was named background measurements.

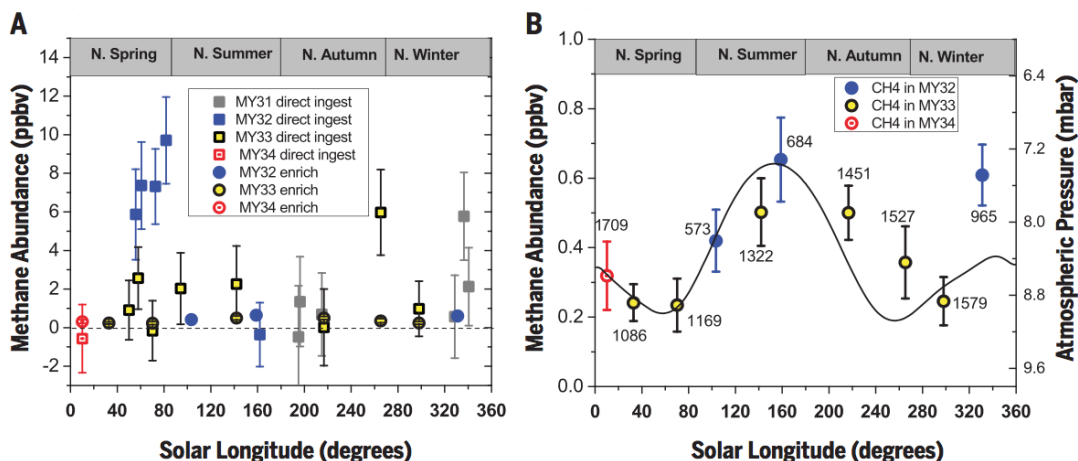


Figure 16: Taken from Figure 1, Webster et al. (2018). All plotted values have error bars of ± 1 SEM, and are corrected to global mean annual values. (A) All measurements up to 27 May 2017, including those from direct ingestions (squares) and enrichment ingestions (circles with smaller error bars). (B) Background measurements from enrichment ingestions. The atmospheric pressure (inverted scale at right) from REMS is plotted for comparison, the solid line representing the mean values over the 3 Mars years.

Temporal methane variation is not local to Gale Crater; previous MEx-PFS measurements have found not only spatial variations of methane, but also seasonal variations, with a global rise of methane in northern summer and global depletion in northern winter (Fonti and Marzo, 2010; Geminale et al., 2011). If triboelectric discharge is the cause of the seasonal variation of background methane at Gale crater, it is important to establish that this methane variation is in fact annual. If the methane variation is found to be annual, periods of maximum triboelectric discharge can be studied with respect to methane seasonality to assess if a correlation exists. Methane variation in the crater is sampled very sparsely using

SAM-TLS; as such a high resolution analysis is not possible at this time. The data over 3 Martian years shows a persistent, though small, background level of methane, which has at least one strong peak at L_s 160° , as in Figure 16. The pressure data overlaid on the background methane measurements serves as a reference to a well-known seasonal variation in the Mars atmosphere.

The existence of a robust variation in the methane has been claimed by Webster et al. (2018) and debated by Gillen et al. (2020). With three new measurements in 2020, the statistical significance of a seasonal cycle can be reassessed.

4.2 Statistical Analysis of Annual Methane Variation

Gillen et al. (2020) employ Gaussian Process regression via the *exoplanet* (Foreman-Mackey and Barentsen, 2019) and *celerite* (Foreman-Mackey, 2018; Foreman-Mackey et al., 2017) python libraries. An annual variation of methane was not favoured by this approach (Gillen et al., 2020); the highest probability periods were less than 100 sols if the entire SAM-TLS dataset is analyzed. If only the enriched background data are considered, plausible periods extended to 600 sols, with the median period at 498 sols. Gillen et al. (2020) present 200 outcomes of the GP algorithm in Figure 1 of their paper (Figure 17 in this thesis). Although some outcomes remain cyclical, a significant number of outcomes are straight lines or highly oscillating waves, ignorant of the Martian year. Figure 2 of their paper shows the probability density of periodic models of enriched background data (Figure 18 in this thesis). By Gillen et al. (2020)s analysis, the probability density of a one-Martian-year period is not the peak of the curve, and thus not the most likely possibility. In addition, the entire curve falls under a density of 0.002 on a scale of up to 1, signifying that the probability of any period at all is extremely low.

The issue with this approach is manifold. The effort to remove scientific bias towards periodicity is appreciated, however, the non-periodic assumption likely under-constrains the dataset. The values in the dataset do not represent something arbitrary such as the number of toys produced per day. The dataset consists of gas concentrations in an atmosphere,

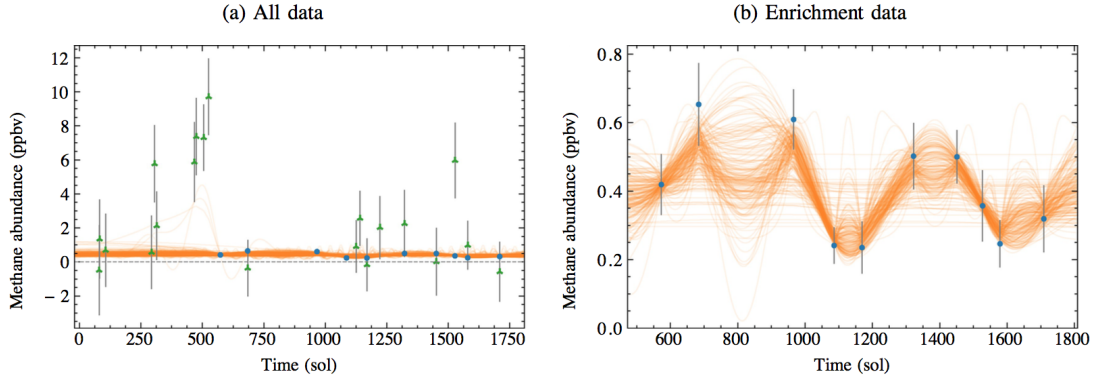


Figure 17: Taken from Figure 1, Gillen et al. (2020). Methane surface concentration [ppbv] vs. time [sol], using all data (a) and only the enrichment data (b), from (Webster et al., 2018), where error bars are 1 standard error. Green triangles represent direct data and blue circles the enriched data. The methane estimates are fit using GP regression, where the orange lines represent 200 individual models drawn from the GP posterior distribution.

which are inherently dependent on pressure and temperature. Pressure and temperature have unquestionable seasonality in a planetary atmosphere due to the tilt of Mars upon its axis and its orbit around the sun. Thus, to deny the seasonality behind the parameters that contribute to these values may be incorrect. The magnitude of background methane is small and almost at the edge of detection of SAM-TLS. The variation in the dataset is small as well, < 0.5 ppbv. As such, it is easy to fit the data points to a straight line, especially given the sparseness of the data. However, a small change does not always imply an insignificant change, but may instead imply a delicate process.

To assess the effect of the additional methane measurements reported on a statistical assessment of likely periods, a new periodicity analysis was conducted using a well-known, robust technique known as the Lomb-Scargle method. Gillen et al. (2020) stated that their Lomb-Scargle periodogram produced similar results to their GP model; it was thus found to be a favourable technique to confer with their previous work. However, it must be noted that it is only possible to compare the Lomb-Scargle results to the subset of results that

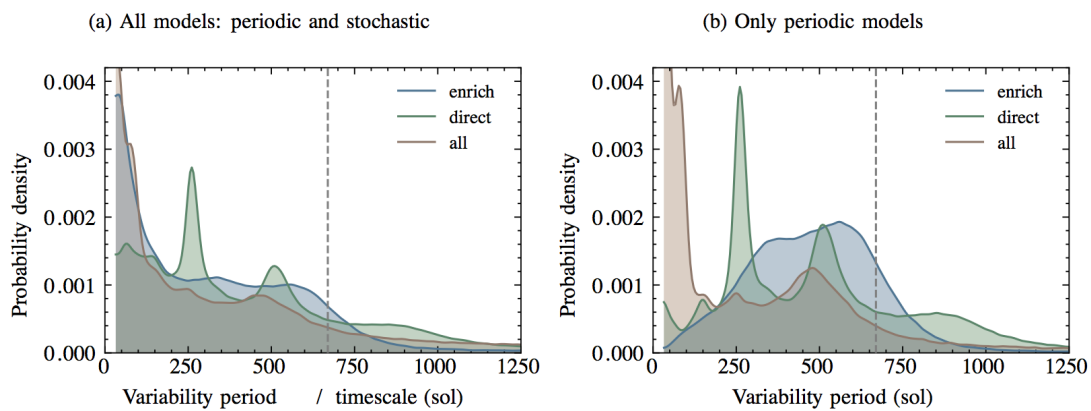


Figure 18: Taken from Figure 2, Gillen et al. (2020). Posterior period distributions from the GP model. Higher probability density corresponds to a more strongly favored period for methane variability. Three posteriors are shown: using all the data (red), only the direct data (green), and only the enriched data (blue). Panel a shows the results when including all GP models and panel b shows the posterior period distribution when selecting only those models which we classify as periodic. The vertical dashed grey line indicates the variability period expected if there were seasonal variation of methane on the Martian surface.

were periodic models, as the Lomb-Scargle algorithm assumes periodicity.

4.3 Assessment of Periodicity with Lomb-Scargle Periodogram

The Lomb-Scargle algorithm employs both Fourier analysis and the Least Squares method, can be derived from Bayesian probabilities, and makes no apriori assumptions about period length. The Lomb Scargle method is particularly effective for unevenly sampled time series data (VanderPlas, 2018) and is only successful if the data has uncorrelated white noise; both these characteristics describe the SAM-TLS enriched methane dataset. The Lomb-Scargle periodograms (LSP) presented in this section were constructed using the *astropy* python library (VanderPlas et al., 2012) (VanderPlas and Ivezić, 2015). The sol and time of observation were taken as 1 hour after the ingest began for each methane measurement, the methane concentrations used were corrected for atmospheric pressure and the associated uncertainties on each measurement were taken as the reported standard error. Additional parameters were selected based on literature recommendations (VanderPlas, 2018): the number of samples per peak was set at 5. To compare the LSP to the periodic models (Gillen et al., 2020), the LSP power was converted to probability by:

$$P(GP) \propto e^{LS} \tag{17}$$

where $P(GP)$ is the probability from the GP Bayesian Model and LS is the Lomb-Scargle Power. In practice, when equation (17) is applied to the Lomb-Scargle power values, it results in probabilities from a minimum value of 1 to an upper limit of e , as Lomb-Scargle powers range from 0 to 1. To converge these values into a meaningful probability, the exponent transformed LS powers are subtracted by the minimum value (unity) and normalized. The transformed Lomb-Scargle curve of the enriched background (Webster et al., 2018) datapoints (W18) in Figure 19 shows a clear correlation to the probability density of enriched, periodic models (Gillen et al., 2020), whose curve has also been scaled, such that the shapes can be compared rather than the magnitudes of the probabilities themselves.

Figure 20 shows the LSP constructed from the W18 data and additional enriched dat-

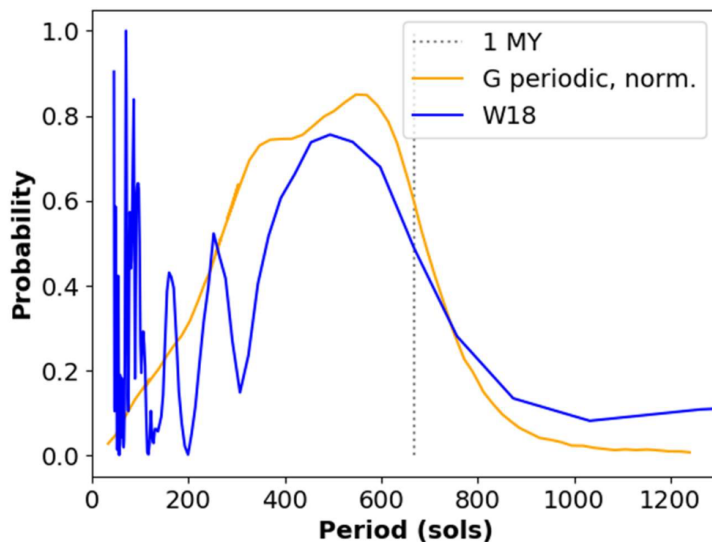


Figure 19: A comparison between the probability curve of the LSP generated from the W18 data (blue) and the scaled posterior period probability distribution from GP analyses of W18 data (Gillen et al., 2020, orange). Grey dotted line represents 1 Mars Year.

apoints, excluding the 20.8 ppbv plume detection (W20). The maximum period has been limited to 1300 sols as periods longer than the timeframe of the data are statistically meaningless (VanderPlas, 2018). Aside from very short periods, the W18 data’s LSP has a high-powered peak at 503 sols, similar to the peak observed by Gillen et al. (2020). The LSP created from the extended W20 data, however, has two high-powered peaks, one of which peaks at 626 sols, or within 6.3% of a Mars Year (668 sols). The concept of power on an LSP is analogous to probability for the purposes of this analysis, except that the terminology is derived from the Fourier series power spectrum.

The significance of the Lomb-Scargle peaks can be assessed using their false alarm probability (FAL): the probability that a periodogram made from data without a signal could produce a peak of comparable magnitude from random Gaussian noise (VanderPlas, 2018). In this case, the Baluev method was used for the probability approximation, as implemented in *astropy*, to provide an upper limit on the FAL (Baluev, 2008). In Figure 20, the FAL for

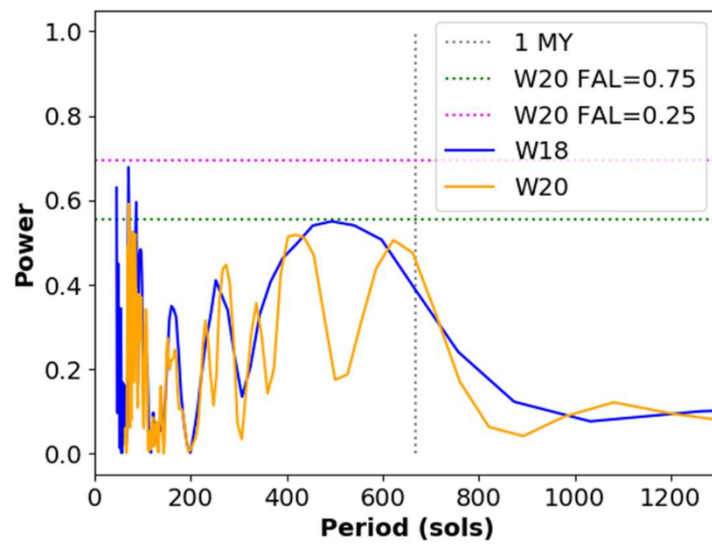


Figure 20: Comparison of LSP generated from W18 and W20. X-axis shows possible periods. Y-axis shows power of those periods. Grey dotted line represents 1 Mars Year. Green dotted line is the power needed to achieve a false alarm level of 0.75. Pink dotted line is the power needed to achieve a false alarm level of 0.25.

the peak at 503 sols in the W18 dataset is 0.965, and that of the peak at 626 sols in the W20 dataset is 0.894; thus, both could have been formed through random noise alignment. In addition, since the FALs are computed solely based on the power value, all peaks of similar power and lower can potentially be discounted. In Figure 20, the green dotted line shows the power a W20 dataset peak needs to achieve a false alarm level of 0.75 or below. Almost none of the peaks in the W20 dataset achieve this level and none of them achieve a false alarm level as low as 0.25, at which the peak is unlikely to be noise generated.

However, the measurement at 965 sols has been discussed as a likely anomaly (Moore et al., 2019). The results change significantly when the measurement at 965 sols is removed as demonstrated in Figure 21. The removal of the sol 965 measurement alters both LSPs (Figure 21a) to peak almost exactly at one Martian year. The FAL of the W18 dataset peak at 667 sols is 0.526 - too large to qualify as a significant peak, in agreement with previous findings (Gillen et al., 2020). The FAL of the 2020 dataset peak at 662.6 sols, however, is 0.051, indicating that a peak of this magnitude is unlikely to have been generated from a non-periodic dataset. An annual variation of background methane on Mars is now a distinct and likely possibility.

The LSP is highly sensitive to the sampling of the data. When the algorithm is applied to a sine curve without noise, sampled at regular intervals (Figure 21b, 'PS'), the LSP produced one peak at the expected period. A sine curve without noise sampled at SAM intervals (Figure 21b, 'SS'), however, produced peaks at various points: < 200 sols, 260 sols, and 390 sols. These peaks are slightly shifted and exaggerated in the LSP of a sine curve with noise (Figure 21c, 'NS'), also sampled at SAM intervals and given a period of 668 sols (1 Martian year). Additional peaks present on the LSPs of simulated data are therefore a feature of the data sampling and are not meaningful. This implies that the additional peaks seen in the LSP of W20 data could simply be a result of the sampling as well, especially the set of crowded peaks at < 200 sols, which are suggested by all three plots in Figure 21. As a result, many of the short period candidates for methane variation are potentially eliminated.

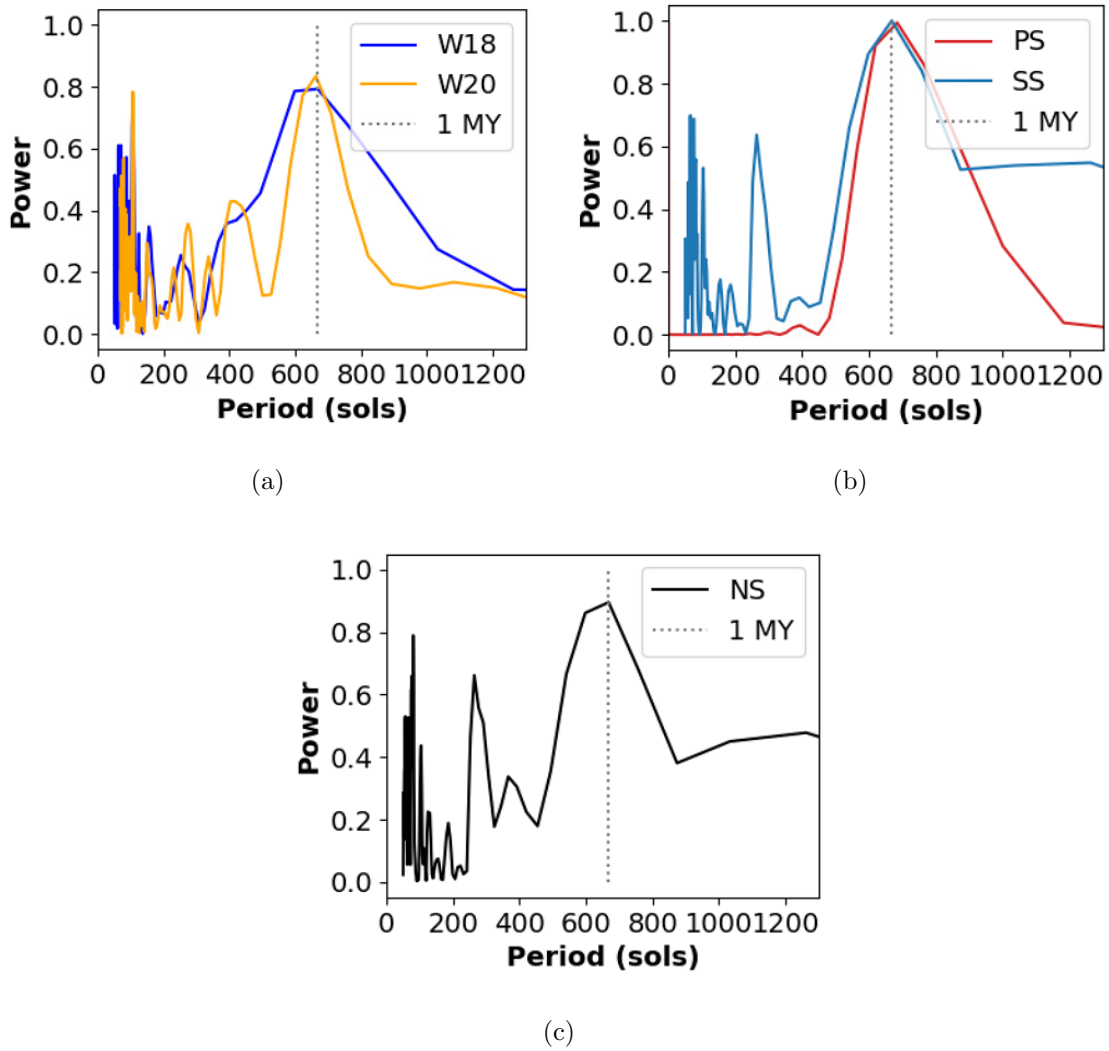


Figure 21: In all cases, x-axis shows possible periods. Y-axis shows power of those periods. Dotted grey line represents 1 Mars Year (MY). (a) LSP generated from W18 and W20 with 965 sol measurement removed. (b) LSP generated from sine curve regularly sampled (PS) and sine curve sampled at SAM intervals (SS). (c) LSP generated from sine curve sampled at SAM intervals with added noise of a normal distribution centred around the mean of the methane quantity error of W18 (NS).

4.4 Atmospheric Cycles

Employing the Lomb-Scargle method on well-behaved datasets such as Ar , N_2 , and the dust cycle obtained from Section 2 helps to cross-reference the validity of the technique. The Argon and Nitrogen LSPs have peaks located at 143.6, 331.5, and 675.2 sols, as displayed in Figure 22. Observations of nitrogen and oxygen were taken in conjunction by SAM, therefore, the datasets are sampled identically. This explains why both diagrams have identical shorter-period peaks despite differences in data values and error margins, and further demonstrates that sampling is the reason for shorter periods appearing on the Lomb-Scargle diagram. Table 9 provides characterization of the datasets of the atmospheric gases involved in this work. All datasets listed except for the dust dataset are extremely sparse with less than 20 points in almost three martian years. In spite of this, each dataset has an LSP peak near 1 mars year, and the distance of that peak from 1 mars year is less than the error percentage of each dataset. This is notable because the nitrogen and oxygen datasets have small error margins.

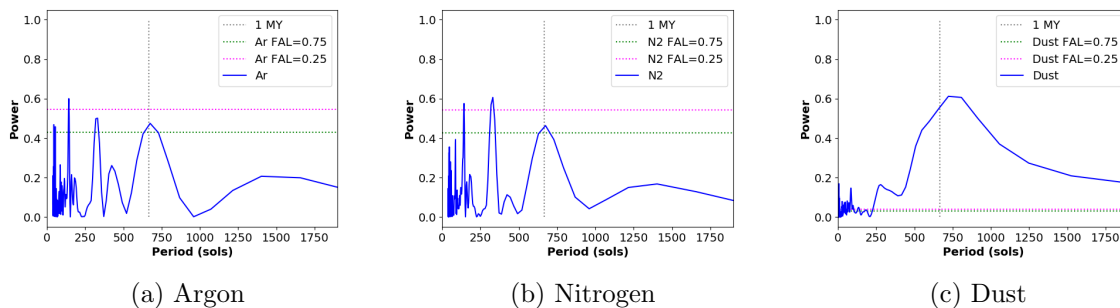


Figure 22: LSP of Atmospheric Argon, Nitrogen, and dust at Gale. X axis shows possible periods. Y axis shows power of those periods. Dotted grey line represents 1 Mars Year. FAL is the false alarm probability level.

The dust dataset shows only one LSP peak of note at 698.4 sols. The effect of a less sparse dataset can be noted here, in that it suppresses invalid short period peaks from the Lomb-Scargle diagram efficiently. In addition, despite the significant error in the dataset, its

Table 9: Error Margin in Atmospheric Cycles

Atmospheric Component	Span of dataset (sols)	Length of dataset	Error % in dataset	Peak	Peak Error %
Argon	1824	19	2.0	675.2	1.08
Nitrogen	1824	19	3.2	675.2	1.08
Methane	2054	12	25.1	662.6	0.81
Dust	1400	236	21.0	698.4	4.55
Oxygen	1824	19	18.0	628.7	5.88

*Error % in dataset column values for Argon, Nitrogen, and Oxygen taken from Trainer et al. (2019)

peak is within 4.55% of 1 Mars year or one-third the error margin. The breadth of the peak, however, can be attributed to the large error involved in the dust dataset. Furthermore, the Lomb-Scargle method is able to successfully retrieve a cycle in oxygen, the other gas involved in the methane destruction mechanism, where large irregularities exist. Figure 23 gives an annual cycle for Oxygen a confidence interval well below the false alarm probability of 0.25. The oxygen peak near one mars year is also one third of the error margin. There is one new feature to the oxygen LSP: it has a significant peak longer than 1 martian year. Since the Lomb-Scargle method assumes periodicity, unrealistically long periods and near-zero periods indicate the probability of no periodicity. Though these may be valid results, the same argument applied to methane is applicable here. Oxygen values are an order of magnitude smaller than nitrogen and oxygen and vary less than 0.001 in magnitude, which makes non-periodicity easy to conclude. In contrast, the probability of five atmospheric components converging to a variability of one martian year is harder to ignore.

It is now possible to assemble a diagram with the oxygen, saltation and methane cycles on Mars. In each case, the Lomb Scargle method takes the strongest period, as in Table 9, and fits the y values based on model parameters. The inconsistency in phase seen in Figure

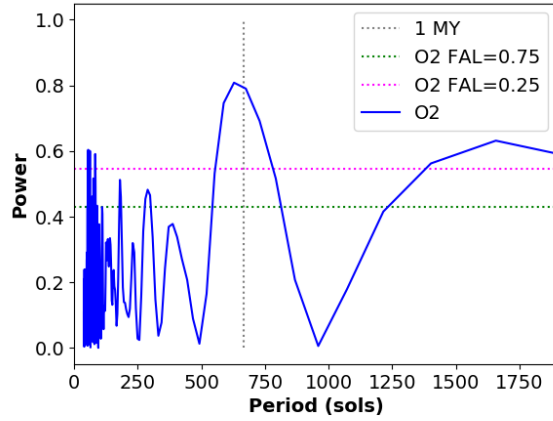


Figure 23: LSP of Atmospheric Oxygen at Gale. X axis shows possible periods. Y axis shows power of those periods. Dotted grey line represents 1 Mars Year (MY). FAL is the false alarm probability level.

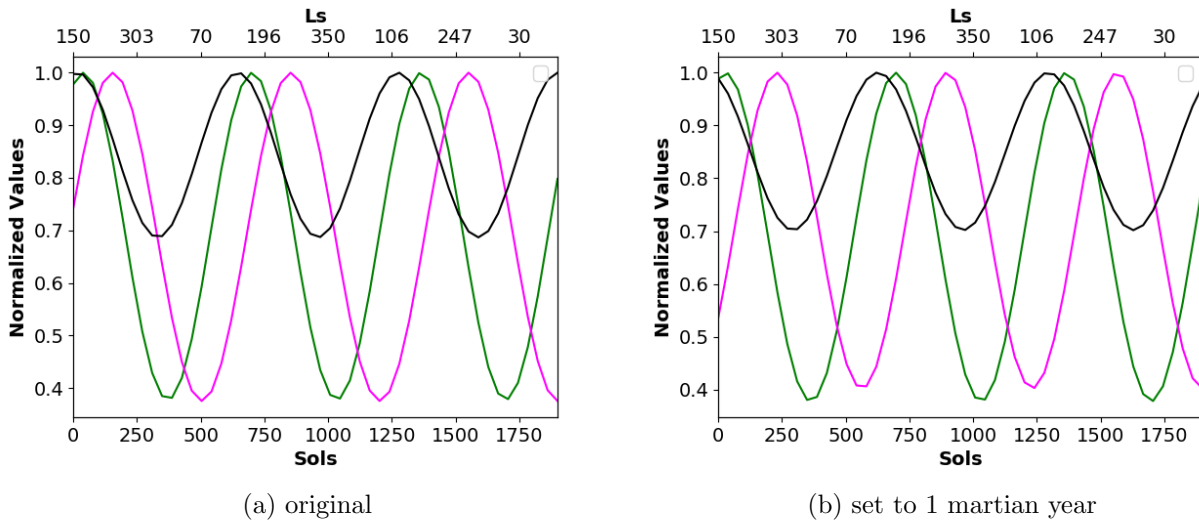


Figure 24: Methane destruction cycle at Gale with (a) periods equal to highest power on respective LSP and (b) periods set to one mars year for all cycles. X axis shows time progression with sol and L_s . Cycle datapoints are normalized to unity on y-axis. Cycles displayed are dust (pink), methane (green), and oxygen (black).

24a is a result of this. The length of the x-axis was chosen arbitrarily, such that multiple cycles could be displayed. For comparison, if the periods of all three cycles are set to 1 mars year exactly, the results are as in Figure 24b. However, the pattern can be seen plainly in both. A rise in dust concentration and thus saltation activity is followed, after a short phase lag (67.5°), by a decrease in oxygen and methane. This is evidence that sand electrification is the beginning of the process, and that a period of time is needed for sand electrification to ionize gases, chemical reactions to occur, and oxidants to form and accumulate in the soil. Oxidants do not accumulate immediately, and until then the oxygen levels are not shown to decrease. The decrease in oxygen represents the start of the accumulation of oxidants. The original cycles make the phase lag between the oxygen and methane hard to decipher, however, in the adjusted cycles it can be seen clearly. The oxygen decreases first, and the methane decrease is followed by a small phase lag, which would be expected since oxidation of methane should begin soon after the accumulation of oxidants. The precision of Figure 24b in matching the predicted chemical reactions is unexpectedly high, given the sparseness of the datasets as well as the limited experimental data available. The subsequent fall in dust concentration or saltation activity allows the methane and oxygen to regain concentration in the atmosphere. The cycle amplitudes for methane and dust are similar whereas the variation of oxygen is less than half of the other two cycles. This does not imply a lack of oxygen to supply oxidation reactions. Methane mixing ratios are on the order of ppb and oxygen mixing ratios are on the order of ppm, thus there exists a larger absolute amount of oxygen, which is why it may be depleted less as a fraction of the total amount compared to methane.

4.5 Methane Destruction Rate Calculations

Triboelectric discharge could explain the disappearance of methane on either or both of these timescales: the occasional smaller plume at Gale crater, which is inhibited from reaching orbiters the next day and the rare high volume plume that spreads globally. Lab simulations strongly suggest that triboelectric discharge is able to act quickly. It is necessary to test

if it can scavenge methane as quickly as the two types of plumes require. The following calculations are extremely low accuracy and simplistic. To start with, the amount of H_2O_2 produced by saltation was 44.9 nmol/g as noted above. The surface area of the tube was stated as 3.4 m²/g by Bak et al. (2017). If we divide the first by the second we get a quantity of 13.21 nmol H_2O_2 /m² JSC-1, which is easier to work with. This amount of H_2O_2 was created in 63 days or 5443200 s of tumbling (Bak et al., 2017), which is equivalent to 2.43×10^{-6} nmol/m²/s of H_2O_2 .

The large plume simulated by Viscardy et al. (2016) released 5×10^6 kg of methane into the atmosphere. Here, it is also assumed that triboelectric discharge is only effective when the plume is caught inside the PBL. This is because the compression of the PBL to approximately 16 m each night allows saltating particles access to a significantly higher number of gas molecules, and gas molecules outside the PBL are not subject to this type of compression (Moores et al., 2019). The methane modelled by Viscardy et al. (2016) does not surpass the height of the PBL (10 km) for 5 sols. However, there are no limits on horizontal dispersal. The dispersal of methane horizontally after 5 sols can be seen in Figure 1a, Viscardy et al. (2016) and is reproduced in Figure 25 with area vertices projected on to it. Thus, the area exposed to saltation is approximately the sum of the area of the trapezoid and circle enclosed. In latitudinal/longitudinal coordinates the area is 4235.4. The total area of a map is the area of the rectangle in latitudinal/longitudinal coordinates or $360 \times 180 = 64800$. The fraction of the Mars surface exposed to saltation is then 0.065. The surface of Mars has an area of 144.8×10^{12} m². The area exposure to saltation in real units is 9.46×10^{12} m². However, saltation occurs where sand-sized particles reside and sand dunes cover $\ll 1\%$ of the surface of Mars (Hayward et al., 2007). If we take the upper limit of sand dune coverage to be 1%, the area exposure reduces to 9.46×10^{10} m²

This means 2.295×10^{-4} mol/s of H_2O_2 could be produced if saltation occurred everywhere on the surface under the plume simultaneously. The required ratio of H_2O_2 molecules to CH_4 molecules for the oxidation of methane by triboelectric discharge is 1:1, as seen by this chemically balanced equation: $CH_4 + H_2O_2 = CH_3OH + H_2O$ (Qian et al., 2018). Thus

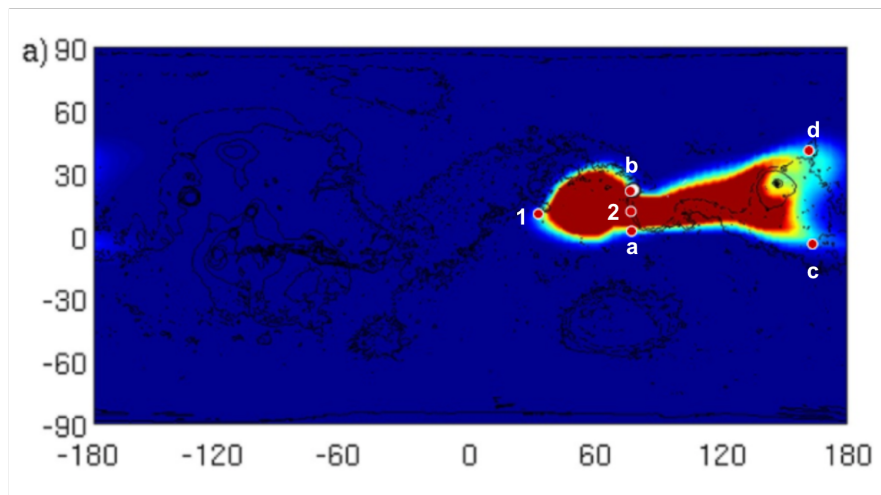


Figure 25: Taken from Figure 1, Viscardy et al. (2016). Horizontal distribution of the column-averaged mixing ratio of methane (in ppb) for 5 sols after an instantaneous surface release of methane in Nili Fossae (indicated by a white dot) at L_s 150°. Area vertices projected on to map. 1 and 2 represent diameter of circle. a,b,c,d represent corners of trapezoid.

the number of H_2O_2 particles created by triboelectric discharge is equivalent to the number of methane particles destroyed. This is a gross oversimplification as chemical reactions never yield 100%. Previously methane oxidation tests done with H_2O and O_2 in Earth atmospheric conditions showed a yield of 32% (Indarto, 2016). Since H_2O_2 is a stronger oxidant and Mars pressure is much lower, we assume the yield to be 50%. Such a yield would result in 1.148×10^{-4} mol/s of methane. Multiplying by the molar mass of CH_4 (16.04 g/mol), triboelectric discharge would eliminate 1.84×10^{-3} g of methane every second. If we divide the total methane release by this rate of elimination, and assume that such a rate of elimination continues as the methane disperses even further across the surface, it would take 86136 years to completely eliminate the methane. However, this is only one oxidant, the more powerful perchlorates are not included and there are several factors that are extremely hard to estimate. Furthermore, the rate of H_2O_2 production is based on simulating saltation as tumbling sand inside a tube, which has limited applicability to the particle interactions in a planetary surface. The methane model is also heavily reliant on atmospheric models of Mars, which are incomplete, as noted in Section 2.

It is perhaps more reasonable to ask if a SAM plume inside the crater could be eliminated in time. The diameter of Gale Crater is 154 km, giving it an area of 1.86×10^{10} m², assuming it is circular. If 1% of the crater is covered by sand, this area reduces to 1.86×10^8 m². This results in 4.53×10^{-7} mol/s of H_2O_2 or 2.26×10^{-7} mol/s of methane being destroyed, which is the same as 3.63×10^{-6} g/s. The max SAM detection of methane in crater is 9.34 ppbv (mol/ml) or 1.49×10^8 g/m³ (Webster et al., 2018). This measurement was taken at night, so the volume (area of crater times compressed PBL height) of the crater filled with methane is 2.98×10^{11} m³. The amount of methane in the crater is 2.78×10^9 g. This also results in a time frame of 24.3 million years, which is not realistic. However, as proposed by Etiope and Oehler (2019), methane is released from cracks in the soil, and is very location specific. Therefore, a SAM measurement of 9.34 ppbv does not imply that the whole crater had this concentration of methane, but only that the location of the SAM instrument had this concentration.

Let us consider this approach further. The nighttime convection inhibition mechanism proposed by Moores et al. (2019) also allows for a much smaller absolute methane flux to be detected at the same concentration level by SAM: between 1.35 and 2.35 kg/Gale/sol as opposed to the 30 kg/Gale/sol estimated by Korablev et al. (2019). This rate is based on the methane adsorption from a microseepage model as described in Moores et al. (2019). Moores et al. (2019) also provide individual methane flux estimates for each SAM measurement that range between $3.83 - 14.1 \times 10^{-8} \text{g/m}^2/\text{sol}$ for a stratified near surface and $6.95 - 25.1 \times 10^{-8} \text{g/m}^2/\text{sol}$ for a well-mixed near surface. These measurements follow the methane cycle found above. From our current understanding, methane from an underground reservoir travels through the soil to the near surface. The changes in methane flux modelled here imply that the methane is destroyed by oxidants in the soil, before reaching the surface. Assuming that the underground release is at a constant level equivalent to the maximum stratified flux ($14.1 \times 10^{-8} \text{g/m}^2/\text{sol}$), there is a destruction mechanism attenuating the flux to a minimum close to $3.83 \times 10^{-8} \text{g/m}^2/\text{sol}$ each season. We can then evaluate what percentage of the methane is destroyed by triboelectric discharge-created H_2O_2 .

If we don't multiply the rate of H_2O_2 production by an area, the rate of methane loss is $1.95 \times 10^{-14} \text{g/m}^2/\text{s}$. To convert this to a rate per sol, we multiply the number by a factor 88775, the number of seconds in one martian day, to get a rate of $1.73 \times 10^{-9} \text{g/m}^2/\text{sol}$, which is only one order of magnitude smaller than the rate of methane seepage. By this rate, triboelectric discharge would be capable of destroying 4.5% of the methane flux in one sol. Thus, as more and more oxidants accumulate in the soil with the progression of the windy season and rise in saltation activity, triboelectric discharge would cut down the level of methane seeping out of the crater by up to 4.5%, which is not close to the 72.8% attenuation needed as the minimum-maximum flux difference suggests. However, these calculations are based on the previous limitations stated.

Currently, by the same saltation simulation, triboelectric discharge is theorized to have a flux of $10 \mu\text{W/m}^2/\text{Sr}$ (Thøgersen et al., 2019), which is under the detection limit of all mission cameras (calculated in Section 3). However, if triboelectric discharge is assumed to be

responsible for all 72.8% of the methane loss, it would be 16.17 times brighter than the 4.5% methane loss calculated here. This would result in a flux of $161.7 \mu\text{W}/\text{m}^2/\text{Sr}$, which is above the detection limit of both MastCam and MAHLI on MSL. And if the triboelectric discharge flux were at the detection limit of MastCam ($40 \mu\text{W}/\text{m}^2/\text{Sr}$), it would be responsible for 18% of the methane loss based on these calculations. Thus with a planned observation, the amount of methane loss occurring with triboelectric discharge is verifiable.

It is necessary to stress that the oxidation rate of methane by H_2O_2 used in the above calculations is the result from one study that tested 10 g of sand. It is impossible to know how such a rate would change in a large dune filled with sand. The study also measured the net H_2O_2 produced after 63 days. There may have been large variations in production and destruction of H_2O_2 in that time, given that the lifetime of H_2O_2 in martian soil is not well known. The coupled effects of multiple oxidants on the oxidation rate of methane in this type of process is not known either. There are several factors at play here, which are difficult to model and account for. On the other hand, laboratory conditions make it much easier to accurately image and conduct spectrography on triboelectric discharge. On a planetary surface, there is no guarantee that a camera will be able to locate such events or how far the camera's position will be from these events. These calculations should by no means be taken as a conclusive result of the oxidation power of triboelectric discharge, however, in the context of Mars, triboelectric discharge cannot be the primary component of the fast destruction mechanism for methane.

5 Conclusion

Triboelectric discharge is produced when saltation grains are instilled with charge through contact electrification and ionize the surrounding atmospheric particles. This phenomenon was observed in laboratory experiments to have a magnitude of $10 \mu\text{W}/\text{m}^2$. Since saltation has been observed at Gale Crater during northern winter ($L_s > 180^\circ$), it is possible to attempt to observe triboelectric discharge on Mars for the first time. Saltation on Mars is a frequent and prominent phenomena, suggesting a similar ubiquity for triboelectric glow. If this is true, triboelectric glow could be the reason for the oxygen and methane variation seen at Gale Crater.

The magnitude of glow discharge is very faint, thus, it can only be observed at night, and is not possible to observe easily with current landed missions on Mars. To increase the likelihood of observing glow discharge, it is necessary to schedule the observation during the optimum environmental conditions. Saltation activity is triggered by a wind stress threshold, but the variation of wind stress at night is not well-constrained due to a lack of mission activity past sunset. In addition, evidence of saltation is observed widely on Mars, but the wind threshold achieved by martian winds is still debated. This work examined variations in saltation activity by analyzing the changes in dust concentration inside the crater, also known as extinction, instead of using wind models. When saltation occurs, dust activity also increases: this record is captured by the NavCam and MastCam LOS observation. Using MastCam-100 images for the first time, the highest resolution dust record was produced, which showed how dust lifting varied with crater height. The analysis enabled the identification of narrow periods of high dust activity, and by extension, high saltation activity. If a future observation of triboelectric charge is planned at Gale Crater, it should be scheduled in the periods suggested in Section 2.

To understand if the glow could be observed with MSL, InSight, or Mars 2020, the lab spectra were first carefully mapped on to the spectral sensitivities of onboard cameras in order to identify the best filter options. Taking into consideration signal strength, field of view, and pointing, MSL's MastCam L0, and MAHLI were identified as the best choices. However,

the signal strength was much lower than 1 digital number on all of the cameras, suggesting that the signal would not be distinguishable from noise. Thus, a series of calculations were performed to understand the radiance limit of the cameras. The dark noise of each camera was computed for a certain exposure time and temperature. This noise was propagated to a radiance value, given individual camera parameters. The radiance limit is the minimum amount of radiance an object requires to be detected by the camera. Unfortunately, all of the radiance limits were at least one order of magnitude higher than the radiance of Phobos (reflected from the ground) and two orders higher than the magnitude of glow. The radiance of Phobos was included for comparison as it is the next brightest object reflecting light from the ground. Though the cameras cannot be used to see the glow directly, the radiance limits can still be used to define an upper limit for the magnitude of glow. The most suitable cameras for this were MastCam L0 and MAHLI, which were further analyzed to understand if radiance from Phobos or any triboelectric glow had been captured in any previous nighttime sequences. Dark noise was subtracted during the processing of these images, such that only the extra radiance present in the image would be visible.

MastCam images showed two instances of significant radiance, one of scattered light behind the horizon on sol 529, and one unidentified light source at 17° of elevation on sol 729. However, saltation and Phobos shine were ruled out as the source of these illuminations. In many instances where Phobos was visible in the sky, the camera was not pointing at the crater, but higher than Phobos, and when the camera was pointing to the ground at night, Phobos was not visible. Thus, we cannot rule out the possibility of detecting Phobos shine or glow as the camera positions rarely matched the needs of this observation. When MastCam was pointed at the ground, it was also not the windy season, and thus saltation would not be expected, and thus we cannot state a reliable upper limit to the glow.

MAHLI images were always taken very close to surface targets, leaving too little space for observing saltation. These images cannot be used either to put an upper limit on glow. The four pictures that were taken of Mount Sharp on sol 165 were during the windy season but are too small a sample size to definitively say that saltation glow was not detected, since

they were taken over less than 5 minutes. It may have simply been the case that there was no saltation in that brief period of time. Phobos was visible briefly in images on sol 1337 and its radiance could have been reflected on the rock being observed. However, it was not, though it could be the case that this rock was not subject to the reach of Phobos' shine.

Overall, very few nighttime images have been taken with MAHLI or Mastcam L0 over the course of MSL's mission to date. Furthermore, even fewer of these images meet the criteria for potentially observing Phobos shine or saltation glow. The glow's location or time cannot be predicted, thus any number of sequences might prove unlucky in capturing the glow by simply looking at the wrong part of the crater or at the wrong time or both, though a series of observations taken during the northern hemisphere winter season and pointed at dunes or other likely active areas would increase the likelihood of detection. An ideal observation using currently active spacecraft would use MastCam L0 and/or MAHLI with a sustained long exposure image sequence looking out towards the crater or towards dune/active region during the upcoming windy season, repeated over a number of nights. If glow is still not directly detected, it would enable a robust upper limit on the glow radiance to be placed, equivalent to the radiance limits calculated in this paper. To see if other missions would have more success, the radiance limits of certain relevant cameras on Mars 2020 and InSight were calculated as well. These radiance limits did not prove to be lower than that of MSL.

The behaviour of oxygen and methane inside the crater suggests that triboelectric discharge is at play at Gale Crater. These gases should have atmospheric lifetimes of 60 and 350 years respectively, but show seasonal variation at Gale. The annual variation of these gases was statistically analyzed using the Lomb-Scargle method. The most probable period for both gases was found to be 1 Martian year within the error margins, despite the sparseness of these datasets. When the high resolution dust cycle obtained from Section 2 was mapped on to the oxygen and methane cycle in the crater, an increase of high dust/saltation activity was followed by a decrease in oxygen after a short phase lag. The decrease in oxygen was immediately followed by a decrease in methane. Inversely, the decrease in dust/saltation activity produced an increase in oxygen levels and methane levels with a phase lag. This

strongly suggests that the ionization of atmospheric gases by triboelectric discharge leads to a series of chemical reactions that use up atmospheric oxygen and produce oxidants, which are then deposited on the soil. The oxidants, such as H_2O_2 and perchlorates, oxidize the methane seeping out of the surface, causing the seasonal decrease in volume mixing ratio that we observe with SAM.

However, order of magnitude calculations show that the amount of oxidant produced by triboelectric discharge is not enough to explain the amount of methane decrease seen in the crater. It is possible that a combination of processes are responsible for the destruction of methane and oxygen. Dust devils are widespread and common on Mars and Gale Crater as they have been observed by many orbiter and landed missions at all latitudes (except the poles) and elevations (Cantor et al., 2006; Greeley et al., 2010; Newman et al., 2019). They are concentrated in the southern hemisphere, and vary in density locally (Reiss et al., 2016). Dust devils are larger in size compared to terrestrial dust storms, ranging in a few kms of height and a few 100 metres of width, and produce stronger electric fields than triboelectric discharge (Barth et al., 2016), which may allow them to ionize a larger volume of gas. Dust devil activity follows the same dust cycle used above and is therefore applicable to same mapping of cycles discussed. However, dust devil activity was subdued in the first two martian years compared to the third martian year according to MSL data. The increase in dust devil activity has been attributed to MSL's ascent to higher elevation terrain, which suggests that dust devils are strongly reduced in Gale Crater for the lower elevations where sand dunes reside (Ordóñez-Etxeberria et al., 2020).

Alternatively, methane may be released in seasonally varying amounts. Surface winds and topography can induce pressure pumping, and release methane from surface reservoirs (Viúdez-Moreiras et al., 2020). The dust cycle used above follows the pattern of surface winds, and thus could represent the process of pressure pumping instead of saltation in this case. The variations may also begin with methane release by advective fluxes, and become exaggerated by near surface processes such as triboelectric discharge, and bigger processes such as dust devils. It is impossible to precisely state the process responsible for methane

release and destruction at the resolution of the current methane dataset, which only takes one measurement every ~ 100 sols. For this reason, trace gases need to be observed on a much more frequent basis. Furthermore, we do not currently have instruments on Mars to decipher if the trace gases are produced by biotic or abiotic reactions, which can only be investigated using a dedicated instrument such as a Cavity Ring Down Spectrometer (Garvin, 2020). Thus, trace gas detection is crucial to the next step in the search for life on Mars.

Bibliography

- Anderson, F. S., Greeley, R., Xu, P., Lo, E., Blumberg, D. G., Haberle, R. M., and Murphy, J. R. (1999). Assessing the martian surface distribution of aeolian sand using a mars general circulation model. *Journal of Geophysical Research: Planets*, 104(E8):18991–19002.
- Aplin, K., Goodman, T., Herpoldt, K., and Davis, C. (2012). Laboratory analogues of martian electrostatic discharges. *Planetary and Space Science*, 69(1):100–104.
- ASTM (2012). Astm g173-03-standard tables for reference solar spectral irradiances: Direct normal and hemispherical on 37 tilted surface.
- Atreya, S. K., Mahaffy, P. R., and Wong, A.-S. (2007). Methane and related trace species on mars: Origin, loss, implications for life, and habitability. *Planetary and Space Science*, 55(3):358 – 369. Planet Mars II.
- Atreya, S. K., Wong, A.-S., Renno, N. O., Farrell, W. M., Delory, G. T., Sentman, D. D., Cummer, S. A., Marshall, J. R., Rafkin, S. C., and Catling, D. C. (2006). Oxidant enhancement in martian dust devils and storms: Implications for life and habitability. *Astrobiology*, 6(3):439–450.
- Ayoub, F., Avouac, J.-P., Newman, C., Richardson, M., Lucas, A., Leprince, S., and Bridges, N. (2014). Threshold for sand mobility on mars calibrated from seasonal variations of sand flux. *Nature Communications*, 5(1).
- Bak, E. N., Zafirov, K., Merrison, J. P., Jensen, S. J. K., Nørnberg, P., Gunnlaugsson, H. P., and Finster, K. (2017). Production of reactive oxygen species from abraded silicates. implications for the reactivity of the martian soil. *Earth and Planetary Science Letters*, 473:113 – 121.
- Baker, M. M., Lapotre, M. G. A., Minitti, M. E., Newman, C. E., Sullivan, R., Weitz, C. M., Rubin, D. M., Vasavada, A. R., Bridges, N. T., and Lewis, K. W. (2018). The bagnold

- dunes in southern summer: Active sediment transport on mars observed by the curiosity rover. *Geophysical Research Letters*, 45(17):8853–8863.
- Baluev, R. V. (2008). Assessing the statistical significance of periodogram peaks. *Monthly Notices of the Royal Astronomical Society*, 385(3):1279–1285.
- Barth, E. L., Farrell, W. M., and Rafkin, S. C. (2016). Electric field generation in martian dust devils. *Icarus*, 268:253 – 265.
- Bell, J., Maki, J., Mehall, G., Ravine, M., Caplinger, M., Bailey, Z., Kinch, K., Madsen, M., Betts, B., Cisneros, E., et al. (2020). The mars 2020 rover mast camera zoom (mastcam-z) multispectral, stereoscopic imaging investigation. *LPI*, (2326):1305.
- Bell, J. F., Squyres, S. W., Herkenhoff, K. E., Maki, J. N., Arneson, H. M., Brown, D., Collins, S. A., Dingizian, A., Elliot, S. T., Hagerott, E. C., and et al. (2003). Mars exploration rover athena panoramic camera (pancam) investigation. *Journal of Geophysical Research: Planets*, 108(E12).
- Bell III, J. F., Godber, A., McNair, S., Caplinger, M. A., Maki, J. N., Lemmon, M. T., Van Beek, J., Malin, M. C., Wellington, D., Kinch, K. M., Madsen, M. B., Hardgrove, C., Ravine, M. A., Jensen, E., Harker, D., Anderson, R. B., Herkenhoff, K. E., Morris, R. V., Cisneros, E., and Deen, R. G. (2017). The mars science laboratory curiosity rover mastcam instruments: Preflight and in-flight calibration, validation, and data archiving. *Earth and Space Science*, 4(7):396–452.
- Berkowitz, J., Greene, J. P., Cho, H., and Ruscić, B. (1987). The ionization potentials of ch₄ and cd₄. *The Journal of Chemical Physics*, 86(2):674–676.
- Bo, T.-L., Zhang, H., Hu, W.-W., and Zheng, X.-J. (2013). The analysis of electrification in windblown sand. *Aeolian Research*, 11:15–21.
- Bourke, M., Edgett, K., and Cantor, B. (2008). Recent aeolian dune change on mars. *Geomorphology*, 94(1):247 – 255.

- Bridges, N. T., Phoreman, J., White, B. R., Greeley, R., Eddlemon, E. E., Wilson, G. R., and Meyer, C. J. (2005). Trajectories and energy transfer of saltating particles onto rock surfaces: Application to abrasion and ventifact formation on earth and mars. *Journal of Geophysical Research*, 110(E12).
- Cantor, B. A., Kanak, K. M., and Edgett, K. S. (2006). Mars orbiter camera observations of martian dust devils and their tracks (september 1997 to january 2006) and evaluation of theoretical vortex models. *Journal of Geophysical Research: Planets*, 111(E12):n/a–n/a.
- Eden, H. F. and Vonnegut, B. (1973). Electrical breakdown caused by dust motion in low-pressure atmospheres: Considerations for mars. *Science*, 180(4089):962–963.
- Edgett, K., Caplinger, M., Maki, J., Ghaemi, F., McNair, S., Herkenhoff, K., Duston, B., Willson, R., Yingst, R., Kennedy, M., et al. (2015). Curiosity’s robotic arm-mounted mars hand lens imager (mahli): Characterization and calibration status, msl mahli technical report.
- Edgett, K. S., Yingst, R. A., Ravine, M. A., Caplinger, M. A., Maki, J. N., Ghaemi, F. T., Schaffner, J. A., Bell, J. F., Edwards, L. J., Herkenhoff, K. E., and et al. (2012). Curiosity’s mars hand lens imager (mahli) investigation. *Space Science Reviews*, 170(1-4):259–317.
- Encrenaz, T., Greathouse, T. K., Aoki, S., Daerden, F., Giuranna, M., Forget, F., Lefèvre, F., Montmessin, F., Fouchet, T., Bézard, B., and et al. (2019). Ground-based infrared mapping of h₂o₂ on mars near opposition. *Astronomy and Astrophysics*, 627:A60.
- Erman, P., Karawajczyk, A., Rachlew-Källne, E., Strömholm, C., Larsson, J., Persson, A., and Zerne, R. (1993). Direct determination of the ionization potential of co by resonantly enhanced multiphoton ionization mass spectroscopy. *Chemical Physics Letters*, 215(1):173 – 178.
- Etioppe, G. and Oehler, D. Z. (2019). Methane spikes, background seasonality and non-detections on mars: A geological perspective. *Planetary and Space Science*, 168:52 – 61.

- Fabian, A., Krauss, C., Sickafoose, A., Horanyi, M., and Robertson, S. (2001). Measurements of electrical discharges in martian regolith simulant. *IEEE transactions on plasma science*, 29(2):288–291.
- Farley, K., Martin, P., Archer, P., Atreya, S., Conrad, P., Eigenbrode, J., Fairén, A., Franz, H., Freissinet, C., Glavin, D., Mahaffy, P., Malespin, C., Ming, D., Navarro-Gonzalez, R., and Sutter, B. (2016). Light and variable $^{37}\text{Cl}/^{35}\text{Cl}$ ratios in rocks from gale crater, mars: Possible signature of perchlorate. *Earth and Planetary Science Letters*, 438:14 – 24.
- Fenton, L. K. (2005). Aeolian processes in proctor crater on mars: Mesoscale modeling of dune-forming winds. *Journal of Geophysical Research*, 110(E6).
- Fonti, S. and Marzo, G. A. (2010). Mapping the methane on mars. *Astronomy and Astrophysics*, 512:A51.
- Foreman-Mackey, D. (2018). Scalable backpropagation for gaussian processes using celerite. *Research Notes of the AAS*, 2(1):31.
- Foreman-Mackey, D., Agol, E., Ambikasaran, S., and Angus, R. (2017). Fast and scalable gaussian process modeling with applications to astronomical time series. *The Astronomical Journal*, 154(6):220.
- Foreman-Mackey, D. and Barentsen, G. (2019). dfm/exoplanet: exoplanet v0.1.3.
- Formisano, V., Atreya, S., Encrenaz, T., Ignatiev, N., and Giuranna, M. (2004). Detection of methane in the atmosphere of mars. *Science*, 306(5702):1758–1761.
- Forward, K. M., Lacks, D. J., and Sankaran, R. M. (2009). Particle-size dependent bipolar charging of martian regolith simulant. *Geophysical Research Letters*, 36(13).
- Garvin, Z. K. (2020). Trace gas consumption as a metabolic strategy for life beneath the martian surface and the means to detect it. *Whitepaper*.

- Geissler, P. E., Sullivan, R., Golombek, M., Johnson, J. R., Herkenhoff, K., Bridges, N., Vaughan, A., Maki, J., Parker, T., and Bell, J. (2010). Gone with the wind: Eolian erasure of the mars rover tracks. *Journal of Geophysical Research*, 115.
- Geminale, A., Formisano, V., and Sindoni, G. (2011). Mapping methane in martian atmosphere with pfs-mex data. *Planetary and Space Science*, 59(2):137 – 148. Methane on Mars: Current Observations, Interpretation and Future Plans.
- Gillen, E., Rimmer, P. B., and Catling, D. C. (2020). Statistical analysis of curiosity data shows no evidence for a strong seasonal cycle of martian methane. *Icarus*, 336:113407.
- Giuranna, M., Viscardy, S., Daerden, F., Neary, L., Etiope, G., Oehler, D., Formisano, V., Aronica, A., Wolkenberg, P., Aoki, S., and et al. (2019). Independent confirmation of a methane spike on mars and a source region east of gale crater. *Nature Geoscience*, 12(5):326–332.
- Golombek, M., Kipp, D., Warner, N., Daubar, I. J., Fergason, R., Kirk, R. L., Beyer, R., Huertas, A., Piqueux, S., Putzig, N. E., and et al. (2016). Selection of the insight landing site. *Space Science Reviews*, 211(1-4):5–95.
- Greeley, R., Arvidson, R. E., Barlett, P. W., Blaney, D., Cabrol, N. A., Christensen, P. R., Fergason, R. L., Golombek, M. P., Landis, G. A., Lemmon, M. T., and et al. (2006). Gusev crater: Wind-related features and processes observed by the mars exploration rover spirit. *Journal of Geophysical Research: Planets*, 111(E2):n/a–n/a.
- Greeley, R., Waller, D. A., Cabrol, N. A., Landis, G. A., Lemmon, M. T., Neakrase, L. D. V., Pendleton Hoffer, M., Thompson, S. D., and Whelley, P. L. (2010). Gusev crater, mars: Observations of three dust devil seasons. *Journal of Geophysical Research*, 115.
- Gross, F. B., Grek, S. B., Calle, C. I., and Lee, R. U. (2001). Jsc mars-1 martian regolith simulant particle charging experiments in a low pressure environment. *Journal of Electrostatics*, 53(4):257–266.

- Grotzinger, J. P., Crisp, J., Vasavada, A. R., Anderson, R. C., Baker, C. J., Barry, R., Blake, D. F., Conrad, P., Edgett, K. S., Ferdowski, B., and et al. (2012). Mars science laboratory mission and science investigation. *Space Science Reviews*, 170(1-4):5–56.
- Gwinner, K., Scholten, F., Preusker, F., Elgner, S., Roatsch, T., Spiegel, M., Schmidt, R., Oberst, J., Jaumann, R., and Heipke, C. (2010). Topography of mars from global mapping by hrsc high-resolution digital terrain models and orthoimages: Characteristics and performance. *Earth and Planetary Science Letters*, 294(3):506 – 519. Mars Express after 6 Years in Orbit: Mars Geology from Three-Dimensional Mapping by the High Resolution Stereo Camera (HRSC) Experiment.
- Hayes, A., Corlies, P., Tate, C., Barrington, M., Bell, J., Maki, J., Winhold, A., Jensen, E., Ravine, M., Capliner, M., et al. (2020). Radiometric calibration of the mastcam-z cameras for mars2020. *LPI*, (2326):2312.
- Hayward, R. K., Mullins, K. F., Fenton, L. K., Hare, T. M., Titus, T. N., Bourke, M. C., Colaprete, A., and Christensen, P. R. (2007). Mars global digital dune database and initial science results. *Journal of Geophysical Research: Planets*, 112(E11).
- Indarto, A. (2016). Partial oxidation of methane to methanol with nitrogen dioxide in dielectric barrier discharge plasma: experimental and molecular modeling. *Plasma Sources Science and Technology*, 25(2):025002.
- Iversen, J., Pollack, J., Greeley, R., and White, B. (1976). Saltation threshold on mars: The effect of interparticle force, surface roughness, and low atmospheric density. *Icarus*, 29(3):381 – 393.
- Jackson, D. W. T., Bourke, M. C., and Smyth, T. A. G. (2015). The dune effect on sand-transporting winds on mars. *Nature Communications*, 6(1).
- Kok, J. F. (2008). Electrostatics in wind-blown sand. *Physical Review Letters*, 100(1).

- Kok, J. F. (2010). An improved parameterization of wind-blown sand flux on mars that includes the effect of hysteresis. *Geophysical Research Letters*, 37(12).
- Kok, J. F. and Renno, N. O. (2006). Enhancement of the emission of mineral dust aerosols by electric forces. *Geophysical Research Letters*, 33(19).
- Korablev, O., Vandaele, A. C., Montmessin, F., Fedorova, A. A., Trokhimovskiy, A., Forget, F., Lefèvre, F., Daerden, F., Thomas, I. R., and et al. (2019). No detection of methane on mars from early exomars trace gas orbiter observations. *Nature*, 568(7753):517–520.
- Krasnopolsky, V. A. (2006). Photochemistry of the martian atmosphere: Seasonal, latitudinal, and diurnal variations. *Icarus*, 185(1):153 – 170.
- Krasnopolsky, V. A. (2012). Search for methane and upper limits to ethane and so₂ on mars. *Icarus*, 217(1):144 – 152.
- Krasnopolsky, V. A. (2017). Annual mean mixing ratios of n₂, ar, o₂, and co in the martian atmosphere. *Planetary and Space Science*, 144:71 – 73.
- Krasnopolsky, V. A., Maillard, J. P., and Owen, T. C. (2004). Detection of methane in the martian atmosphere: evidence for life? *Icarus*, 172(2):537 – 547.
- Krauss, C. E., Horanyi, M., and Robertson, S. (2003). Experimental evidence for electrostatic discharging of dust near the surface of mars. *New Journal of Physics*, 5:70–70.
- Krauss, C. E., Horányi, M., and Robertson, S. (2006). Modeling the formation of electrostatic discharges on mars. *Journal of Geophysical Research: Planets*, 111(E2):n/a–n/a.
- Küpper, M. and Wurm, G. (2015). Thermal creep-assisted dust lifting on mars: Wind tunnel experiments for the entrainment threshold velocity. *Journal of Geophysical Research: Planets*, 120(7):1346–1356.
- Lacks, D. J. (2008). Nonequilibrium accumulation of surface species and triboelectric charging in single component particulate systems. *Physical Review Letters*, 100(18).

- Langevin, Y., Gondet, B., Le Mouélic, S., Gasnault, O., Herkenhoff, K., Blaney, D., Maurice, S., Wiens, R., et al. (2013). Processing approaches for optimal science exploitation of the chemcam remote microscopic imager (rmi) during the first 90 days of curiosity operations. In *Lunar and Planetary Science Conference*, volume 44, page 1227.
- Lasne, J., Noblet, A., Szopa, C., Navarro-González, R., Cabane, M., Poch, O., Stalport, F., François, P., Atreya, S., and Coll, P. (2016). Oxidants at the surface of mars: A review in light of recent exploration results. *Astrobiology*, 16(12):977–996.
- Levin, G. V. and Straat, P. A. (2009). Methane and life on mars. *Instruments and Methods for Astrobiology and Planetary Missions XII*.
- Lowell, J. and Truscott, W. (1986). Triboelectrification of identical insulators. ii. theory and further experiments. *Journal of Physics D: Applied Physics*, 19(7):1281.
- Mahaffy, P. R., Webster, C. R., Cabane, M., Conrad, P. G., Coll, P., Atreya, S. K., Arvey, R., Barciniak, M., Benna, M., Bleacher, L., and et al. (2012). The sample analysis at mars investigation and instrument suite. *Space Science Reviews*, 170(1-4):401–478.
- Maki, J., Thiessen, D., Pourangi, A., Kobzeff, P., Litwin, T., Scherr, L., Elliott, S., Dingizian, A., and Maimone, M. (2012). The mars science laboratory engineering cameras. *Space Science Reviews*, 170(1-4):77–93.
- Maki, J. N., Bell, J. F., Herkenhoff, K. E., Squyres, S. W., Kiely, A., Klimesh, M., Schwochert, M., Litwin, T., Willson, R., Johnson, A., and et al. (2003). Mars exploration rover engineering cameras. *Journal of Geophysical Research: Planets*, 108(E12).
- Maki, J. N., Golombek, M., Deen, R., Abarca, H., Sorice, C., Goodsall, T., Schwochert, M., Lemmon, M., Trebi-Ollennu, A., and Banerdt, W. B. (2018a). The color cameras on the insight lander. *Space Science Reviews*, 214(6).
- Maki, J. N., Trebi-Ollennu, A., Deen, R., Golombek, M., Abarca, H., Sorice, C., Banerdt,

- W. B., and Schwochert, M. (2018b). The color cameras on the insight mars lander. *LPI*, (2764):1305.
- Malin, M., Bell, J., Cameron, J., Dietrich, W., Edgett, K., Hallet, B., Herkenhoff, K., Lemmon, M., Parker, T., Sullivan, R., Sumner, D., Thomas, P., Wohl, E., Ravine, M., Caplinger, M., and Maki, J. (2005). The mast cameras and mars descent imager (mardi) for the 2009 mars science laboratory.
- Malin, M. C., Ravine, M. A., Caplinger, M. A., Tony Ghaemi, F., Schaffner, J. A., Maki, J. N., Bell III, J. F., Cameron, J. F., Dietrich, W. E., Edgett, K. S., Edwards, L. J., Garvin, J. B., Hallet, B., Herkenhoff, K. E., Heydari, E., Kah, L. C., Lemmon, M. T., Minitti, M. E., Olson, T. S., Parker, T. J., Rowland, S. K., Schieber, J., Sletten, R., Sullivan, R. J., Sumner, D. Y., Aileen Yingst, R., Duston, B. M., McNair, S., and Jensen, E. H. (2017). The mars science laboratory (msl) mast cameras and descent imager: Investigation and instrument descriptions. *Earth and Space Science*, 4(8):506–539.
- Malvar, H. S., Li-wei He, and Cutler, R. (2004). High-quality linear interpolation for demosaicing of bayer-patterned color images. In *2004 IEEE International Conference on Acoustics, Speech, and Signal Processing*, volume 3, pages iii–485.
- Maurice, S., Wiens, R. C., Saccoccio, M., Barraclough, B., Gasnault, O., Forni, O., Mangold, N., Baratoux, D., Bender, S., Berger, G., and et al. (2012). The chemcam instrument suite on the mars science laboratory (msl) rover: Science objectives and mast unit description. *Space Science Reviews*, 170(1-4):95–166.
- McCord, T. B. and Adams, J. B. (1969). Spectral reflectivity of mars. *Science*, 163(3871):1058–1060.
- Melnik, O. and Parrot, M. (1998). Electrostatic discharge in martian dust storms. *Journal of Geophysical Research: Space Physics*, 103(A12):29107–29117.
- Moore, C. A., Moores, J. E., Newman, C. E., Lemmon, M. T., Guzewich, S. D., and Battalio,

- M. (2019). Vertical and horizontal heterogeneity of atmospheric dust loading in northern gale crater, mars. *Icarus*, 329:197 – 206.
- Moore, J. E., King, P. L., Smith, C. L., Martinez, G. M., Newman, C. E., Guzewich, S. D., Meslin, P., Webster, C. R., Mahaffy, P. R., Atreya, S. K., and et al. (2019). The methane diurnal variation and microseepage flux at gale crater, mars as constrained by the exomars trace gas orbiter and curiosity observations. *Geophysical Research Letters*, 46(16):9430–9438.
- Moore, J. E., Lemmon, M. T., Kahanpää, H., Rafkin, S. C., Francis, R., Pla-Garcia, J., Bean, K., Haberle, R., Newman, C., Mischna, M., Vasavada, A. R., [de la Torre Juárez], M., Rennó, N., Bell, J., Calef, F., Cantor, B., McConnochie, T. H., Harri, A.-M., Genzer, M., Wong, M. H., Smith, M. D., Martín-Torres, F. J., Zorzano, M.-P., Kempainen, O., and McCullough, E. (2015). Observational evidence of a suppressed planetary boundary layer in northern gale crater, mars as seen by the navcam instrument onboard the mars science laboratory rover. *Icarus*, 249:129 – 142. Special Issue: First Year of MSL.
- Mumma, M. J., Villanueva, G. L., Novak, R. E., Hewagama, T., Bonev, B. P., DiSanti, M. A., Mandell, A. M., and Smith, M. D. (2009). Strong release of methane on mars in northern summer 2003. *Science*, 323(5917):1041–1045.
- Namikas, S. L. (2003). Field measurement and numerical modelling of aeolian mass flux distributions on a sandy beach. *Sedimentology*, 50(2):303–326.
- NASA (2020a). Solary system exploration, mars: Facts and figures.
- NASA (2020b). Solary system exploration, phobos: Facts and figures.
- Nelessen, A., Sackier, C., Clark, I., Brugarolas, P., Villar, G., Chen, A., Stehura, A., Otero, R., Stille, E., Way, D., Edquist, K., Mohan, S., Giovingo, C., and Lefland, M. (2019). Mars 2020 entry, descent, and landing system overview. In *2019 IEEE Aerospace Conference*, pages 1–20.

- Newman, C. E., Gómez-Elvira, J., Marin, M., Navarro, S., Torres, J., Richardson, M. I., Battalio, J. M., Guzewich, S. D., Sullivan, R., de la Torre, M., Vasavada, A. R., and Bridges, N. T. (2017). Winds measured by the rover environmental monitoring station (rems) during the mars science laboratory (msl) rover's bagnold dunes campaign and comparison with numerical modeling using marswrf. *Icarus*, 291:203 – 231.
- Newman, C. E., Kahanpää, H., Richardson, M. I., Martínez, G. M., Vicente-Retortillo, A., and Lemmon, M. T. (2019). Marswrf convective vortex and dust devil predictions for gale crater over 3 mars years and comparison with msl-rems observations. *Journal of Geophysical Research: Planets*, 124(12):3442–3468.
- Olawale, D., Okoli, O., Fontenot, R., and Hollerman, W. (2016). *Triboluminescence: Theory, synthesis, and application*. Springer International Publishing.
- Ordóñez-Etxeberria, I., Hueso, R., and Sánchez-Lavega, A. (2020). Strong increase in dust devil activity at gale crater on the third year of the msl mission and suppression during the 2018 global dust storm. *Icarus*, 347:113814.
- Owen, T. and Biemann, K. (1976). Composition of the atmosphere at the surface of mars: Detection of argon-36 and preliminary analysis. *Science*, 193(4255):801–803.
- Oze, C. (2005). Have olivine, will gas: Serpentinization and the abiogenic production of methane on mars. *Geophysical Research Letters*, 32(10).
- Qian, M., Li, G., Kang, J., Liu, S., Yuan, D., Ren, C., Zhang, J., and Wang, D. (2018). The effect of hydrogen peroxide concentration on the partial oxidation of methane to methanol in an atmospheric dielectric barrier discharge. *AIP Advances*, 8(12):125224.
- Ray, S. (2013). *An introduction to high voltage engineering*. PHI Learning Pvt. Ltd.
- Reiss, D., Fenton, L., Neakrase, L., Zimmerman, M., Statella, T., Whelley, P., Rossi, A. P., and Balme, M. (2016). Dust devil tracks. *Space Science Reviews*, 203(1-4):143–181.

- Renno, N. O. and Kok, J. F. (2008). Electrical activity and dust lifting on earth, mars, and beyond. In *Planetary Atmospheric Electricity*, pages 419–434. Springer.
- Rice, M. A., Willetts, B. B., and McEwan, I. (1995). An experimental study of multiple grain-size ejecta produced by collisions of saltating grains with a flat bed. *Sedimentology*, 42(4):695–706.
- Rieder, R., Economou, T., Wänke, H., Turkevich, A., Crisp, J., Brückner, J., Dreibus, G., and McSween, H. Y. (1997). The chemical composition of martian soil and rocks returned by the mobile alpha proton x-ray spectrometer: Preliminary results from the x-ray mode. *Science*, 278(5344):1771.1–1774.
- Schmidt, D. S., Schmidt, R. A., and Dent, J. D. (1998). Electrostatic force on saltating sand. *Journal of Geophysical Research: Atmospheres*, 103(D8):8997–9001.
- Seto, M., Noguchi, K., and Cappellen, P. V. (2019). Potential for aerobic methanotrophic metabolism on mars. *Astrobiology*, 19(10):1187–1195.
- Sharma, R., Clark, D. W., Srirama, P. K., and Mazumder, M. K. (2008). Tribocharging characteristics of the mars dust simulant (jsc mars-1). *IEEE Transactions on Industry Applications*, 44(1):32–39.
- Silvestro, S., Vaz, D. A., Ewing, R. C., Rossi, A. P., Fenton, L. K., Michaels, T. I., Flahaut, J., and Geissler, P. E. (2013). Pervasive aeolian activity along rover curiosity’s traverse in gale crater, mars. *Geology*, 41(4):483 – 486.
- Simonelli, D. P., Wisz, M., Switala, A., Adinolfi, D., Veverka, J., Thomas, P. C., and Helfenstein, P. (1998). Photometric properties of phobos surface materials from viking images. *Icarus*, 131(1):52 – 77.
- Smith, C. L. (2020). The line-of-sight extinction record at gale crater as observed by msl’s mastcam and navcam through 2556 sols. Submitted to JGR: Planets.

- Smith, C. L., Moores, J. E., Lemmon, M., Guzewich, S. D., Moore, C. A., Ellison, D., and Khayat, A. S. J. (2019). Visibility and line-of-sight extinction estimates in gale crater during the 2018/my34 global dust storm. *Geophysical Research Letters*, 46(16):9414–9421.
- Smith, P. H. and Lemmon, M. (1999). Opacity of the martian atmosphere measured by the imager for mars pathfinder. *Journal of Geophysical Research: Planets*, 104(E4):8975–8985.
- Snow, K. B. and Thomas, T. F. (1990). Mass spectrum, ionization potential, and appearance potentials for fragment ions of sulfuric acid vapor. *International Journal of Mass Spectrometry and Ion Processes*, 96(1):49 – 68.
- Sternovsky, Z., Robertson, S., Sickafoose, A., Colwell, J., and Horányi, M. (2002). Contact charging of lunar and martian dust simulants. *Journal of Geophysical Research: Planets*, 107(E11):15–1.
- Sullivan, R., Arvidson, R., Bell, J. F., Gellert, R., Golombek, M., Greeley, R., Herkenhoff, K., Johnson, J., Thompson, S., Whelley, P., and et al. (2008). Wind-driven particle mobility on mars: Insights from mars exploration rover observations at “el dorado” and surroundings at gusev crater. *Journal of Geophysical Research*, 113(E6).
- Sullivan, R. and Kok, J. F. (2017). Aeolian saltation on mars at low wind speeds. *Journal of Geophysical Research: Planets*, 122(10):2111–2143.
- Sutter, B., McAdam, A. C., Mahaffy, P. R., Ming, D. W., Edgett, K. S., Rampe, E. B., Eigenbrode, J. L., Franz, H. B., Freissinet, C., Grotzinger, J. P., Steele, A., House, C. H., Archer, P. D., Malespin, C. A., Navarro-González, R., Stern, J. C., Bell, J. F., Calef, F. J., Gellert, R., Glavin, D. P., Thompson, L. M., and Yen, A. S. (2017). Evolved gas analyses of sedimentary rocks and eolian sediment in gale crater, mars: Results of the curiosity rover’s sample analysis at mars instrument from yellowknife bay to the namib dune. *Journal of Geophysical Research: Planets*, 122(12):2574–2609.
- Swann, C., Sherman, D. J., and Ewing, R. C. (2020). Experimentally derived thresholds for windblown sand on mars. *Geophysical Research Letters*, 47(3).

- Thøgersen, J., Bak, E. N., Finster, K., Nørnberg, P., Jakobsen, H. J., and Jensen, S. J. K. (2019). Light on windy nights on mars: A study of saltation-mediated ionization of argon in a mars-like atmosphere. *Icarus*, 332:14 – 18.
- Tillman, J. E., Johnson, N. C., Guttorp, P., and Percival, D. B. (1993). The martian annual atmospheric pressure cycle: Years without great dust storms. *Journal of Geophysical Research*, 98(E6):10963.
- Tonkyn, R. G., Winniczek, J. W., and White, M. G. (1989). Rotationally resolved photoionization of o_2^+ near threshold. *Chemical Physics Letters*, 164(2):137 – 142.
- Trainer, M. G., Wong, M. H., McConnochie, T. H., Franz, H. B., Atreya, S. K., Conrad, P. G., Lefèvre, F., Mahaffy, P. R., Malespin, C. A., Manning, H. L., et al. (2019). Seasonal variations in atmospheric composition as measured in gale crater, mars. *Journal of Geophysical Research: Planets*, 124(11):3000–3024.
- Treumann, R. A., Kłos, Z., and Parrot, M. (2008). Physics of electric discharges in atmospheric gases: An informal introduction. In *Planetary Atmospheric Electricity*, pages 133–148. Springer.
- Trickl, T., Cromwell, E. F., Lee, Y. T., and Kung, A. H. (1989). State-selective ionization of nitrogen. *The Journal of Chemical Physics*, 91(10):6006–6012.
- Tyler, D. and Barnes, J. R. (2015). Convergent crater circulations on mars: Influence on the surface pressure cycle and the depth of the convective boundary layer. *Geophysical Research Letters*, 42(18):7343–7350.
- VanderPlas, J., Connolly, A. J., Ivezić, Ž., and Gray, A. (2012). Introduction to astroml: Machine learning for astrophysics. In *2012 Conference on Intelligent Data Understanding*, pages 47–54.
- VanderPlas, J. T. (2018). Understanding the lomb–scargle periodogram. *The Astrophysical Journal Supplement Series*, 236(1):16.

- VanderPlas, J. T. and Ivezić, Ž. (2015). Periodograms for multiband astronomical time series. *The Astrophysical Journal*, 812(1):18.
- Villanueva, G., Mumma, M., Novak, R., Radeva, Y., Käufel, H., Smette, A., Tokunaga, A., Khayat, A., Encrenaz, T., and Hartogh, P. (2013). A sensitive search for organics (ch₄, ch₃oh, h₂co, c₂h₆, c₂h₂, c₂h₄), hydroperoxyl (ho₂), nitrogen compounds (n₂o, nh₃, hcn) and chlorine species (hcl, ch₃cl) on mars using ground-based high-resolution infrared spectroscopy. *Icarus*, 223(1):11 – 27.
- Viscardy, S., Daerden, F., and Neary, L. (2016). Formation of layers of methane in the atmosphere of mars after surface release. *Geophysical Research Letters*, 43(5):1868–1875.
- Viúdez-Moreiras, D., Gómez-Elvira, J., Newman, C., Navarro, S., Marin, M., Torres, J., and [de la Torre-Juárez], M. (2019a). Gale surface wind characterization based on the mars science laboratory rems dataset. part i: Wind retrieval and gale’s wind speeds and directions. *Icarus*, 319:909 – 925.
- Viúdez-Moreiras, D., Gómez-Elvira, J., Newman, C., Navarro, S., Marin, M., Torres, J., and [de la Torre-Juárez], M. (2019b). Gale surface wind characterization based on the mars science laboratory rems dataset. part ii: Wind probability distributions. *Icarus*, 319:645 – 656.
- Viúdez-Moreiras, D., Arvidson, R. E., Gómez-Elvira, J., Webster, C., Newman, C. E., Mahaffy, P., and Vasavada, A. R. (2020). Advective fluxes in the martian regolith as a mechanism driving methane and other trace gas emissions to the atmosphere. *Geophysical Research Letters*, 47(3).
- Wang, L.-S., Reutt, J., Lee, Y., and Shirley, D. (1988). High resolution uv photoelectron spectroscopy of co⁺, cos⁺ and cs⁺ using supersonic molecular beams. *Journal of Electron Spectroscopy and Related Phenomena*, 47:167 – 186.
- Webster, C. R., Mahaffy, P. R., Atreya, S. K., Moores, J. E., Flesch, G. J., Malespin, C.,

- McKay, C. P., Martinez, G., Smith, C. L., Martin-Torres, J., and et al. (2018). Background levels of methane in mars' atmosphere show strong seasonal variations. *Science*, 360(6393):1093–1096.
- Wray, J. J. (2012). Gale crater: the mars science laboratory/curiosity rover landing site. *International Journal of Astrobiology*, 12(1):25–38.
- Wu, Z., Wang, A., Farrell, W. M., Yan, Y., Wang, K., Houghton, J., and Jackson, A. W. (2018). Forming perchlorates on mars through plasma chemistry during dust events. *Earth and Planetary Science Letters*, 504:94 – 105.
- Zahnle, K., Freedman, R. S., and Catling, D. C. (2011). Is there methane on mars? *Icarus*, 212(2):493 – 503.
- Zhai, Y., Cummer, S. A., and Farrell, W. M. (2006). Quasi-electrostatic field analysis and simulation of martian and terrestrial dust devils. *Journal of Geophysical Research*, 111(E6).
- Zheng, X., Jin, T., and Wang, P. (2020). The influence of surface stress fluctuation on saltation sand transport around threshold. *Journal of Geophysical Research: Earth Surface*, 125(5):e2019JF005246.
- Zheng, X. J., Huang, N., and Zhou, Y.-H. (2003). Laboratory measurement of electrification of wind-blown sands and simulation of its effect on sand saltation movement. *Journal of Geophysical Research: Atmospheres*, 108(D10).

Appendices

A MAHLI Image Calibration

This section details the procedure required to enable a comparison of MAHLI to MastCam-34 and MastCam-100 images in radiance units; it was provided by Dr. Mark Lemmon (Space Science Institute). Radiance units ($\text{W}/\text{m}^2/\text{nm}/\text{Sr}$) are produced by the ASU ‘Version 2’ calibration pipeline for Mastcam. Bell III et al. (2017) describes the calibration and validation through comparison of sky models to images. The reference product is a MastCam-34 image calibrated with the “Pre-Flight” coefficients. (The sky model coefficient is preferred for LR2, which is not relevant here.) Note that MAHLI RGB is assumed to represent the same wavelengths as MastCam-34 RGB for the purpose of this analysis.

The sky model, by definition, forces simultaneous L0 and R0 images of the sky to have the same radiance. However, the sky model coefficients and pre-flight coefficients have a different ratio for the two eyes. To force R0 images to have the property that simultaneous L0 and R0 images of the sky have the same radiance for the same geometry, the R0 images must be multiplied by 0.922. The MAHLI products used are the ‘DRXX’ , an I/F type unit, but can be rescaled to match the MastCam-34 calibration to allow intercomparison. The first step in rescaling is to make the MAHLI image proportional to radiance. That requires reading in the image with use of the RADIANCE_SCALING_FACTOR; accounting for the FOCUS_POSITION_COUNT-dependent focal ratio; and undoing the correction for the Mars-Sun distance.

1. Read in the 16-bit, 3-color DRXX file, convert to floating point, and apply the scaling factor and offset to get a radiometrically calibrated image.
2. Determine and correct for the focal ratio:
 - (a) For f_{pc} (FOCUS_POSITION_COUNT) in a cover-open position, determine dw

(working distance):

$$dw = (a/f_{pc} + b + c \times f_{pc} + d \times f_{pc}^2 + e \times f_{pc}^3)^{-1} \quad (18)$$

where $a = 0.576786$; $b = -11.8479$; $c = 2.80153 \times 10^{-3}$; $d = -2.266488 \times 10^{-7}$; $e = 6.26666 \times 10^{-12}$.

(b) Determine focal ratio, *frat*, from:

$$frat = \frac{8.47}{1 - e^{-0.859617 \times dw^{-1.2975}}} \quad (19)$$

(c) If focal ratio value is above 9.8 or below 8.47, limit focal ratio to these upper and lower bounds.

(d) Correct radiance (*RAD*) in a radiometrically calibrated MAHLI image by, $RAD = RAD \times (frat/9.0)^2$. The choice of 9.0 as the reference value is based on Edgett et al. (C&C status paper).

3. Determine and correct for the Mars-Sun distance. In this case, multiply *RAD* by $(1.38/r_{au})^2$, where r_{au} is the Mars-Sun distance in AU.

Carrying out the above steps results in an image whose pixel values are in radiance units. A constant of proportionality is needed to make the image radiance-proportionate to MastCam. This can be done with reference to MastCam-34 values. As of sol 1695, 9 sets of MAHLI sky flats had been obtained in conjunction with an M34 sky image. Of these 9 sets, the sol 1695 M34 image was not downlinked; and the sol 989 and 1157 MAHLI images do not have the RADIANCE_SCALING_FACTOR in the DRXX files available. Thus, this analysis uses the sol 322, 516, 653, 828, 1340, and 1498 MAHLI sky flats. Images with the cover closed were not considered.

MAHLI radiometrically calibrated images and MastCam-34 images were projected into a Sun-relative sky mosaic. All areas of the sky (at 0.25 degree-resolution) that were in each MAHLI and MastCam-34 image for a sol were averaged for each image. Step (d) results in all MAHLI images having radiance values that are linearly proportional to the solar elevation

angle. Therefore, a linear fit was used, and the Mastcam radiance was divided by the MAHLI radiance projected to the Mastcam time. For sol 322, this was an interpolation; for the other images, this required a small extrapolation. Using a sky radiative transfer model to guide the extrapolation was considered, but was not deemed to provide significant improvements.

Table A.1: Ratio of MastCam-34 radiance to MAHLI RAD value ($\text{W}/\text{m}^2/\text{nm}/\text{Sr}$)

Index	sol	R ratio	G ratio	B ratio
0	322	0.315	0.324	0.377
1	516	0.309	0.318	0.363
2	653	0.305	0.318	0.371
3	828	0.312	0.321	0.378
4	1340	0.29	0.299	0.345
5	1498	0.292	0.299	0.347
Average		0.304	0.313	0.364
Std dev %		3.4	3.5	4
Average, 0-3		0.31	0.32	0.372
Std dev, 0-3 %		1.3	0.9	1.8
Intercept	516	0.311	0.321	0.372
Tscale= $-1\%/\text{Slope}$		149 sols	139 sols	139 sols
RMS error %		1.3	1	2

Table A.1 and Figure A1 show the ratio by which to MAHLI radiometrically calibrated products (as defined above) must be multiplied to get equivalent MastCam-34 radiances. The ratios are found to decrease as mission sol increases. This could be caused by decreased MastCam-34 transmission due to dust in the image optics. This decrease in ratio could be quasi-linear, or a discrete event between sol 828 and 1340. In addition to reporting each measurement, Table A.1 presents the average of all data points (with standard deviation of

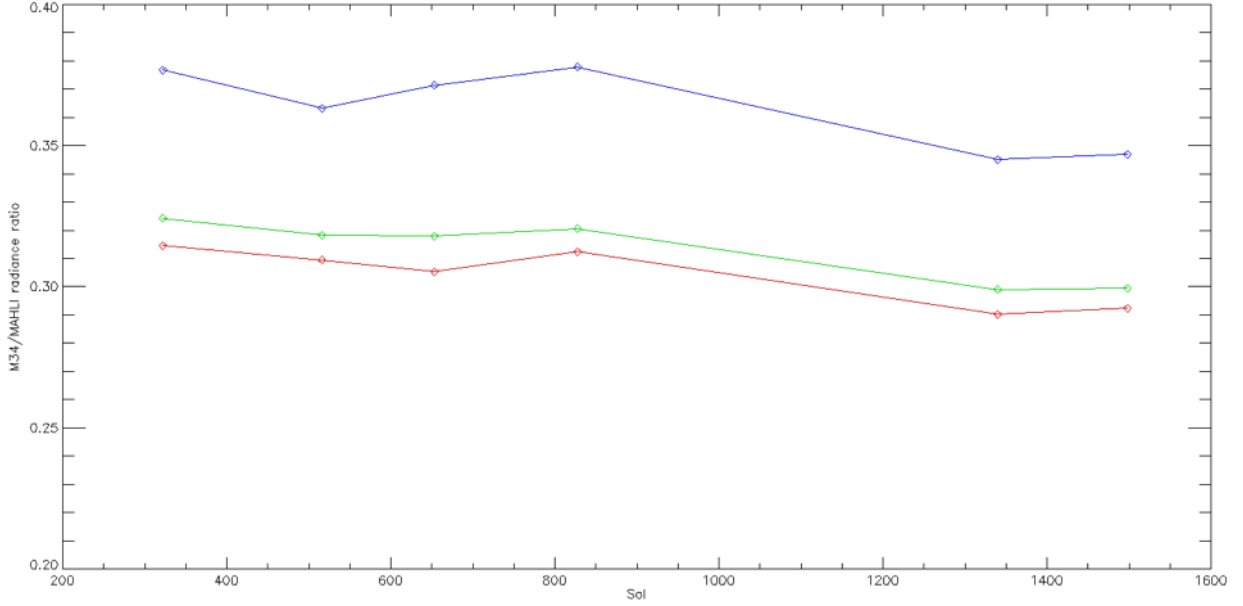


Figure A1: Ratio of MastCam-34 radiance to MAHLI RAD for red, green, and blue channels, in time order.

3.4-4.0%); the average of the first 4 data points (with standard deviation of 0.9-1.8%); and a linear fit, which is referenced to sol 516 (with RMS error of 1.0-2.0%).

The current recommendation to make the MAHLI image radiance-proportionate to Mast-Cam, is to use the average of the first 4 ratios for sols 0-828; or to use the linear fit for any sols:

$$R = I \times \left(1 - \frac{S - 516}{T \times 100} \right) \quad (20)$$

where R is the ratio in any R, G, B filter, I is the intercept of the respective filter as listed in Table A.1, S is sol of the MAHLI image in question, and T is the Tscale of the respective filter as listed in Table A.1.

B Vertical extinction with complete MastCam-100 LOS dataset

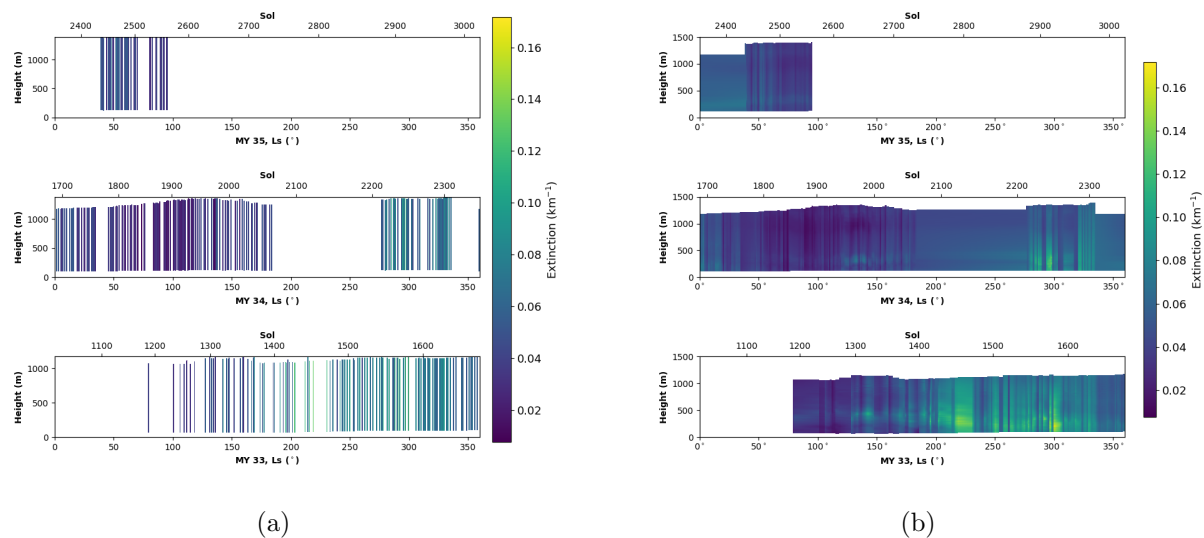


Figure B1: Variation in Red Filter Vertical Extinction at Gale with sol and L_s of complete LOS dataset. X-axis represents height above the surface of the crater. (a) Each vertical line is the extinction calculated from one LOS image, averaged across azimuth. (b) Linear interpolation on individual extinction bars across the entire sol span of the data. Pixel radiance is represented by colour bar intensity.

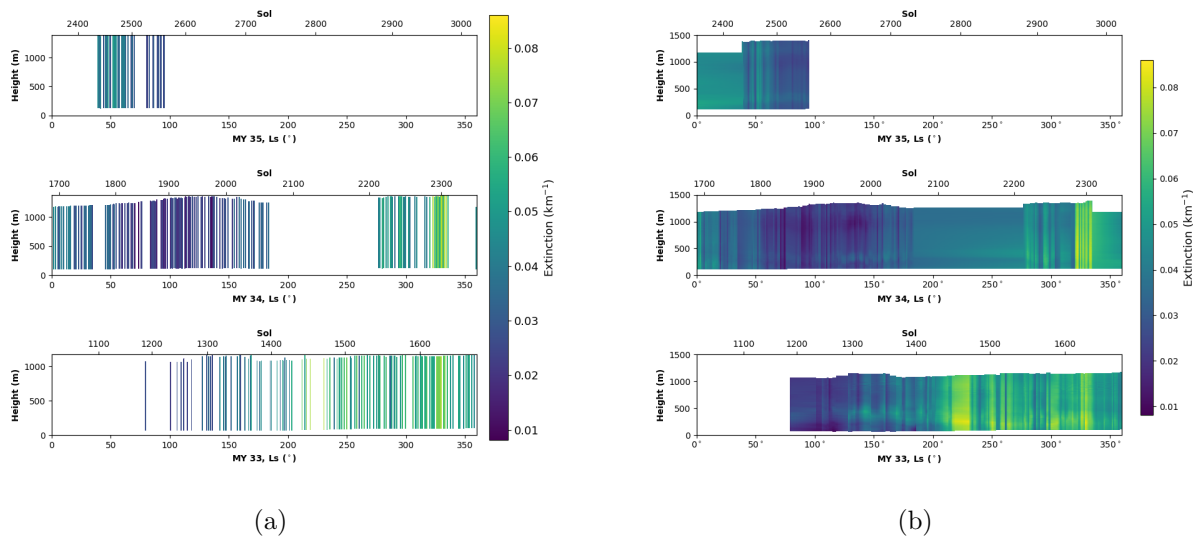


Figure B2: Variation in Green Filter Vertical Extinction at Gale with sol and L_s of complete LOS dataset. X-axis represents height above the surface of the crater. (a) Each vertical line is the extinction calculated from one LOS image, averaged across azimuth. (b) Linear interpolation on individual extinction bars across the entire sol span of the data. Pixel radiance is represented by colour bar intensity.

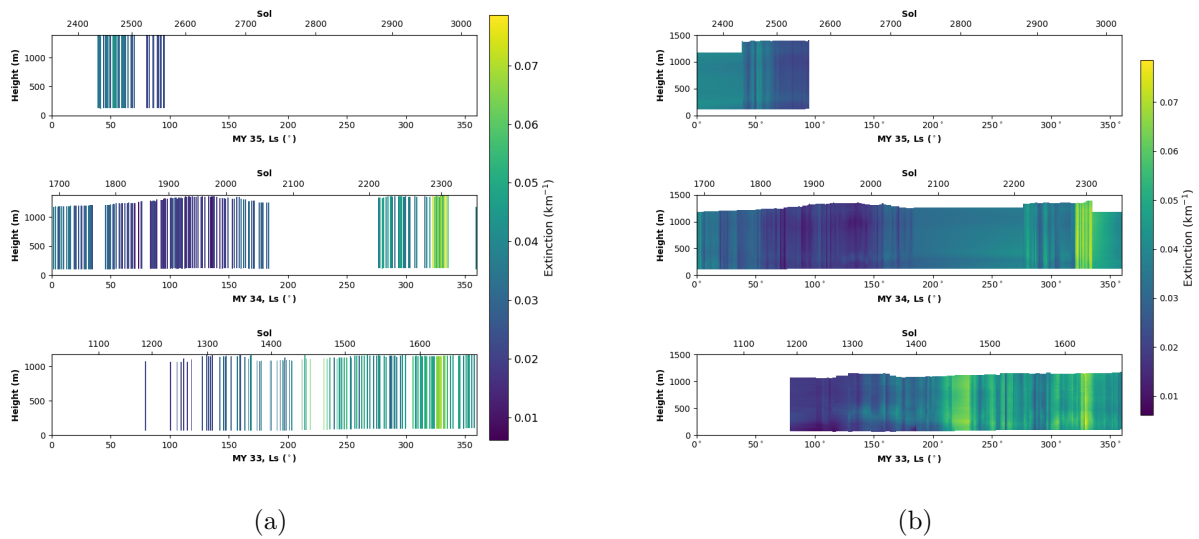


Figure B3: Variation in Blue Filter Vertical Extinction at Gale with sol and L_s of complete LOS dataset. X-axis represents height above the surface of the crater. (a) Each vertical line is the extinction calculated from one LOS image, averaged across azimuth. (b) Linear interpolation on individual extinction bars across the entire sol span of the data. Pixel radiance is represented by colour bar intensity.